SANDIA REPORT

SAND2014-17867
Unlimited Release
Printed September 2014

Validation of Heat Transfer, Thermal Decomposition, and Container Pressurization of Polyurethane Foam

Sarah N. Scott, Amanda B. Dodd, Marvin E. Larsen, Jill M. Suo-Anttila, Ken L. Erickson

Prepared by
Sandia National Laboratories
Albuquerque, New Mexico 87185 and Livermore, California 94550

Sandia National Laboratories is a multi-program laboratory managed and operated by Sandia Corporation,
a wholly owned subsidiary of Lockheed Martin Corporation, for the U.S. Department of Energy's
National Nuclear Security Administration under contract DE-AC04-94AL85000.

Sandia National Laboratories

Issued by Sandia National Laboratories, operated for the United States Department of Energy by Sandia Corporation.

Available to DOE and DOE contractors from
U.S. Department of Energy
Office of Scientific and Technical Information
P.O. Box 62
Oak Ridge, TN 37831

Telephone: (865) 576-8401
Facsimile: (865) 576-5728
E-Mail: reports@adonis.osti.gov
Online ordering: http://www.osti.gov/bridge

Available to the public from
U.S. Department of Commerce
National Technical Information Service
5285 Port Royal Rd.
Springfield, VA 22161

Telephone: (800) 553-6847
Facsimile: (703) 605-6900
E-Mail: orders@ntis.fedworld.gov
Online order: http://www.ntis.gov/help/ordermethods.asp?loc=7-4-0#online

SAND2014-17867
Unlimited Release
Printed September 2014

Validation of Heat Transfer, Thermal Decomposition, and Container Pressurization of Polyurethane Foam

Sarah N. Scott and Amanda B. Dodd
Thermal/Fluids Science and Engineering
Sandia National Laboratories
P.O. Box 969
Livermore, CA 94550-MS9042

Marvin E. Larsen
Thermal Sciences and Engineering
Sandia National Laboratories
P.O. Box 5800
Albuquerque, New Mexico 87185-MS0836

Jill M. Suo-Anttila
Fire Science and Technology
Sandia National Laboratories
P.O. Box 5800
Albuquerque, New Mexico 87185-MS1135

Ken L. Erickson

Abstract

Polymer foam encapsulants provide mechanical, electrical, and thermal isolation in engineered systems. In fire environments, gas pressure from thermal decomposition of polymers can cause mechanical failure of sealed systems. In this work, a detailed uncertainty quantification study of PMDI-based polyurethane foam is presented to assess the validity of the computational model. Both experimental measurement uncertainty and model prediction uncertainty are examined and compared. Both the mean value method and Latin hypercube sampling approach are used to propagate the uncertainty through the model. In addition to comparing computational and experimental results, the importance of each input parameter on the simulation result is also investigated. These results show that further development in the physics model of the foam and appropriate associated material testing are necessary to improve model accuracy.

ACKNOWLEDGMENTS

The authors would like to thank Patricia Hough, Timothy Koehler, and Ryan Keedy for reviewing this report.

CONTENTS

FIGURES

TABLES

1. INTRODUCTION

Polymers and other organic materials have a long history of use in mechanical systems to provide mechanical, electrical, and thermal isolation. Accurately modeling organic materials in thermal environments can be challenging due to complex physics, uncertain thermal properties, and the relatively low decomposition temperatures. When polymers are exposed to a source of heat, such as fire, they undergo both physical and chemical changes [1]. The chemical breakdown, or decomposition, of the polymer causes large molecules to fragment, forming a variety of smaller molecules. These smaller fragments can vary greatly in size and properties and can undergo further decomposition. The chemical subspecies have differing equilibrium vapor pressures and those subspecies with the highest vapor pressures will quickly vaporize and in a sealed system can cause the container to pressurize. The subspecies that do not vaporize are left in either a liquid or solid form. While it is possible for a polymer to decompose completely into vapor, it is unlikely. Typically, solid residue is left behind and, in a material that chars, this layer can be porous.

Due to the wide range of mechanical systems where polyurethane foam is used (*e.g.* automobiles, airplanes), it is prohibitively expensive to test all of these systems in multiple configurations to understand the foam's behavior in each case. Therefore, it is desirable to have a physics based computational model of the foam that can be used to examine multiple heating scenarios and physical configurations.

This work presents a validation assessment of a computational model of thermally decomposing polymeric methylene diisocyanate (PMDI)-polyether-polyol based polyurethane foam. The computational model, described in Erickson *et al.* [2-4], simulates organic material decomposition, heat transfer, and pressurization. The model uses the diffusion approximation to simulate radiant heat transfer, Arrhenius reaction kinetics to convert solid into decomposed products, and an ideal gas law to calculate pressure as a function of time and temperature. Each of the thermal properties and model assumption choices contain an associated uncertainty. When assessing the validity of a model, it is not only necessary to compare a nominal model to experimental data, but to also employ uncertainty quantification techniques to propagate experimental and modeling uncertainty through the model. The end result is model and experimental data with a mean response and a standard deviation. In the current paper, we employ two uncertainty quantification techniques, the mean value method (MV) as well as the Latin hypercube sampling (LHS) approach. These two approaches are commonly used in assessing model validity with uncertainty quantification. For a small number of uncertain parameters, the mean value method can offer savings on the number of simulations that are required for an analysis, although this savings does not scale well with a large number of parameters. Since the current study contains a relatively small number of parameters, the MV is used to propagate uncertainty through the model. Since the MV assumes a linear relationship between the parameter variation and the response (this will be discussed in more detail later) LHS (which does not assume this) was used to propagate uncertainty for a subset of the data. The results of the two methods are compared in order to identify any nonlinear relationships between parameters and responses.

2. EXPERIMENTS

The experimental data that is used for comparison is referred to as known as Foam In a Can (FIC). The experimental configuration consists of a stainless steel cylindrical container filled with foam along with an embedded metal object (Figure 1a and c). This experiment has been performed in the upright and inverted orientations (Figure 1b). The dimensions of the three cans used are shown in Figure 2 and Table 1. The exterior surfaces of the can were painted with Pyromark^{TM} 2500 series flat black paint to ensure consistent, uniform radiative properties. Foam samples are cast oversized and then machined to a snug fit in the container and around the encapsulated mass. The foam samples were polymeric methylene diisocyanate (PMDI)-polyether-polyol based polyurethane foam (PUF) with a range of densities.

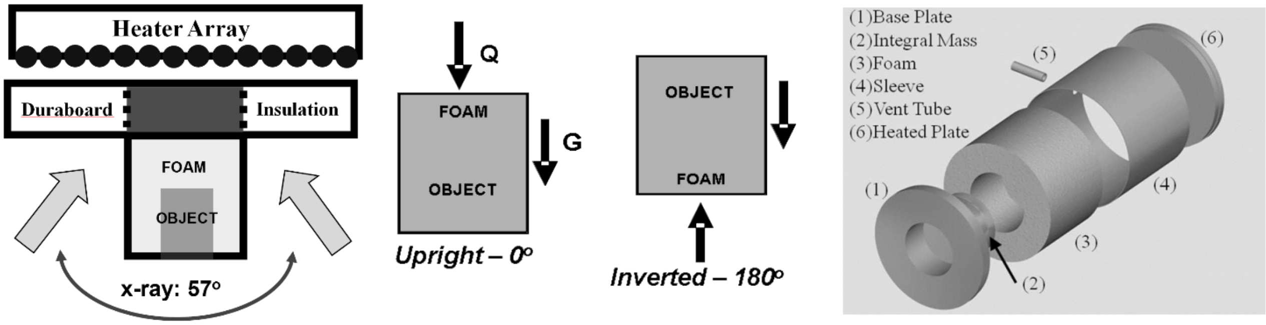

(a) (b) (c)

Figure 1. FIC Experiment: (a) experimental setup of the foam in a can experiments, (b) description of upright and inverted heating, and (d) an exploded view of the geometry.

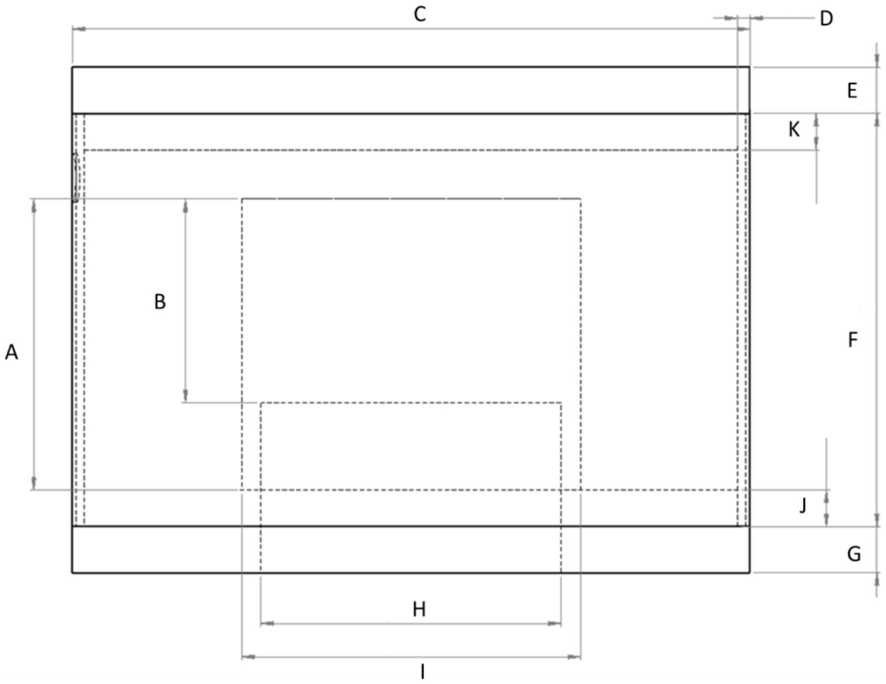

Figure 2. Schematic of the can. Values for the dimensions are given in Table 1

Table 1 Dimension Value

Dimension	2010		2011		2012-2013	
	in	*cm*	*in*	*cm*	*in*	*cm*
A	1.5	3.81	1.5	3.81	1.5	3.81
B	1.05	2.67	1.05	2.667	0.425	1.0795
C	3.5	8.89	3.5	8.89	3.5	8.89
D	0.03	0.076	0.063	0.16002	0.063	0.16002
E	0.375	0.953	0.375	0.953	0.375	0.953
F	2.5	6.35	2.5	6.35	2.5	6.35
G	0.375	0.953	0.375	0.953	0.375	0.953
H	1.55	3.94	1.55	3.94	1.55	3.94
I	1.75	4.45	1.75	4.45	1.75	4.45
J	0.19	0.48	0.19	0.48	0.19	0.48
K	0.19	0.48	0.19	0.48	0.19	0.48

The radiant heat flux from the array of silicon rod heaters directed at the lid of the can causes the polymer to decompose and the container to pressurize. Temperatures were measured during the experiment using thermocouples (TC) mounted on the exterior of the can and by embedded thermocouples in the object, lid, and base (Figure 3). A pressure transducer was used to measure pressure response during the experiment. Measurement error on thermocouples and transducer was ± 2%. X-rays were also used to observe physical changes of the foam as a function of time throughout the experiment. The experimental test series is described in Table 2. The experiment ended when the can breached due to foam decomposition pressurization of the can. Test to test variability was very small, as a result, a subset of experiments (one upright and one inverted) were selected for discussion in this paper, although all experiments were simulated.

Table 2 Experimental Test Series

Test Name	Heating Rate (°C/min)	Hold Temperature (°C)	Average Foam Density (kg/m^3)	# of Upright Tests	# of Inverted Tests
2010	200	900	146	2	2
2011-20lb	180	900	266	2	2
2011-30lb	150	900	366	2	2
2012	150	800	323	4	4
2013-10C	10	800	321	4	1
2013-50C	50	800	323	3	3

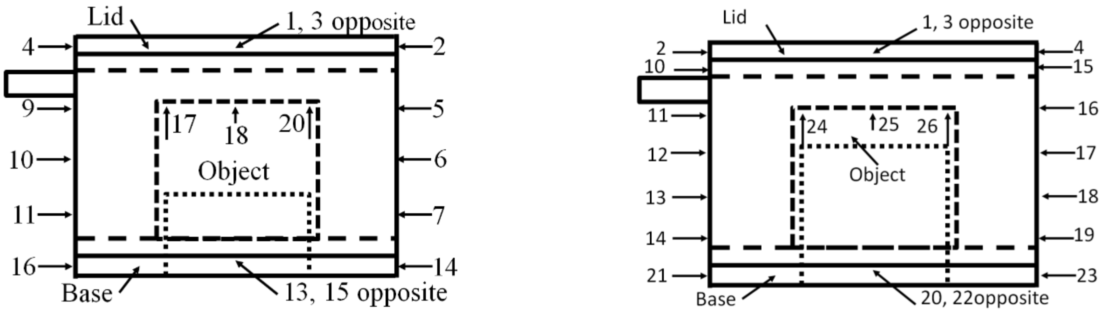

(a) (b)

Figure 3. The location of thermocouples for the (a) 2010 and 2011 and (b) 2012 and 2013 experiments. In the 2012 and 2013 experiment, there is another set of thermocouples (5-9, not pictured) on the outside of the can in the same alignment as TCs 11-14 and 15-19, only rotated 90 degrees (in line with TC 1 and 20)

2.1 Experimental Results

Figure 4 through Figure 21 temperature responses of select thermocouples along the exterior side of the can and on the embedded object as well as the pressure response for a representative inverted and upright experiment in each data set. In general, the inverted experiments tend to be shorter than the upright experiments, due to a steeper pressure rise. This orientation dependent response is caused by motion of the liquid foam decomposition products. X-ray images show that in the upright orientation the foam decomposes, liquefies and moves away from the heated plate, similar to previous experiments [2]. While in the inverted orientation, the foam liquefied decomposition products drip down onto the heated lid, increasing the rate of gasification, and thus pressurization. In addition, liquefaction and flow appear to be exacerbated by erosive channeling of hot gases and vapors penetrating into the bulk foam.

A series of thermocouples were placed on either side of the exterior of the can, separated by either 90 (2012, 2013) or 180 (2010, 2011) degrees. The plots displaying the exterior can thermocouples show circumferential variability due to the nature of the foam decomposition. However, only one series of external thermocouples will be presented in the uncertainty quantification section of this paper.

2.1.1 2010

The 2010 series of experimental consisted of four FIC tests, two in the upright and two in the inverted orientation. The units were heated to 900ºC at a rate of 200ºC/min. These experiments were vented when the internal pressure of the can reached 2.5 MPa. Descriptions of the tests performed are shown in Table 3. In general, the data presented for this test series will be confined to Upright 1 (P10-1) and Inverted 1 (P10-3).

Table 3 2010 Experimental Test Series

Experiment Name	Simulation Name	Orientation	Mass (g)	can volume (m^3)	density (kg/m^3)	density (lb/ft^3)
P10-1	Upright 1	upright	30.71	0.000207254	148.18	9.25
P10-2	Upright 2	upright	30.63	0.000207254	147.79	9.22
P10-3	Inverted 1	inverted	30.01	0.000207254	144.80	9.04
P10-4	Inverted 2	inverted	29.21	0.000207254	140.93	8.79

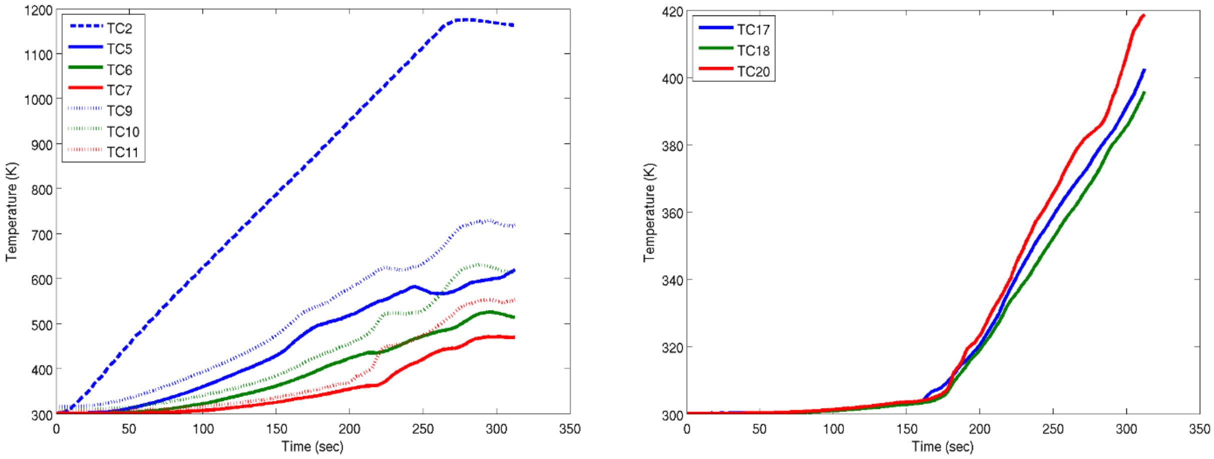

(a) (b)

Figure 4. Representative nominal experimental results: (a) temperature vs time along the external side of the can (b) temperature vs time for thermocouple the internal embedded object for the inverted configuration.

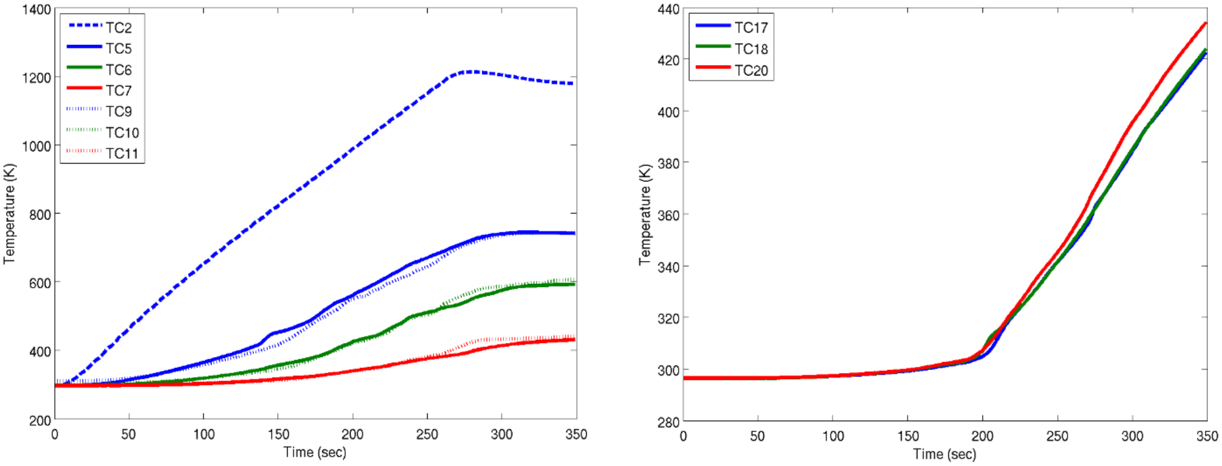

(a) (b)

Figure 5. Representative nominal experimental results: (a) temperature vs time along the external side of the can (b) temperature vs time for thermocouple the internal embedded object for the upright configuration.

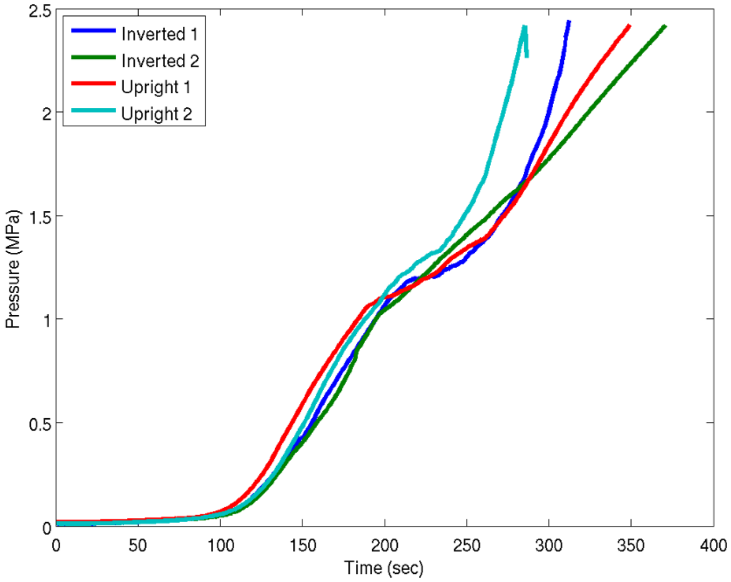

Figure 6. Nominal experimental results for upright and inverted internal can pressure vs time

2.1.2 2011-20lb

The 2011-20lb series of experimental consisted of four FIC tests, two in the upright and two in the inverted orientation. The units were heated to 900ºC at a rate of 180ºC/min. These experiments were vented when the internal pressure of the can reached 4.5 MPa. Descriptions of the tests performed are shown in Table 4. In general, the data presented for this test series will be confined to Upright 1 (P20-1) and Inverted 1 (P20-3).

Table 4 2011-20lb Experimental Test Series

Test Name	Simulation Name	Orientation	Mass (g)	can volume (m^3)	density (kg/m^3)	density (lb/ft^3)
P20-1	Upright 1	upright	51.02	0.00019498	261.67	16.33
P20-2	Upright 2	upright	52.37	0.00019498	268.59	16.76
P20-3	Inverted 1	inverted	51.88	0.00019498	266.08	16.60
P20-5	Inverted 2	inverted	51.89	0.00019498	266.13	16.61

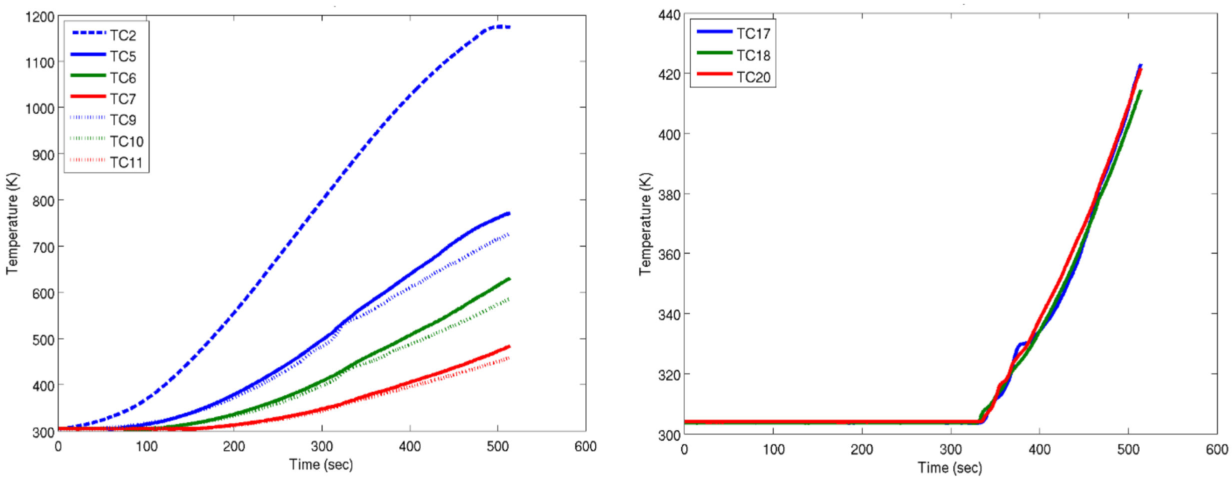

(a) (b)

Figure 7. Representative nominal experimental results: (a) temperature vs time along the external side of the can (b) temperature vs time for thermocouple the internal embedded object for the inverted configuration.

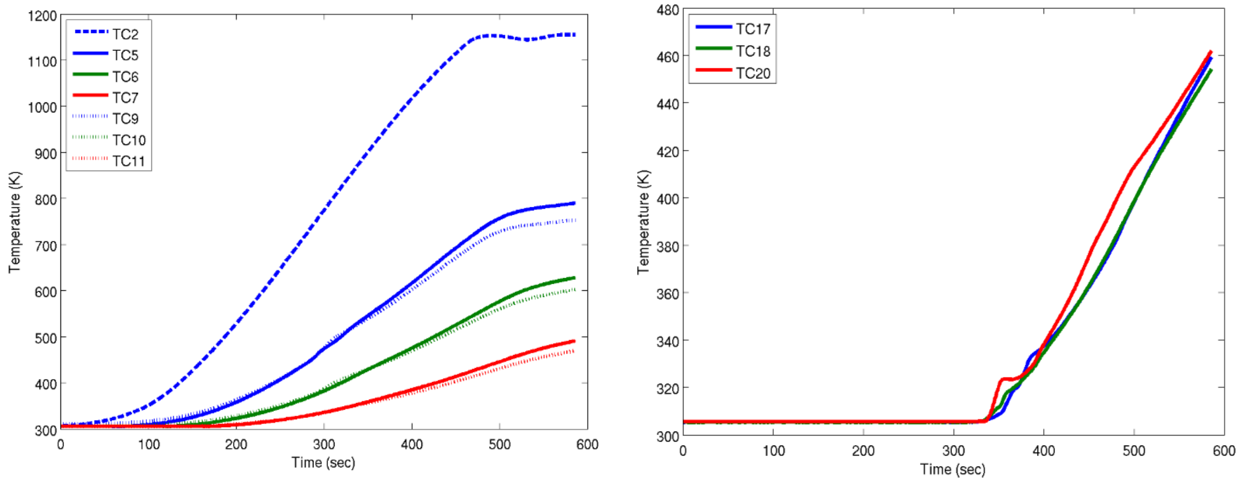

(a) (b)

Figure 8. Representative nominal experimental results: (a) temperature vs time along the external side of the can (b) temperature vs time for thermocouple the internal embedded object for the upright configuration.

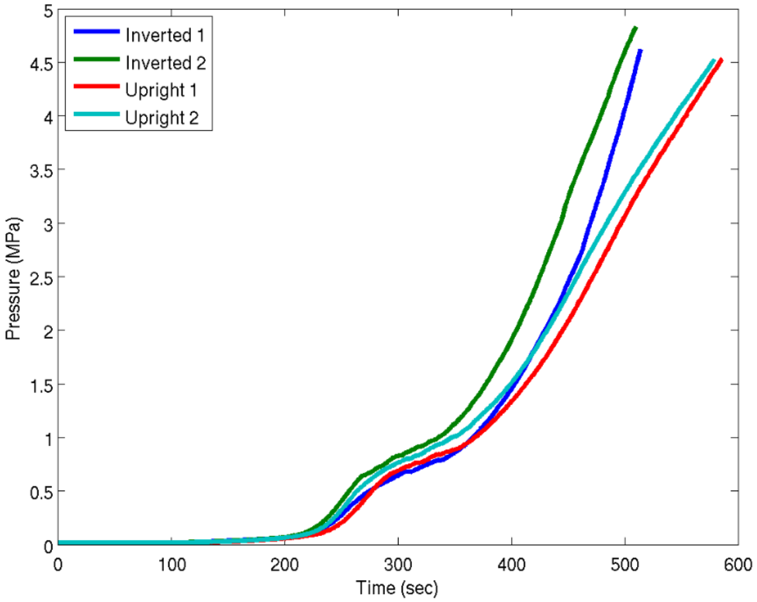

Figure 9. Nominal experimental results for upright and inverted internal can pressure vs time

Comparing the data from the 2010 and the 2011-20lb data, one notes how the more dense foam increases the amount of time required to reach 2.5 MPa. For the less dense foam, the inverted orientation reached the vent pressure in approximately 300s and in the upright orientation in ~350s. However, in this data set this occurs about 100 seconds later. The slightly lower heating rate may also have an effect on the time to pressure.

2.1.3 2011-30lb

The 2011-30lb series of experimental consisted of four FIC tests, two in the upright and two in the inverted orientation. The units were heated to 900ºC at a rate of 150ºC/min. These experiments were vented when the internal pressure of the can reached 4.5 MPa. Descriptions of the tests performed are shown in Table 5. The data presented for this test series will be confined to Upright 1 (P30-2) and Inverted 1 (P30-4).

Table 5 2011-30lb Experimental Test Series

Test Name	Simulation Name	Orientation	Mass (g)	can volume (m^3)	density (kg/m^3)	density (lb/ft^3)
P30-2	Upright 1	upright	71.51	0.00019498	366.76	22.89
P30-3	Upright 2	upright	70.45	0.00019498	361.32	22.55
P30-4	Inverted 1	inverted	70.38	0.00019498	360.96	22.52
P30-5	Inverted 2	inverted	72.99	0.00019498	374.35	23.36

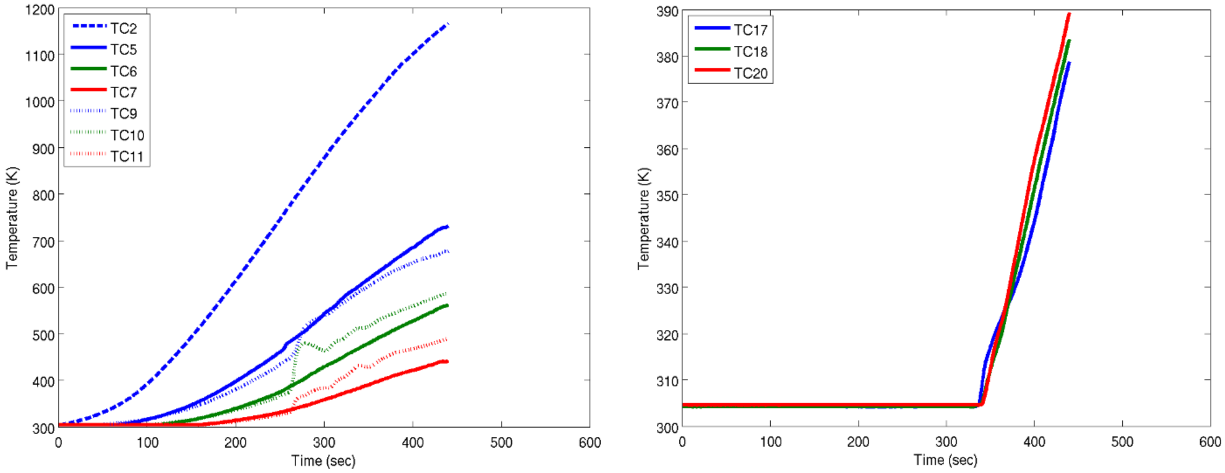

(a) (b)

Figure 10. Representative nominal experimental results: (a) temperature vs time along the external side of the can (b) temperature vs time for thermocouple the internal embedded object for the inverted configuration.

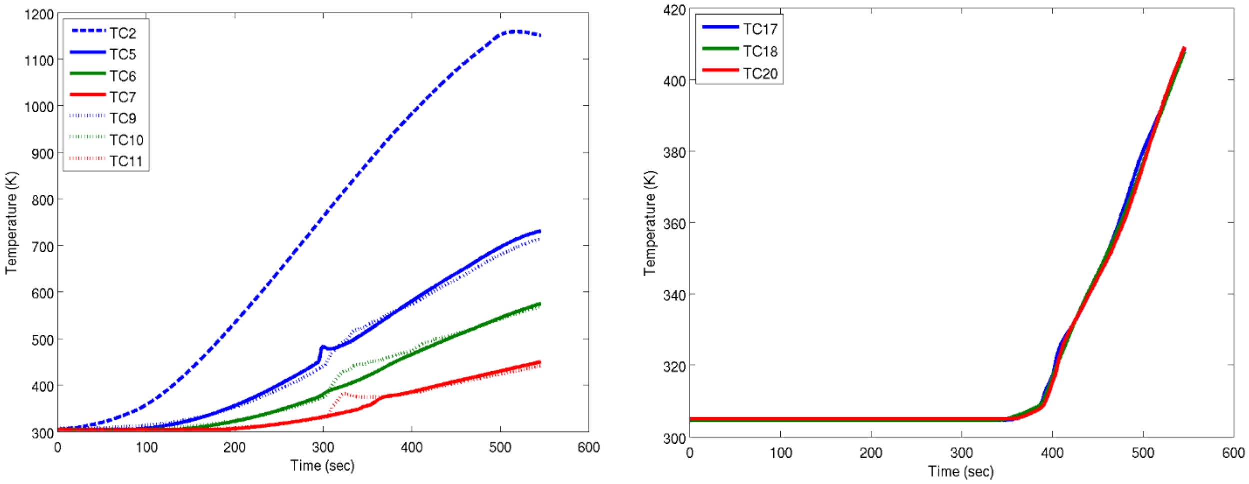

(a) (b)

Figure 11. Representative nominal experimental results: (a) temperature vs time along the external side of the can (b) temperature vs time for thermocouple the internal embedded object for the upright configuration.

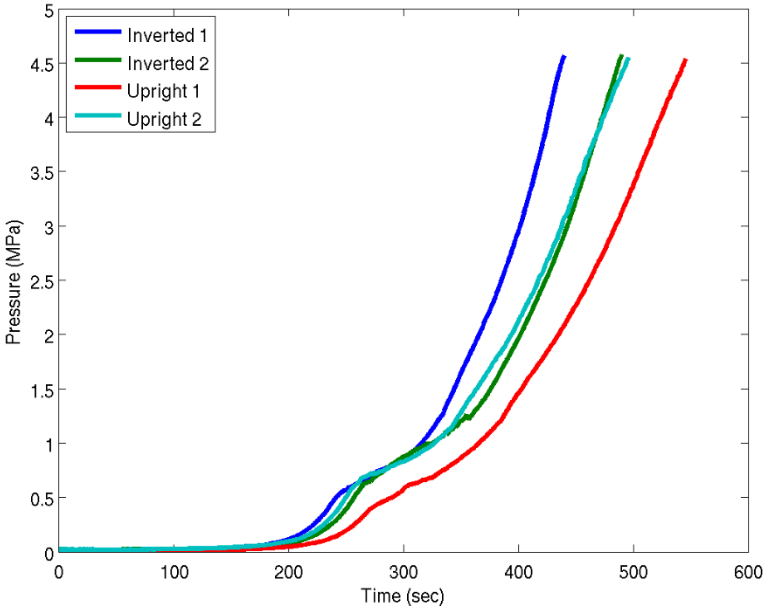

Figure 12. Nominal experimental results for upright and inverted internal can pressure vs time

2.1.4 2012

The 2012 series of experimental consisted of eight FIC tests, four in the upright and four in the inverted orientation. The units were heated to 800ºC at a rate of 150ºC/min. Descriptions of the tests performed are shown in Table 6. The data presented for this test series will be confined to Upright 1 (Can 5) and Inverted 1 (Can 22). These experiments were heated until the cans breached. This allows for higher pressure data to be collected, as shown in Figure 15. This demonstrates how the spread in the time to pressure in the only increases as the foam continues to decompose. In the 2012 and 2013 tests, the volume of the slug was reduced, thus it reacts to changes in heat flux more quickly due to a lower thermal mass. This can be observed by the change in slope seen in Figure 14b.

Table 6 2012 Experimental Test Series

Test Name	Simulation Name	Orientation	Mass (g)	can volume (m^3)	density (kg/m^3)	density (lb/ft^3)
Can 5	Upright 1	Upright	62.287	0.00019498	319.45	19.93
Can 6	Upright 2	Upright	63.727	0.00019498	326.84	20.39
Can 7	Upright 3	Upright	62.59	0.00019498	321.01	20.03
Can 8	Upright 4	Upright	63.46	0.00019498	325.47	20.31
Can 3	Inverted 3	Inverted	63.782	0.00019498	327.12	20.41
Can 4	Inverted 4	Inverted	63.077	0.00019498	323.50	20.19
Can 22	Inverted 1	Inverted	62.675	0.00019498	321.44	20.06
Can 23	Inverted 2	Inverted	63.144	0.00019498	323.85	20.21

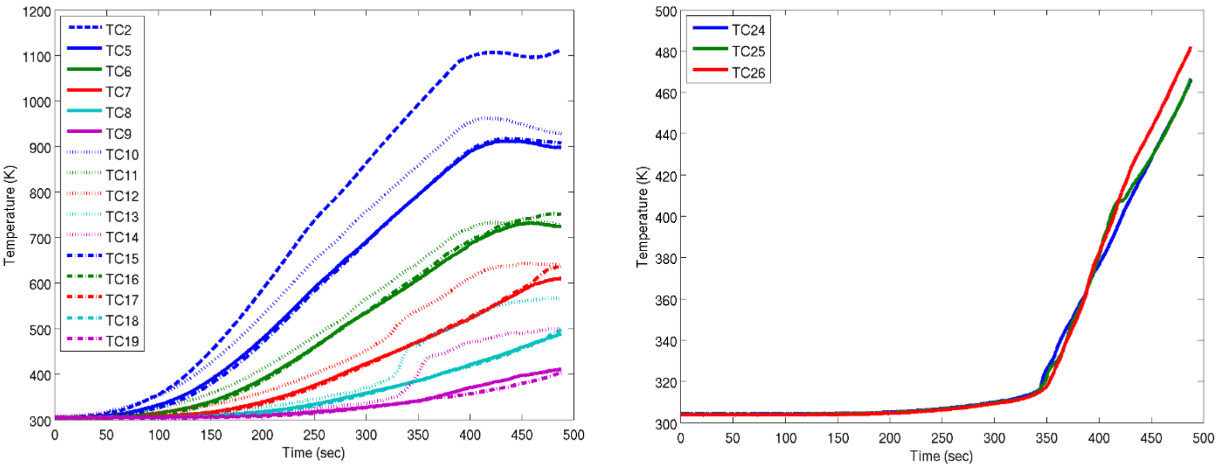

(a) (b)

Figure 13. Representative nominal experimental results: (a) temperature vs time along the external side of the can (b) temperature vs time for thermocouple the internal embedded object for the inverted configuration.

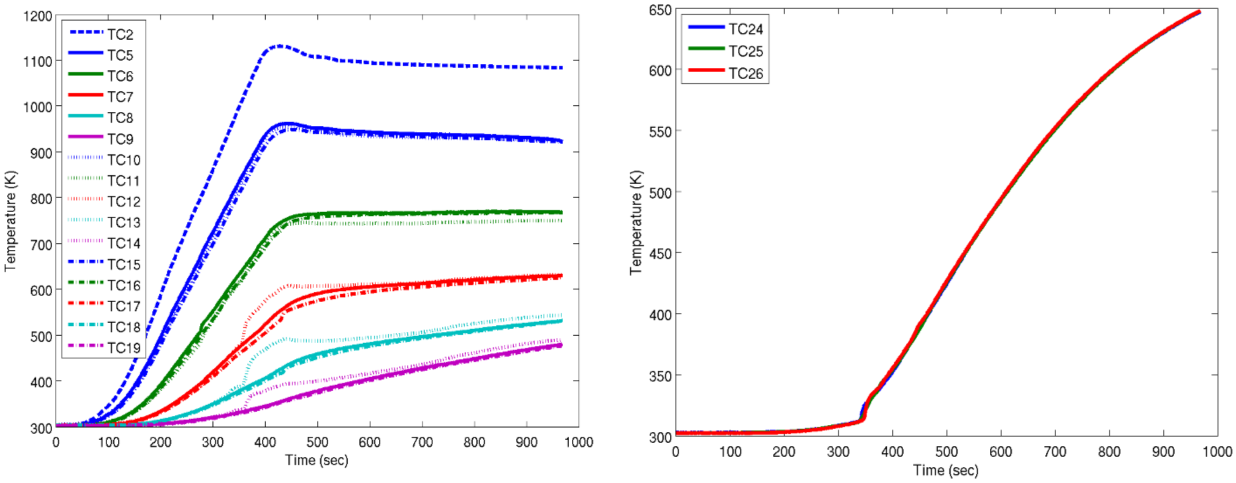

(a) (b)

Figure 14. Representative nominal experimental results: (a) temperature vs time along the external side of the can (b) temperature vs time for thermocouple the internal embedded object for the upright configuration.

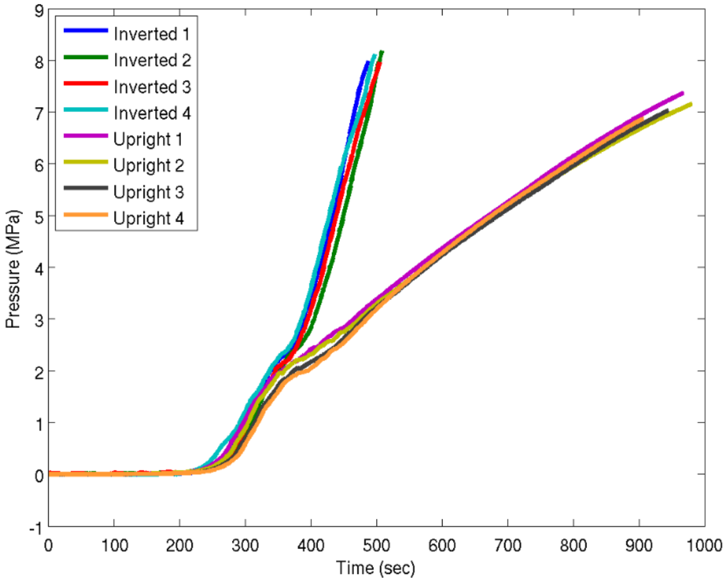

Figure 15. Nominal experimental results for upright and inverted internal can pressure vs time

2.1.5 2013-10C

The 2013-10C series of experimental consisted of five FIC tests, four in the upright and one in the inverted orientation. The units were heated to 800ºC at a rate of 10ºC/min. These experiments were heated until the cans breached. Descriptions of the tests performed are shown in Table 7. The data presented for this test series will be confined to Upright 1 (Can 11) and Inverted 1 (Can 16). Lowering the heating rate allowed for the production of a significant about the liquid decomposition products.

Table 7 2013-10C Experimental Test Series

Test Name	Simulation Name	Orientation	Mass (g)	can volume (m^3)	density (kg/m^3)	density (lb/ft^3)
Can 11	Upright 1	Upright	61.7	0.00019498	316.44	19.75
Can 13	Upright 2	Upright	64.725	0.00019498	331.96	20.71
Can 19	Upright 3	Upright	61.841	0.00019498	317.17	19.79
Can 24	Upright 4	Upright	60.552	0.00019498	310.55	19.38
Can 16	Inverted 1	Inverted	64.173	0.00019498	329.13	20.54

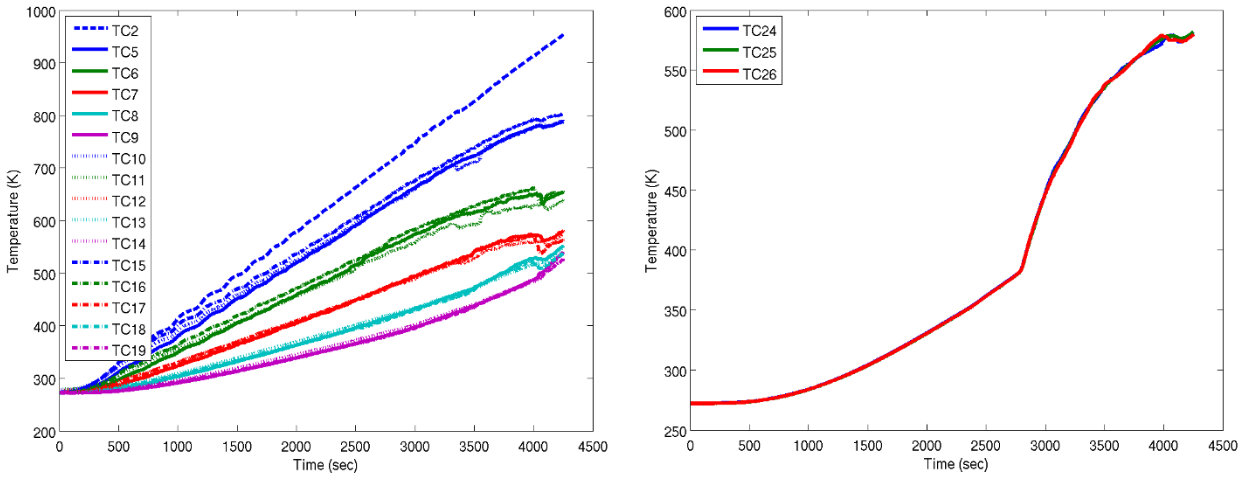

(a) (b)

Figure 16. Representative nominal experimental results: (a) temperature vs time along the external side of the can (b) temperature vs time for thermocouple the internal embedded object for the inverted configuration.

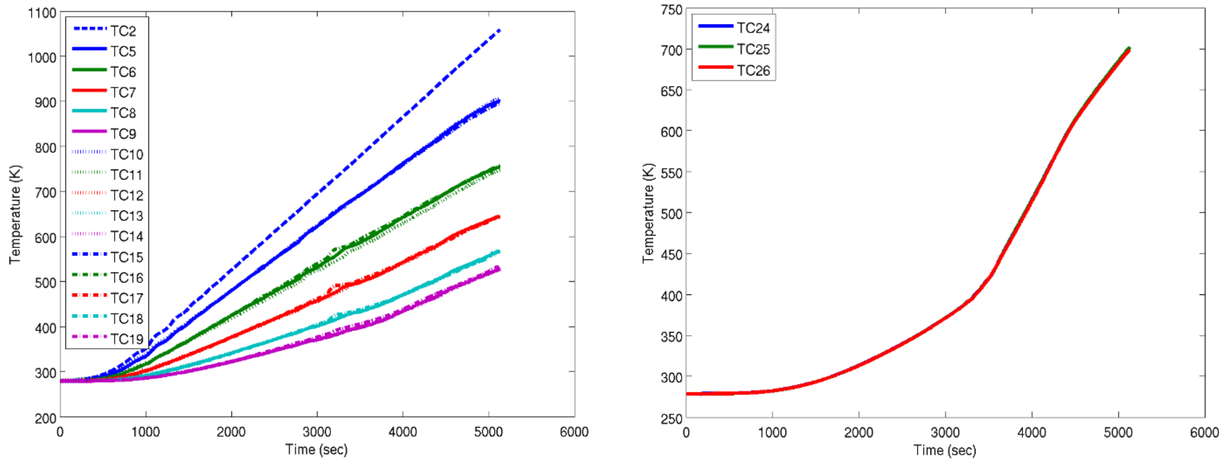

(a) (b)

Figure 17. Representative nominal experimental results: (a) temperature vs time along the external side of the can (b) temperature vs time for thermocouple the internal embedded object for the upright configuration.

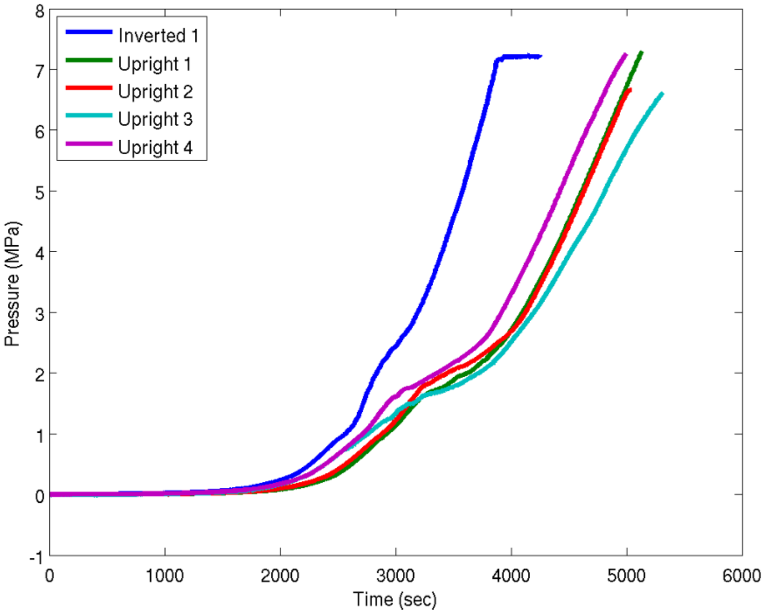

Figure 18. Representative nominal experimental results for upright and inverted internal can pressure vs time

2.1.6 2013-50C

The 2013-50C series of experimental consisted of six FIC tests, three in the upright and three in the inverted orientation. The units were heated to 800ºC at a rate of 50ºC/min. These experiments were heated until the cans breached. Descriptions of the tests performed are shown in Table 8. The data presented for this test series will be confined to Upright 1 (Can 14) and Inverted 1 (Can 10).

Table 8 2013-50C Experimental Test Series

Test Name	Simulation Name	Orientation	Mass (g)	can volume (m^3)	density (kg/m^3)	density (lb/ft^3)
Can 14	Upright 1	Upright	62.405	0.00019498	320.06	19.97
Can 15	Upright 2	Upright	62.687	0.00019498	321.50	20.06
Can 17	Upright 3	Upright	64.274	0.00019498	329.64	20.57
Can 10	Inverted 1	Inverted	62.221	0.00019498	319.11	19.91
Can 12	Inverted 2	Inverted	63.275	0.00019498	324.52	20.25
Can 18	Inverted 3	Inverted	62.954	0.00019498	322.87	20.15

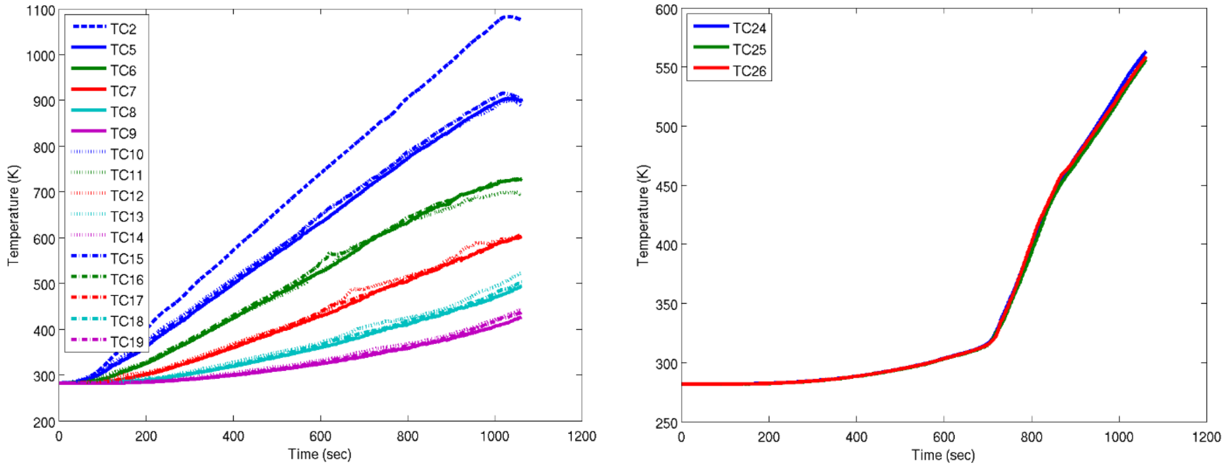

(a) (b)

Figure 19. Representative nominal experimental results: (a) temperature vs time along the external side of the can (b) temperature vs time for thermocouple the internal embedded object for the inverted configuration.

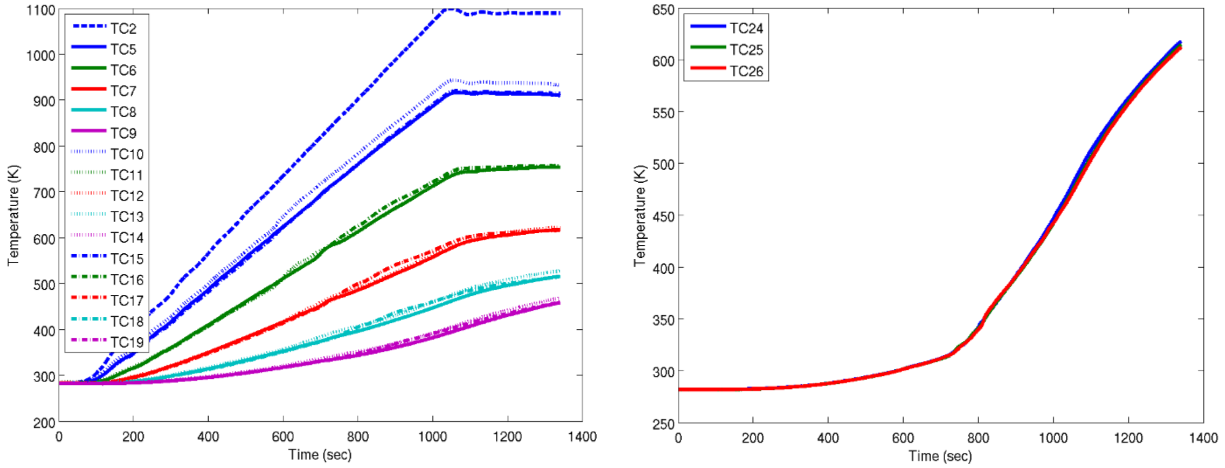

(a) (b)

Figure 20. Representative nominal experimental results: (a) temperature vs time along the external side of the can (b) temperature vs time for thermocouple the internal embedded object for the upright configuration.

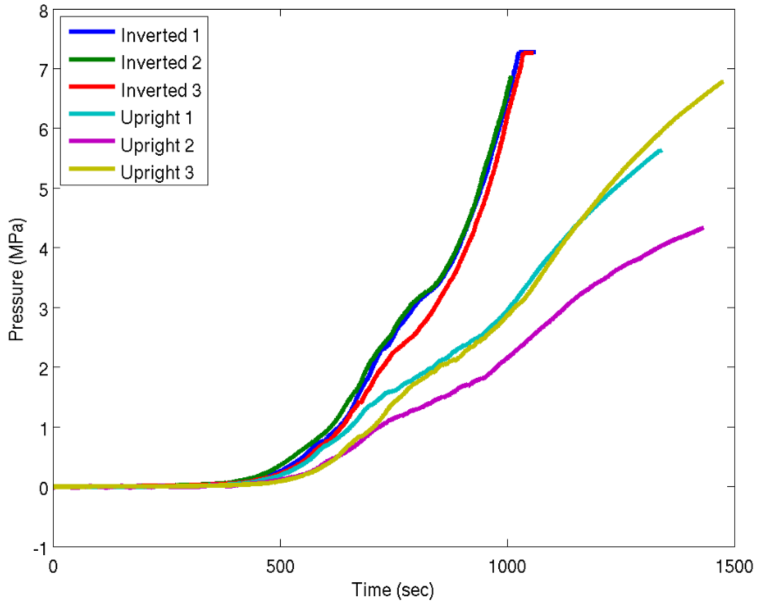

Figure 21. Representative nominal experimental results for upright and inverted internal can pressure vs time

3. COMPUTATIONAL MODEL

A 3-D finite element model composed of tetrahedral elements was evaluated in the Sierra Thermal/Fluids [5] radiation-conduction code to computationally simulate the FIC experimental configuration. The temperature response provided the basis for predicting gas-vapor generation rates and container pressure. Radiation heat transfer was modelled using the diffusion approximation. Based on the experimental results discussed above, a radiation-conduction approach has shortcomings since convective transport would accompany erosive channeling. However, this approach was used successfully to model pressurization of containers and heat transfer to objects embedded in highly charring foam that did not liquefy and flow [2].

The energy balance for heat transfer through the foam is given by

$$\rho c \frac{\partial T}{\partial t} = \nabla \bullet (k + k_e)\nabla T + \sum_i \rho r_i(-\Delta H_i) \tag{1}$$

where ρ is the bulk mass density of the foam; c is the specific heat; T is temperature; t is time; k is the thermal conductivity; k_e is an effective conductivity for radiant heat transfer in optically thick medial; r_i are the overall rates of the reactions describing formation of final condensed- and gas-phase products during foam decomposition; and ΔH_i are the overall heats of reaction of the initial foam to form final products. The equations describing reaction rates r_i and time-dependent container pressure are discussed below. The pressure was solved using a user-defined subroutine that was sub-cycled at each time step during the solution of Eq. 1.

Rate expressions for the r_i describing polymer decomposition and gas and vapor formation were based on the following reaction scheme (see Table 9). Let the polymer matrix consist of moieties $\boldsymbol{A_i}$ that decompose by different mechanisms to form species $\boldsymbol{B_{ij}}$ (where subscript j denotes the j-th species produced by decomposition of moiety $\boldsymbol{A_i}$). Let w_i^0 denote the mass fraction of $\boldsymbol{A_i}$ in the initial foam, and let ξ_{ij} denote the mass fraction of $\boldsymbol{A_i}$ that forms $\boldsymbol{B_{ij}}$. Decomposition products $\boldsymbol{B_{ij}}$ can be light gases, lower-molecular-weight organic compounds, higher-molecular-weight organic compounds, and thermally stable condensed-phase products or char.

Table 9 Decomposition Reaction Scheme.

Initial Foam $w_1^0 A_1 + w_2^0 A_2 + \ldots + w_n^0 A_n$	Reaction $\rightarrow$	Decomposition Products
$\boldsymbol{A_1}$	r_1	$\xi_{11}B_{11} + \xi_{12}B_{12} + \cdots + \xi_{1m}B_{1m}$
$\boldsymbol{A_2}$	r_2	$\xi_{21}B_{21} + \xi_{22}B_{22} + \cdots + \xi_{2m}B_{2m}$
…	…	…
$\boldsymbol{A_n}$	r_n	$\xi_{n1}B_{11} + \xi_{n2}B_{12} + \cdots + \xi_{nm}B_{nm}$

Assume that overall reaction rates r_i are approximately first order with Arrhenius-type rate constants, $k_i = k_i^0 \exp(-Q_i/RT)$, where Q_i and k_i^0 are activation energy and frequency factor, respectively, and R is the gas constant. Let w_i denote the fraction of $\boldsymbol{A_i}$ remaining at time t. Then r_i is given by

$$r_i = -\frac{dw_{A_i}}{dt} = k_i w_i \qquad (1 \ge w_i \ge 0) \tag{2}$$

Let ρ_{A_i} denote the local mass of $\boldsymbol{A_i}$ per unit bulk volume and let ρ_B^0 denote the initial bulk density of the foam. Let $\rho_{B_{ij}}$ and $\overline{\rho}_{B_{ij}}$ denote local bulk mass density and local bulk molar density, respectively, of $\boldsymbol{B_{ij}}$, and let $\overline{M}_{B_{ij}}$ denote molecular weight of $\boldsymbol{B_{ij}}$. Then,

$$\frac{d\rho_{A_i}}{dt} = \rho_B^0 w_i^0 \frac{dw_{A_i}}{dt} \tag{3}$$

$$\frac{d\rho_{B_{ij}}}{dt} = -\xi_{ij} \frac{d\rho_{A_i}}{dt} = -\rho_B^0 w_i^0 \xi_{ij} \frac{dw_i}{dt} \tag{4}$$

$$\frac{d\overline{\rho}_{B_{ij}}}{dt} = \frac{1}{\overline{M}_{B_{ij}}} \frac{d\rho_{B_{ij}}}{dt} = -\frac{\xi_{ij}}{\overline{M}_{B_{ij}}} \frac{d\rho_{A_i}}{dt} = -\rho_B^0 \frac{\xi_{ij} w_i^0}{\overline{M}_{B_{ij}}} \frac{dw_i}{dt} = \rho_B^0 \frac{\xi_{ij} w_i^0}{\overline{M}_{B_{ij}}} r_i = \rho_B^0 \frac{\xi_{ij} w_i^0}{\overline{M}_{B_{ij}}} k_i w_i \tag{5}$$

Let $\overline{\rho}'_{B_{ij}}$ denote local molar density of $\boldsymbol{B_{ij}}$ in the gas-vapor phase, and let $K_{B_{ij}}$ denote a distribution coefficient defined by $K_{B_{ij}}(T, P, ...) = \overline{\rho}'_{B_{ij}} / \overline{\rho}_{B_{ij}}$, which can be a complex function of temperature, pressure, and composition. Let $\overline{\rho}'_g$ denote the local bulk molar gas-vapor phase density of decomposition products; let n'_g denote the total moles of decomposition products in the gas-vapor phase, and let V_B^0 denote the initial bulk volume of the foam. Summing over all decomposition products

$$\overline{\rho}'_g = \sum_i \sum_j K_{B_{ij}} \overline{\rho}_{B_{ij}} \tag{6}$$

$$n'_g = \int_{V_B^0} \overline{\rho}'_g \, dV_B^0 \tag{7}$$

Equations for calculating the container pressure P are based on the ideal gas law and on the assumption that pressure gradients relax rapidly, so that pressure is independent of position (in the sealed volume) and is only a function of time. Then,

$$P = \frac{n_g R}{\int_{V_g} \frac{1}{T} dV_g} = \frac{n_g R}{\left(\int_{V_{fv}} \frac{1}{T} dV_{fv} + \int_{V'_g} \frac{1}{T} dV'_g \right)} = \frac{\left(n_{fv}^0 + n'_g + n_\phi^0 f_p \right) R}{\left(\int_{V_{fv}} \frac{1}{T} dV_{fv} + \int_{V_B^0} \frac{\Phi}{T} dV_B^0 \right)} \tag{8}$$

where n_g is the total number of moles of gas and vapor in the contiguous gas-vapor phase volume V_g; n_{fv}^0 is the number of moles of gas in the initial vacant volume in the system; n'_g is given by Eq. 7 and is the number of moles of decomposition products in the contiguous gas-vapor phase; n_ϕ^0 is the initial number of moles of gas in the cells of the foam; $V_g = V_{fv} + V'_g$; V'_g is the volume of the contiguous gas-vapor phase within V_B^0, V_{fv} is the initial vacant volume the container, and

f_p is a permeation coefficient used to designate when closed cells become part of the contiguous gas-vapor phase during, or prior to, significant decomposition of the polymer matrix.

$$V_g' = \int_{V_B^0} \Phi dV_B^0 \tag{9}$$

$$f_p = \begin{cases} f_p'(T, P, \ldots, w_{A_i}, \ldots) & SF = 1 \\ 1 & SF < 1 \end{cases} \tag{10}$$

The term $f_p'(T, P, \ldots, w_{A_i}, \ldots)$ in Eq. 10 is a complicated function of temperature, pressure, and condensed-phase composition. The solid fraction SF is given by

$$SF = \sum_i w_i^0 w_{Ai} + \sum_i w_i^0 (1 - w_{Ai}) \sum \xi_{ij}^{char} \tag{10}$$

where $\sum \xi_{ij}^{char}$ is the sum of the coefficients corresponding to the products $\boldsymbol{B_{ij}}$ that are thermally stable residues or chars. The term Φ is defined as the local value of V_g' / V_B^0

$$\Phi = \left[\phi_0 f_p + (1 - \phi_0)(1 - SF)\right] = \left[1 - \phi_0 (1 - f_p) - (1 - \phi_0) SF\right] \tag{11}$$

where $\phi_0 = V_B^0 - V_c^0$ is the initial porosity of the foam, V_c^0 is the initial volume of the polymer matrix, having initial density ρ_c^0, and ρ_g^0 is the initial density of the gas in the pores. Finally, noting that $\rho_B^0 = \phi_0 \rho_g^0 + \rho_c^0 (1 - \phi_0)$, then $\phi_0 = \left[(\rho_c^0 - \rho_B^0) / (\rho_c^0 - \rho_g^0)\right]$.

Convective and radiative boundary conditions were applied to all sides with the exception of the heated surface, which has direct view of the heating rods and thermal radiation is the dominant mechanism for coupling of the heated surface to the energy source. The silicon rod heater radiation source is idealized as a uniform far field radiation source of time-varying temperature. A PID (proportional-integral-derivative) controller modeling scheme was developed to regulate this radiating temperature to simulate the specified temperature history in the lid of the can [6].

All parameter values used to model the FIC experiments were determined from independent laboratory-scale experiments. These experiments were discussed in detail previously [2-4, 7-9]. Values for the foam specific heat and foam bulk thermal conductivity were obtained from published reports. In Table 10, the data for PMDI foam specific heat were taken from Taylor et al. [10]. In Table 11, data for bulk thermal conductivity also were taken from Taylor et al. [10]. Data for bulk conductivity given by Neet [11] and Jinn et al. [12] were similar. The value used for ρ_c^0 (density of initial polymer matrix) was estimated to be about 1500 kg/m^3.

Table 10. PMDI Foam Specific Heat.

Temperature (K)	50	296	323	373	423	473	523	>523
Specific Heat (J/kgK)	1269	1269	1356	1497	1843	1900	2203	2203

Table 11. PMDI 320 kg/m^3 Foam Bulk Thermal Conductivity.

Temperature (K)	Conductivity (W/mK)
300	0.049
523	0.071
Temp. > 523	0.071

The effective conductivity k_e for radiant heat transfer in the initial foam, denoted by k_e^0 was based on values of the absorption and scattering coefficients [13] that were determined using an integrating sphere apparatus to measure transmittance and reflectance in unreacted foam and an analytical two-flux representation for radiative transfer [14]. The resulting expression for the effective conductivity for radiative heat transfer in the unreacted PMDI-based foam is $k_e^0 = 0.003\sigma T^3$ W/mK. Because a vapor space develops between the heated plate and the reacting foam in the container, the expression for k_e in Eq. 1 was modified to mimic an increased radiation contribution during foam decomposition. The resulting expression is:

$$k_e = k_e^0 / f_{rxn}$$

$$\text{where } f_{rxn} = \sum_{i=1}^{3} w_i + \xi_{32}\left(w_3^0 - w_3\right) + \xi_{11}\left(w_1^0 - w_1\right), \text{when } \xi_{11}\left(w_1^0 - w_1\right) < \beta ,$$

$$\text{and } f_{rxn} = \sum_{i=1}^{3} w_i + \xi_{32}\left(w_3^0 - w_3\right), \text{ when } \xi_{11}\left(w_1^0 - w_1\right) \geq \beta .$$

The value of β was 0.1 for PMDI-based foam, which corresponded to nominal values of $\xi_{11}\left(w_1^0 - w_1\right)$ at which the onset of foam liquefaction appeared to occur.

Thermal decomposition chemistry of the foams was examined using thermal analysis and infrared spectroscopy techniques discussed previously [8, 9]. Resulting parameter values for PMDI-based foam are given in Table 12.

Table 12. Simplified Reaction Summary Based on Polymer Structure (PMDI).

A$_i$, r_i	w_i^0	ξ_{ij}	Decomposition Species	$M_{B_{ij}}$ (kg/mole)	ΔH_i kJ/kg	k_i^0 (s^{-1})	Q_i/R (K)
A$_1$, r_1	0.45	0.56	CO$_2$	44	0	8.0x10^{12}	21,600
		0.44	Organic vapors	80			
A$_2$, r_2	0.15	1.0	Organic vapors	120	0	1.8x10^{11}	21,600
A$_3$, r_3	0.40	0.50	Organic vapors	120	0	8.9x10^{9}	21,600
		0.50	Char	NA			

4. VALIDATION

In order to quantify the model uncertainty, a validation assessment of the computational model of the FIC experiments was performed and compared to experimental data. This section discusses the mesh resolution study used to select a appropriate mesh as well as an introduction to the mean value method and Latin hypercube sampling approach that are used to propagate uncertainty from the model input parameters to model responses such as temperature and pressure. These two methods were used to assess the uncertainty because, while both standard methods, LHS is able to capture nonlinear responses to the input parameters, unlike mean value. However, LHS requires more simulations (for a small number of parameters) to complete the study. In the case where the responses functions have a linear dependence on the input, LHS and mean value will yield approximately the same response.

The parameters that were examined in this study include material properties and boundary conditions. Specifically these were: the thermal conductivity and specific heat of the stainless steel and foam; stainless steel emissivity; density of the foam; activation energy of the decomposition reaction; temperature of the heated surface; convective heat transfer coefficient; and the far field temperature.

4.1 Mesh Resolution Study

When performing any computer analysis of partial differential equations, the continuous mathematical problem must be converted into a discrete representation. Doing so requires the generation of a mesh, which discretizes the continuous model into finite elements, for solving and storing the approximate solution. An unavoidable consequence is that information is lost relative to the original continuous problem, resulting in uncertainty. The quantification of the sensitivity of the solution to the mesh size is accomplished through a mesh resolution study involving a family of topologically similar meshes with a range of characteristic length scales. The finest mesh in the set is considered to be the ‘true’ solution, because as the mesh size decreases, the mesh-based approximations to the continuous derivatives also improve. When the coarser meshes are compared to the ‘true’ solution, the error associated with discretion can be assessed.

A mesh resolution study is performed in order to ascertain the effect of the mesh on the solution of the problem using the methodology presented in Scott *et al.* [15]. The mesh with 1024 times as many elements as the coarsest mesh was taken as the ‘true’ solution because it was the most refined mesh generated. As it is not actually the true mathematical solution, mesh convergence can only be assessed in the Cauchy sense, as discussed in Hughes [16]. Thus, the rate of convergence can be identified, but the difference between the nominal and 16x mesh only provides an estimate for the absolute difference between the numerical results and analytic solution. Two standard norms were used to assess the rate of convergence: the L_2 and L_∞ norms. The L_∞ norm is the absolute maximum difference between the two solutions, also normalized by the fine mesh. For the temperature the norm is mathematically defined as (in 1D):

$$L_{\infty} = \lim_{n \to \infty} \frac{\left(\int_{\Omega} (T_F(x) - T_C(x))^n dx\right)^{1/n}}{\left(\int_{\Omega} T_F^n(x) dx\right)^{1/n}} \tag{12}$$

where Ω is the domain, $T_F(x)$ is the temperature of the fine mesh at location x and $T_C(x)$ is the temperature of the course mesh at location x. The L_∞ norm is expected to converge as h^{-1}, where h is the mesh length scale. It provides a measure of the worst-case local error that can occur and is useful for verifying that lower dimensional parts of the mesh are accurate, such as faces and contacts. In contrast, the L_2 norm measures the mean square error between two solutions, normalized by the fine mesh, and is expected to converge as h^{-2}. It is useful for assessing the overall quality of the solution.

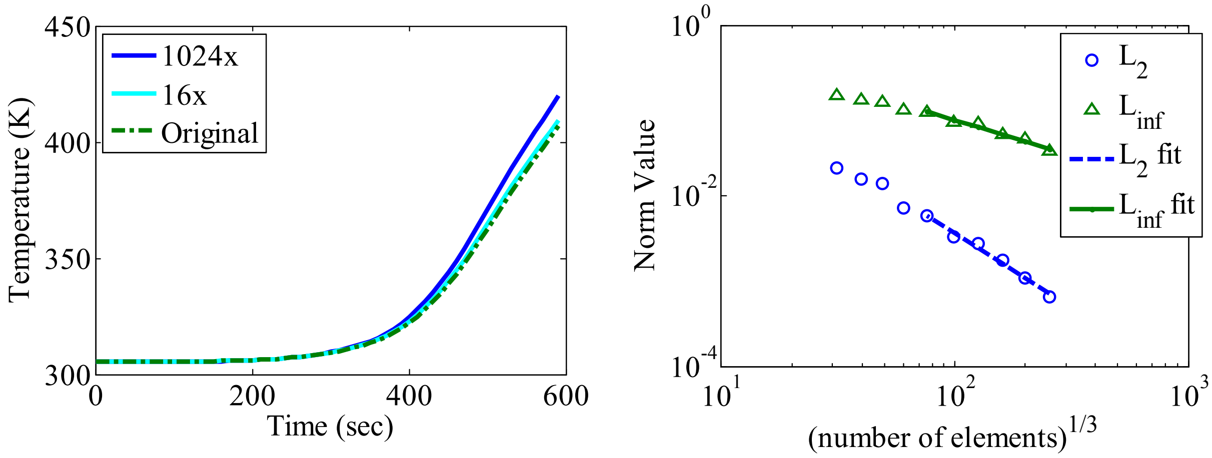

(a) (b)

Figure 22. Mesh resolution study results: (a) temperature vs time of the embedded mass for the original (coarsest) mesh and for the 32x and 1024x more elements than the original mesh and (b) L_2 and L_∞ norms with best fit lines (L_2 best fit slope = -1.76 (R^2 = 0.99), L_∞ best fit slope = -0.83 (R^2 = 0.97)).

Solution trends are presented in Figure 22a showing a comparison of the temperature fields at a location of interest for three different mesh resolutions. Although only one location is shown, all the temperature measurements converged in a similar manner. While Figure 22a qualitatively indicates convergence, the L_2 and L_∞ norms shown in Figure 22b quantitatively prove it. According to Hughes [16], when plotted on a log-log scale, the slope of the best fit lines in this Figure 22b should be -1 for L_∞ and -2 for L_2 to show convergence. The series of tested meshes have an L_2 convergence rate of -1.76 and a L_∞ convergence rate of -0.83, which is close to the theoretical expected values in [16]. Based on the results, it was determined that a mesh with an element edge length of approximately 2mm (or 16 times more elements than the coarsest mesh) was optimal, since it is within the linear convergence regime, but at the coarse end, allowing for shorter computation times.

4.2 Mean Value Method (MV)

The mean value method is one of the methods used to propagate uncertainty through the model. This approach requires input of gradients of the response functions (*i.e.* temperature, pressure) with respect to the input parameters (*e.g.* thermal conductivity of the foam). In other words, each input parameter is perturbed in order to understand the effect of the perturbation of the response. The advantage of this method is that $2n+1$, where n is the number of parameters, simulations must be run in order to complete the study. However, since the formulation assumes a linear response, this method is only acceptable for a subset of problems. For this study, processing of the input files and the responses was performed using Microsoft Excel and a series of MATLAB and Python scripts.

Let a vector representing mean values of N normalized parameters of interest to the problem be defined as $\mathbb{P}$ where each parameter is (P_i). A vector of M responses, defined as $\mathbb{R}$, represents the responses of the simulation. For the current effort, responses are measured temperatures and the pressure. All of the parameters (P) are constant through a model run and the responses are all functions of time. In the case of temperature dependent properties, parameters are applied as a multiplier on the nominal value, i.e., thermal conductivity, $k(T) = P_k k_{nom}(T)$. The sensitivity of the j-th response to the i-th parameter is estimated by central differencing as:

$$\frac{\partial R_j}{\partial P_i} \approx \frac{R_j(\mathbb{P} + \delta P_i) - R_j(\mathbb{P} - \delta P_i)}{2\delta P_i} \qquad (13)$$

Where $R_j(\mathbb{P} + \delta P_i)$ and $R_j(\mathbb{P} - \delta P_i)$ represent the j-th responses for the system with the i-th parameter incremented up by δP_i and down by δP_i respectively, where δP_i is the perturbation of the parameter. The sensitivity has the same units as the corresponding response variable. For example, if the response is a temperature (K), its sensitivity with respect to a parameter is the change in temperature (K) per fractional change in the parameter. Estimates of the standard deviations of the parameters are represented by the vector, defined as $\boldsymbol{\sigma}$. The variance for the system response considering all the parameter uncertainties is estimated as:

$$\sigma_{R_j}^2 = \sum_{i=1}^{N} \left(\frac{\partial R_j}{\partial P_i} \sigma_i \right)^2 \qquad (14)$$

Dividing by $\sigma_{R_j}^2$ gives a relative contribution of each parameter to the variance such that:

$$I_{ij} = \left(\frac{\partial R_j}{\partial P_i} \frac{\sigma_i}{\sigma_{R_j}} \right)^2 \qquad (15)$$

is the *importance* of the i-th parameter to the j-th response. Additional metrics were formed using the importance parameters to filter out parameters that exhibit importance during times where no response has occurred. $\mathbb{I}_{ij}$ is a time-averaged-response-weighted version of importance which accrues value during the transient only when response is coincident with importance and is defined as:

$$\boxed{I}_{ij} = \frac{1}{T\left|R_j(t) - R_j(0)\right|_{max}} \int_0^T \left|R_j(t) - R_j(0)\right| I_{ij} dt \qquad (16)$$

where T is the duration of the analysis. This allows for a single value to represent each input parameters *contribution to the total uncertainty*.

The input parameter variation used in the mean value method is shown in Table 13. The values in Table 13 came from engineering judgment and in the case of foam activation energy an assessment of the variability to the decomposition kinetics through comparison to TGA data.

Table 13. Input parameters use in mean value method.

Input parameter	σ_i	δP_i	**Input parameter**	σ_i	δP_i
Material Properties	0.1	0.1	Convective heat transfer coefficient	0.2	0.2
Far field temperature	0.05	0.05	Temperature of heated surface	0.01	0.01
Foam Density	0.01	0.01	Foam Activation Energy	0.02	0.02

In the chemistry model, pressure increase is a result of gas product production due to pyrolysis reactions that occur because of an increase in temperature within a constrained volume. In the current model formulation, the transport properties in the model are independent of pressure, i.e., the simulation response is independent of the pressure response. Consequently, it was convenient to consider additional uncertainty for the pressure response outside of the model manipulated for UQ. The foam decomposition model has model form errors associated with it due to physics that are not incorporated into the model. To compensate, additional model form errors have been added to uncertainty in the pressure prediction. The model form errors aim to account for discrepancies in the volume that the gas occupies, the amount of material in the gas phase, the reaction temperature, and the temperature of the gas. The volume available to the gas is uncertain because the foam is initially closed cell and the pore structure opens as pressure and temperature increase. In addition, the formation of liquid and potentially a liquid layer influences the volume available to the gas. When PMDI decomposes, it produces smaller polymer fragments that can be distributed between the gaseous and liquid phases depending upon pressure and temperature and a vapor-liquid equilibrium balance. In this model, thermal equilibrium between phases is assumed, and the heat transfer through the foam has errors associated with it, therefore the temperature at which reactions occur is uncertain, thus causing the moles of gas calculated to be uncertain. The magnitude of additional uncertainty was calculated as a multiplier based on the individual uncertainty contributions. Model form errors were assigned with minimum and maximum multipliers: the amount of material in the gas phase has a multiplier of 0.83 to 1, the temperature of the gas associated with the number of moles of gas produced has a multiplier of 0.8 to 1.2, the volume that the gas occupies has a multiplier of 0.83 to 1.0, and the temperature of the entire gas phase has a multiplier of 0.9 to 1.1. Combining the minimum and maximum values in the ideal gas equation and calculating the pressure results in estimated bounds of uncertainty from 50.4% to 264% of the nominal prediction. Since this error dominates the other sources of uncertainty, the results will be presented both with and without this error included.

4.3 Latin Hypercube Sampling (LHS) Approach

A fundamental assumption of the mean value method for propagating model input uncertainty is a linear dependence of the model response on the input parameters. By approximating the gradients with central differences and a relatively large perturbation, which is comparable to the standard deviation in most parameters, the linearity over an appropriate range of the inputs can be studied. Over the perturbation range, the model closely approximates a linear dependence on the parameters. A LHS approach (which does not rely on linearity) is applied and compared with the results from the mean value method. If the model is linear in the parameters, the LHS and mean value methods should be in close agreement. See Saltelli *et al.* [17] and Helton and Davis [18] for a description of the LHS method. The LHS approach and processing of the responses was performed using DAKOTA [19] and a series of MATLAB and Python scripts.

In a LHS approach, a cumulative distribution function (CDF) is specified for each parameter. Each CDF is divided into n_{LHS} intervals of equal probability. A random sample is generated from each interval for all parameters. This results in a vector of length n_{LHS} samples for each parameter

$$p_i = [p_{i,1}, p_{i,2} \cdots p_{i,n_{lhs}}]^T \tag{17}$$

The samples for each parameter are randomly combined with samples from the other parameters to give n_{LHS} random parameter vectors. The simulation is run with each of the random parameter vectors. The model response (i.e. temperature, pressure) for each random parameter vector is processed to calculate statistics (mean and standard deviation).

$$\mu_R = \frac{1}{n_{lhs}} \sum_{i=1}^{n_{lhs}} R_i \tag{18}$$

$$\sigma_R = \left[\frac{1}{n_{lhs} - 1} \sum_{i=1}^{n_{lhs}} (R_i - \mu_r)^2 \right]^{1/2} \tag{19}$$

where the response R_i is the model run i with the random parameter vector (p_i). The LHS method requires specifying a distribution for each parameter. Because data are not available to formulate a distribution, a functional form is assumed. As a first estimate, a truncated normal distribution for each parameter is assumed with a mean and standard deviation shown in Table 14. Similar to the mean value method implementation, the mean is assumed to be a value of 1 that is multiplied by the nominal parameter values (i.e., thermal conductivity, $k(T) = p_i k_{nom}(T)$). The number of LHS samples was selected at a value of 50.

Table 14. Input parameters use in LHS method.

Input parameter	σ_i	**Input parameter**	σ_i
Material Properties	0.1	Convective heat transfer coefficient	0.2
Far field temperature	0.05	Temperature of heated surface	0.01
Foam Density	0.01	Foam Activation Energy	0.02

When a LHS approach is used, correlation coefficients (similar to importance factors in the mean value method) can be directly calculated provided that $n_{LHS} \geq n_p$. The correlation coefficients are computed using the following equation:

$$r^2 = \left[\frac{\sum_{i=1}^{n_{LHS}} (p_i - \overline{p})(R_i - \overline{R})}{n_{LHS}\sigma_R\sigma_p} \right]^2 \tag{20}$$

where n_{LHS} is the number of samples, R_i is the value of the response of interest for the i^{th} simulation, $\overline{R}$ is the mean value of the response, p_i is the value for the i^{th} parameter, $\overline{p}$ is the mean value of the input parameter, σ_R is the standard deviation of the mean value of the response, and σ_p is the standard deviation of the mean value of the parameter. This approach assumes a linear correlation between the response and the parameter and is also referred to as the Pearson correlation coefficient. The degree of linearity can be examined through scatter plots of the responses, which will be discussed when presented in section 5.2.

5. RESULTS

In the following sections, the results from both the mean value method and the Latin hypercube sampling approach will be discussed. Then, a section comparing the results from each method will be presented. When the computational model is compared to the experiments, they are considered to be in good agreement if the experimental results are within the error bars of the simulation. In general, model and experimental results compare well for temperature responses of interest (i.e. the embedded mass temperature), however there is a large discrepancy in the pressure prediction response. The pressure discrepancy has a number contributing factors: (1) the functional form and associated parameter values used to represent material properties and foam decomposition kinetics; (2) the diffusive approximation for radiative heat transfer, and (3) fluid motion and convective heat transfer involving both gas-vapor and liquid phases. All three sources affect the time-dependent temperature distribution in the gas-vapor phase and the condensed phase, which ultimately determines the total number of moles of decomposition products and the volume of the contiguous gas-vapor phase, and thus the pressure. The temperature discrepancies can be attributed to modeling choices such as a constant heat transfer coefficient and a simplified model of the weld region. Variation of parameter values and functional forms of material properties and decomposition rates could shift the response to match experimental data better, however, the current functional form of the model leaves out motion of the decomposition front, fluid motion, and gravity. A different approach to radiative heat transfer could improve agreement, but most likely would not address all discrepancies. A model that includes fluid motion and convective heat transfer involving both gas-vapor and liquid phases is the only mechanism by which temperature distributions and, therefore, the number of moles of decomposition products would change with orientation (due to channeling by hot gases and liquefaction and flow of a condensed phase, either toward or away from a heat flux) and will be considered for future model enhancements.

In the following section, it will be shown that the LHS and mean value methods for propagating uncertainty yielded approximately the same results. This supports that for this problem, the linear assumption is valid. However, LHS provides additional data, scatter plots shows the response for each LHS run as a function of the parameter variation, which yield additional insight into the problem.

The results of this study allow for a better understanding of how input parameter variation affects the responses. With this knowledge, supplementary experiments can be performed and additional physics added to the computational model. In addition, characterizing the error in this experiment allows for confidence to be built in the model and an understanding of modeling limitations as it is utilized in more complex geometric configurations.

5.1 Mean Value Method

The computational model results with mean value generated uncertainties and the experimental results for select thermocouples and for pressure in the upright and inverted orientations are compared in Sections 5.1.1 through 5.1.6. These results are shown with $\pm 2\sigma_R$ propagated uncertainty for the computational results and ±2% error for the experimental results (*e.g.* Figure 23). Generally there is good agreement between the computational and experimental results, especially for thermocouples farther from the heated surface. For the locations closer to the heated surface, the model tends to over predicts the experimental response. In these simulations, a constant convective heat transfer coefficient was used for all locations. Using a temperature dependent value could potentially alleviate this mismatch. In addition, the thermal model geometry has been simplified such that there is no gap between the lid of the stainless steel can and the walls. There is a weld in this region, but there is also potential for a gap and contact resistance between portions of these surfaces.

The inverted and upright experimental and model pressure response is also shown in Sections 5.1.1 through 5.1.6. There is very little difference between the upright and inverted model response, which is to be expected given the modeling assumptions. The model tends to under predict the pressure response in the inverted case and over predict the pressure response in the upright case. The model assumes that all of the decomposition products reside in the gas phase and that all of the volume in both the reacted and unreacted pore space is available to the gases. In addition, since the model does not take gravity into account, there is fundamentally no difference between the upright and inverted simulations, except for the heating boundary condition that is applied (since that matches the individual experiment). These assumptions do not differ between models, and as a result, the predictions are very similar between the upright and inverted simulations. Furthermore, in the inverted case, the model does not predict the change in slope in pressurize response seen in many of the experiments. This is most likely due the computational model excluding physics such as the flow of liquid decomposition products and the distribution of decomposition products between the gaseous and liquid phases. These can be accounted for by additional model form errors associated with the distribution of the decomposition products between liquid and gaseous phases, the volume available for the gases to occupy, and the error in the temperature of the gases. This additional 'error' contribution to the pressure is shown alongside the uncertainty without this addition (*e.g.* Figure 26).

By investigating sensitivity for each input parameter for a given response, the effect of uncertainty in the value of that parameter on the simulation results can be quantified. This data is presented to two forms. The first is the value defined in Eq. 16, which is a time averaged version of the importance (*e.g.*, Figure 27). This view of the data allows for the *overall* importance of each parameter to be evaluated. The second presentation is the importance (Eq. 15) vs time for each parameter (*e.g.*, Figure 30). This gives information as to how each parameters importance varies over the time history of the experiment. The results of this analysis show that the dominant importance factor is dependent on the model response that is being investigated. When measuring the response of pressure, the activation energy for foam decomposition followed by the conductivity and specific heat of the foam dominates the importance factors. This was true in both the upright and inverted cases. When measuring the response of temperature on the outside of the can the conductivity of steel is dominant followed by the specific heat of the steel; while for the embedded object it is the effective conductivity of the foam, the activation energy of the foam, and the specific heat of the steel dominate for both the inverted and upright cases. For both temperature and the pressure response, early in time, the temperature of the environment is dominate because the flow of heat from the heated surface has not yet reached the location of interest or pressure has not begun to increase yet.

5.1.1 2010

As shown in Figure 23(a) and Figure 24(a), the model is under predicting the can wall temperature for the 10lb foam. The slight erratic experimental temperature history indicates that the foam decomposition is playing a large role in the temperature at a given. This may indicate that unmodeled physics, such as liquefaction and channeling, play a larger role when the density of the foam is lower. However, as shown in Figure 23(b) and Figure 24(b), the temperature prediction of the for the imbedded object is better, if still under predicting in the inverted case.

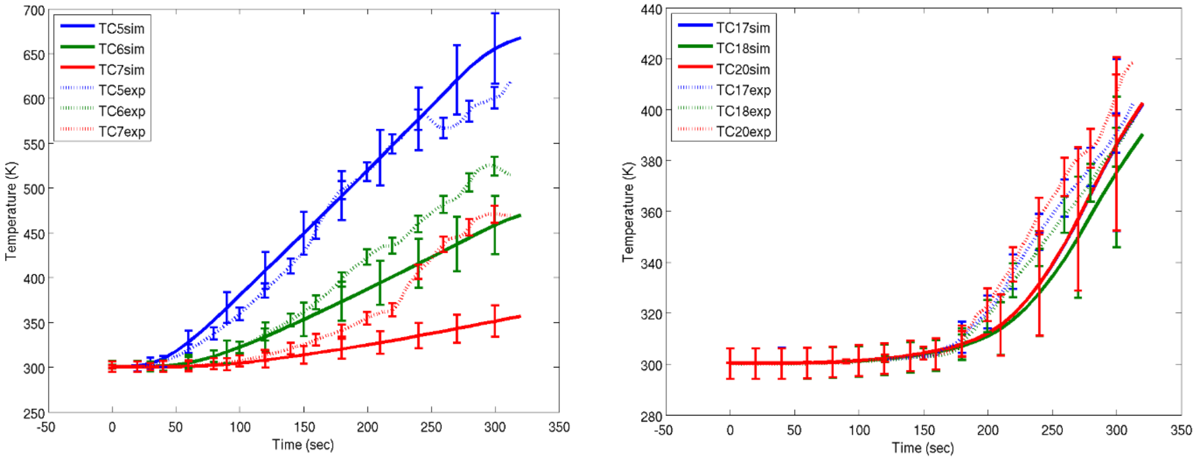

(a) (b)

Figure 23. Inverted Orientation. Computational results (solid) with ±$^{2\sigma_{R}}$ uncertainty and experimental results (dashed) with ±2% error for temperature vs time in the (a) exterior side thermocouples temperature and (b) the embedded object.

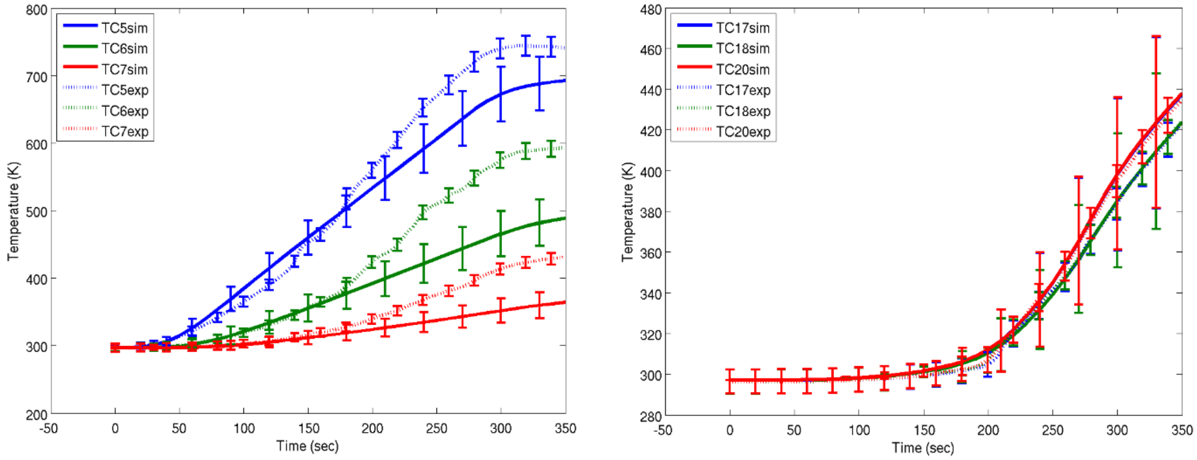

(a) (b)

Figure 24. Upright Orientation. Computational results (solid) with ±$^{2\sigma_{R}}$ uncertainty and experimental results (dashed) with ±2% error for temperature vs time in the (a) exterior side thermocouples temperature and (b) the embedded object.

Figure 25 and Figure 26, which show the pressure response for the upright and inverted scenarios. In both cases, the pressure is over predicting. This over prediction may be a result of the modeling assumption that there is no contact resistance between any of the can components (*e.g.* the foam and the can). This would allow the foam to heat up quicker and thus start decomposing sooner. Since this experiment was vented at a lower pressure than any of the other data sets, this effect is more noticeable.

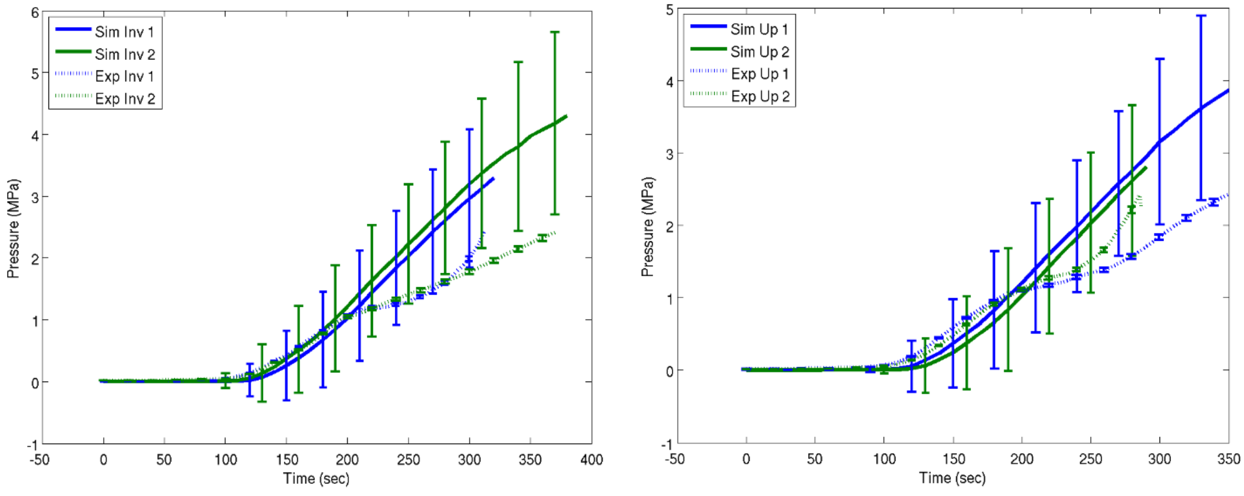

(a) (b)

Figure 25. Computational results (solid) with $\pm 2\sigma_R$ uncertainty and experimental results (dashed) with ±2% error for pressure vs time for the (a) inverted and (b) upright orientations.

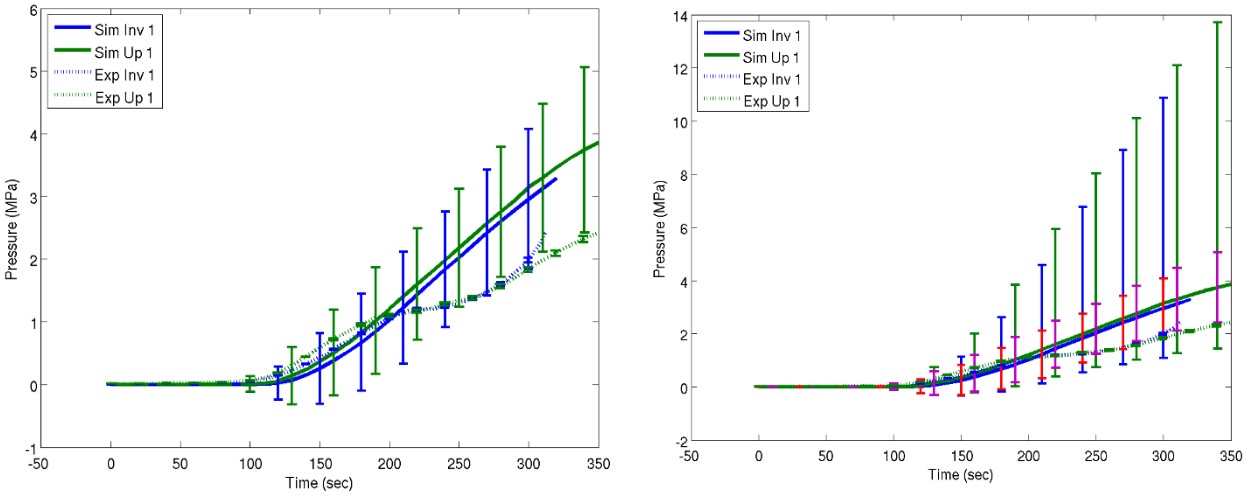

(a) (b)

Figure 26. (a) comparison between representative upright and inverted computational results (solid) with $\pm 2\sigma_R$ uncertainty and experimental results (dashed) with ±2% error for pressure vs time and (b) comparison between representative upright and inverted computational results (solid) with $\pm 2\sigma_R$ uncertainty with pressure multiplier included and experimental results (dashed) with ±2% error for pressure vs time with original uncertainties overlaid in red (upright) and purple (inverted)

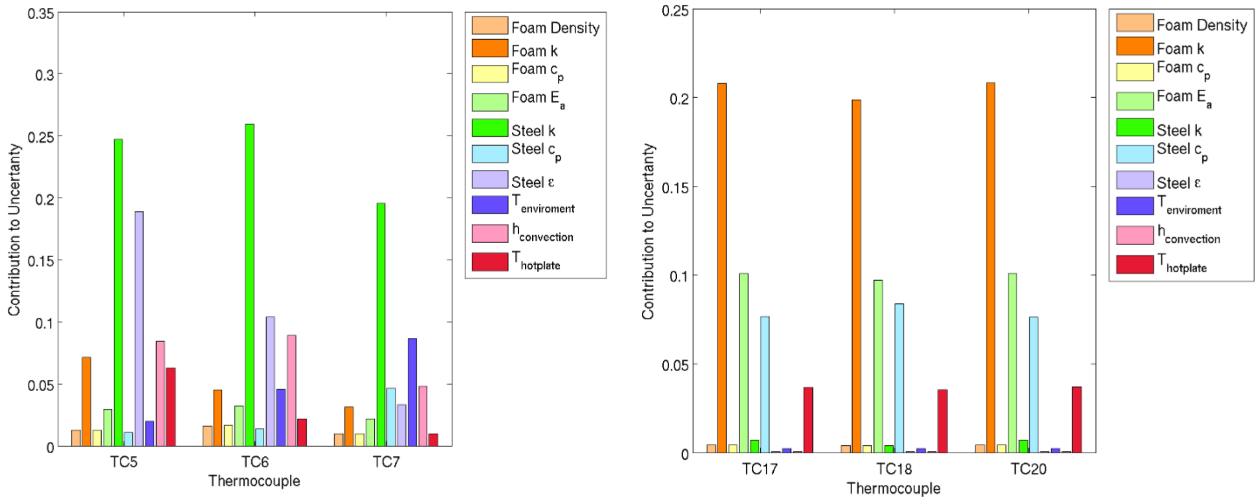

(a) (b)

Figure 27. Contribution to uncertainty for thermocouples (a) along the exterior side (b) on the embedded object for the inverted configuration.

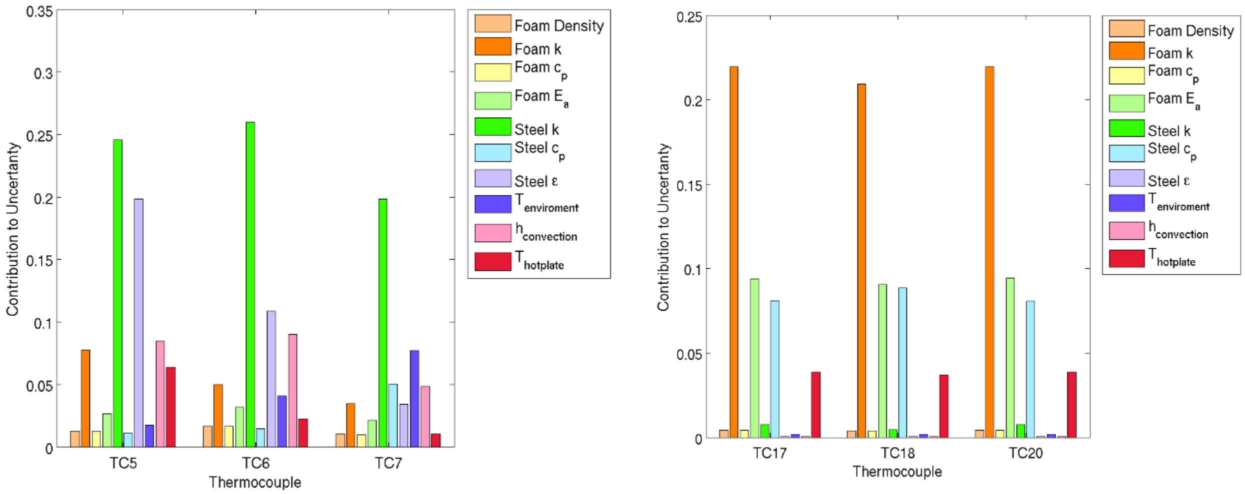

(a) (b)

Figure 28. Contribution to uncertainty for thermocouples (a) along the exterior side (b) on the embedded object for the upright configuration.

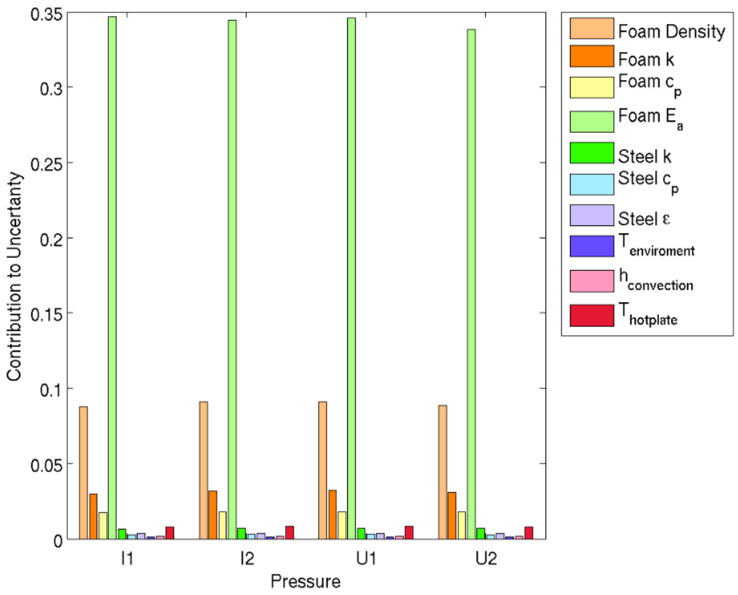

Figure **29. Contribution to uncertainty for pressure**

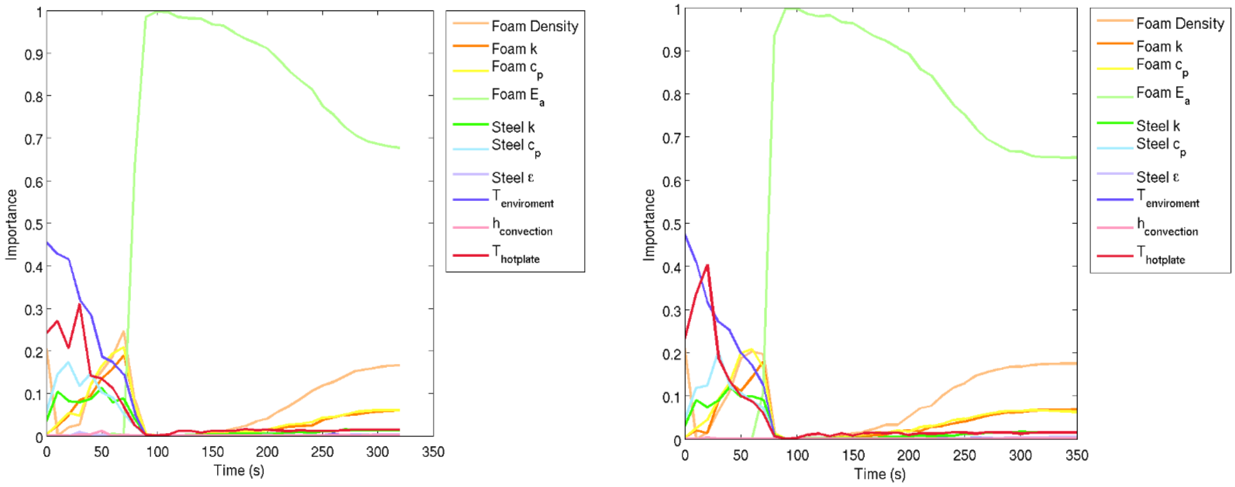

(a) (b)

Figure 30. Parameter importance vs time for pressure for (a) inverted and (b) upright.

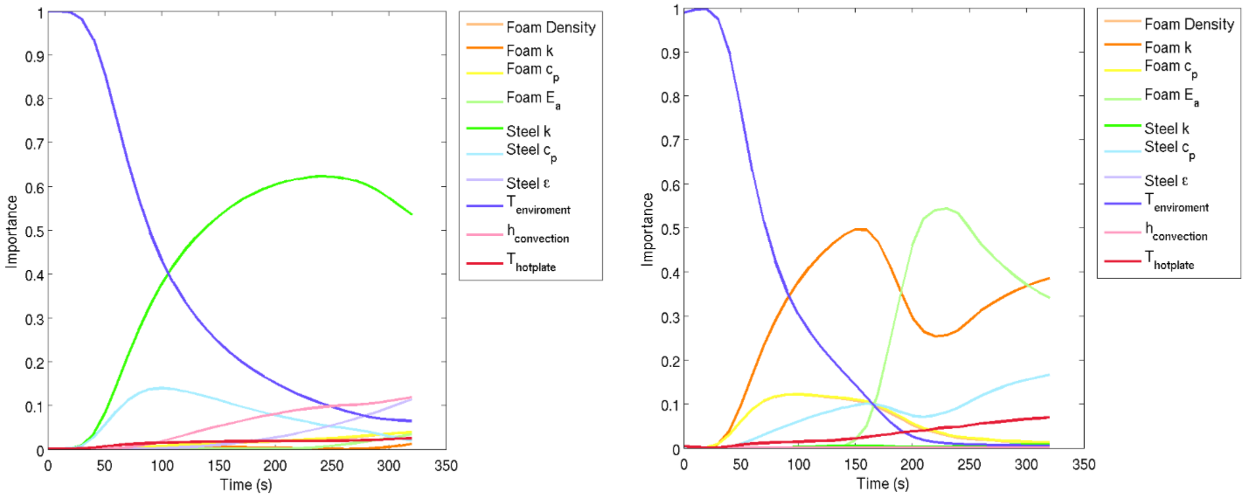

(a) (b)

Figure 31. Parameter importance vs time for (a) TC 6 and (b) TC 18 for the inverted configuration.

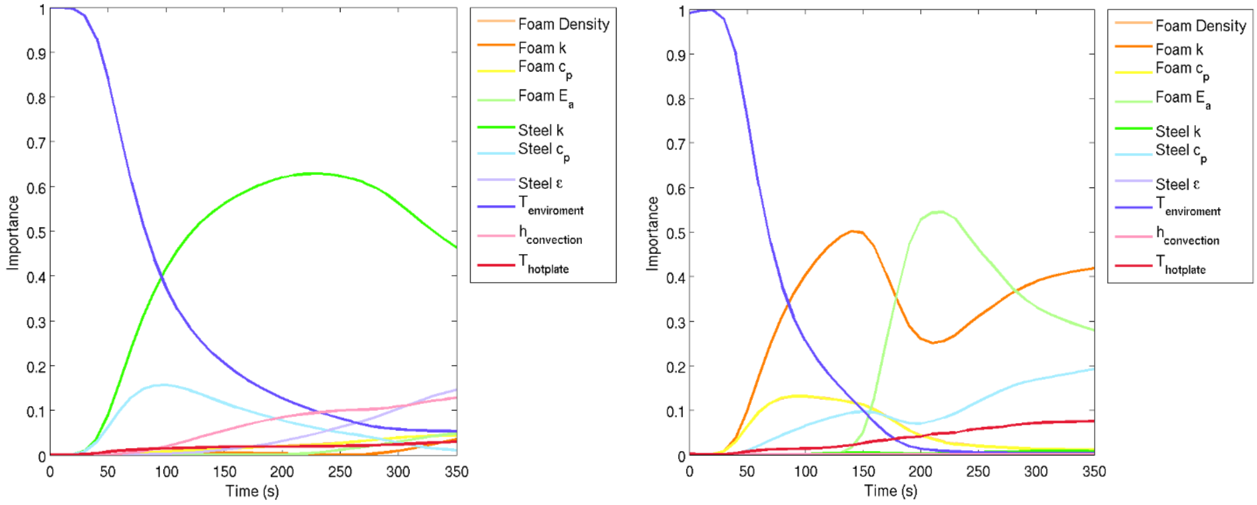

(a) (b)

Figure 32. Parameter importance vs time for (a) TC 6 and (b) TC 18 for the upright configuration.

5.1.2 2011-20lb

In this dataset, the temperature on both the sides of the can and the embedded object agree better than in the 2010 dataset (Figure 33 and Figure 34). However, the temperature is still over predicating on the sides of the can, as in most of the data sets.

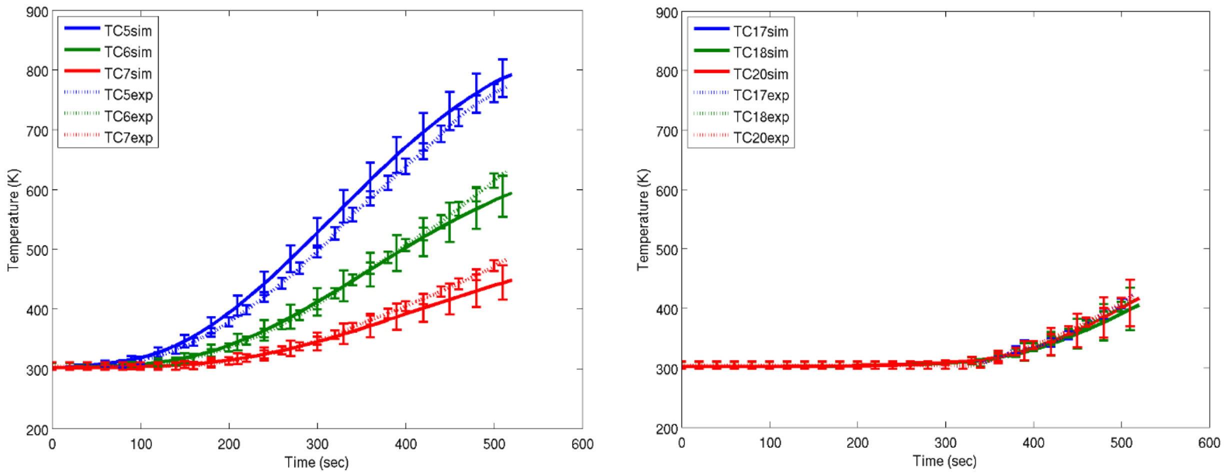

(a) (b)

Figure 33. Inverted Orientation. Computational results (solid) with $\pm^{2\sigma_R}$ uncertainty and experimental results (dashed) with ±2% error for temperature vs time in the (a) exterior side thermocouples temperature and (b) the embedded object.

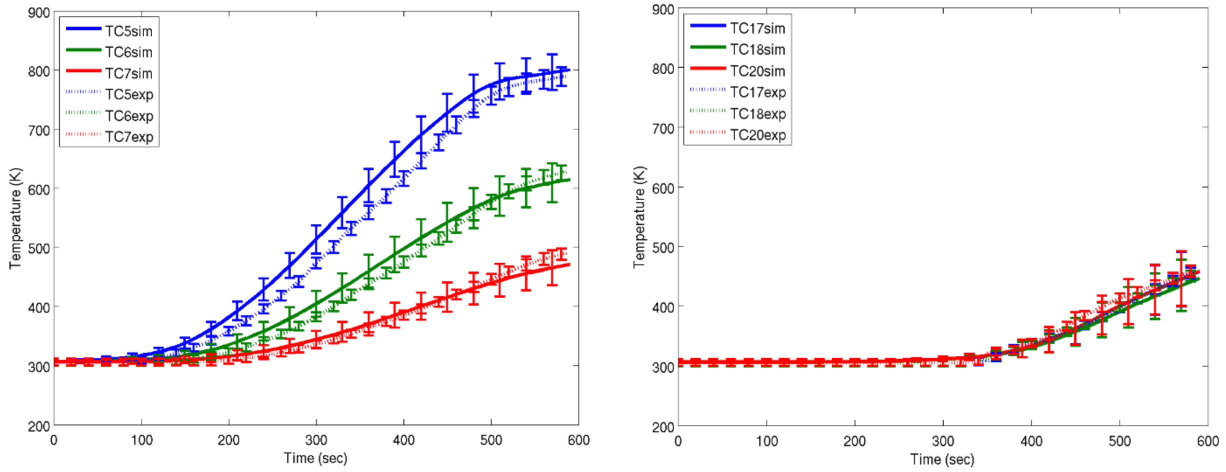

(a) (b)

Figure 34. Upright Orientation. Computational results (solid) with $\pm^{2\sigma_R}$ uncertainty and experimental results (dashed) with ±2% error for temperature vs time in the (a) exterior side thermocouples temperature and (b) the embedded object.

For the pressure, Figure 35 and Figure 36, the early pressure over prediction is evident in both the upright and inverted orientations. However, since these experiments were vented at a higher pressure, the model begins to under predict the inverted experiment and rate of pressure changes increases.

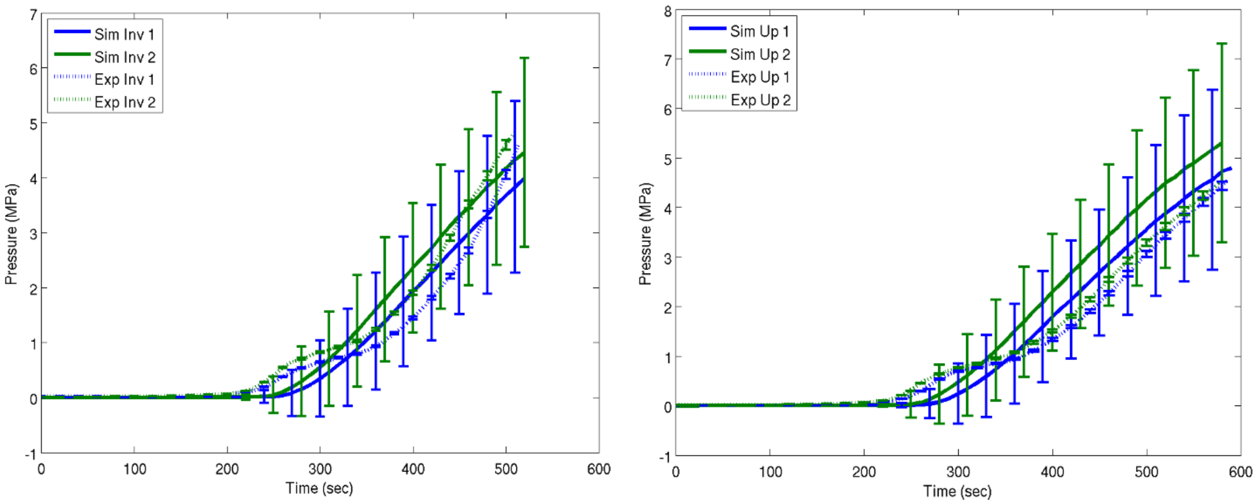

(a) (b)

Figure 35. Computational results (solid) with ±$^{2\sigma_R}$ uncertainty and experimental results (dashed) with ±2% error for pressure vs time for the (a) inverted and (b) upright orientations.

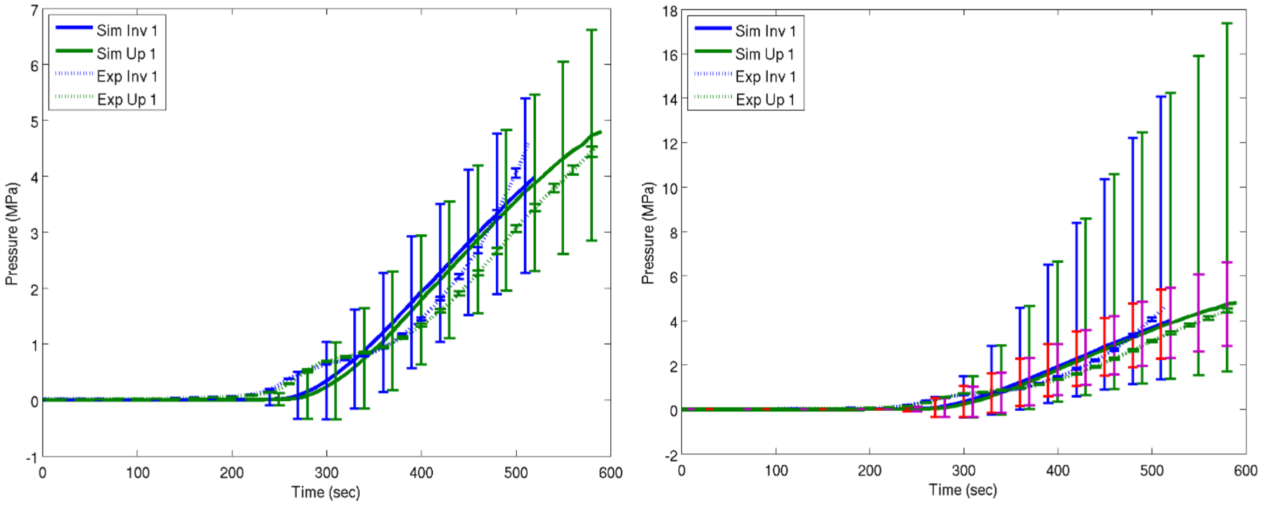

(a) (b)

Figure 36. (a) comparison between representative upright and inverted computational results (solid) with ±$^{2\sigma_R}$ uncertainty and experimental results (dashed) with ±2% error for pressure vs time and (b) comparison between representative upright and inverted computational results (solid) with ±$^{2\sigma_R}$ uncertainty with pressure multiplier included and experimental results (dashed) with ±2% error for pressure vs time with original uncertainties (from (a)) overlaid in red (upright) and purple (inverted)

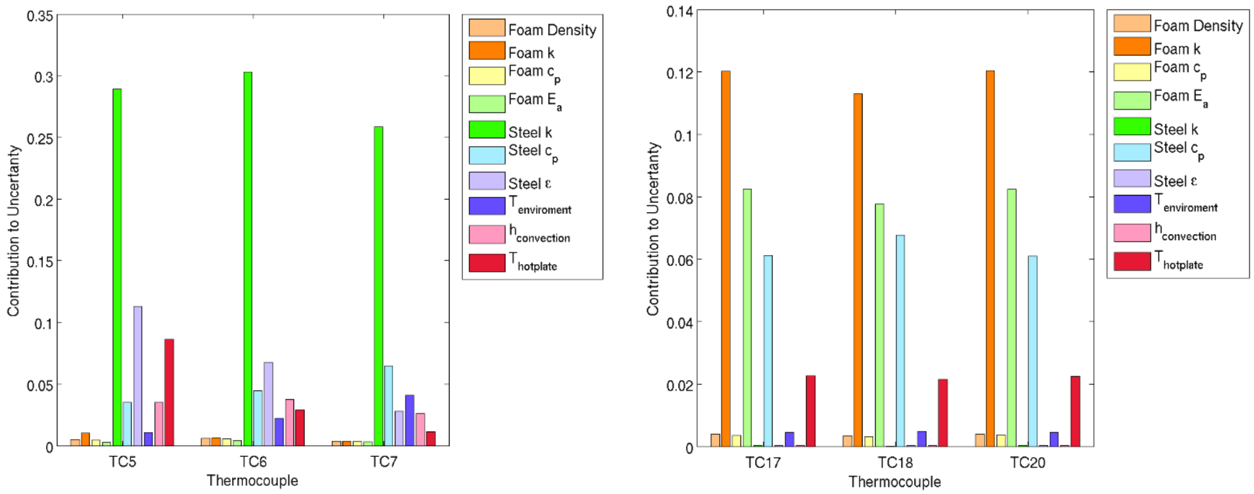

(a) (b)

Figure 37. Contribution to uncertainty for thermocouples (a) along the exterior side (b) on the embedded object for the inverted configuration.

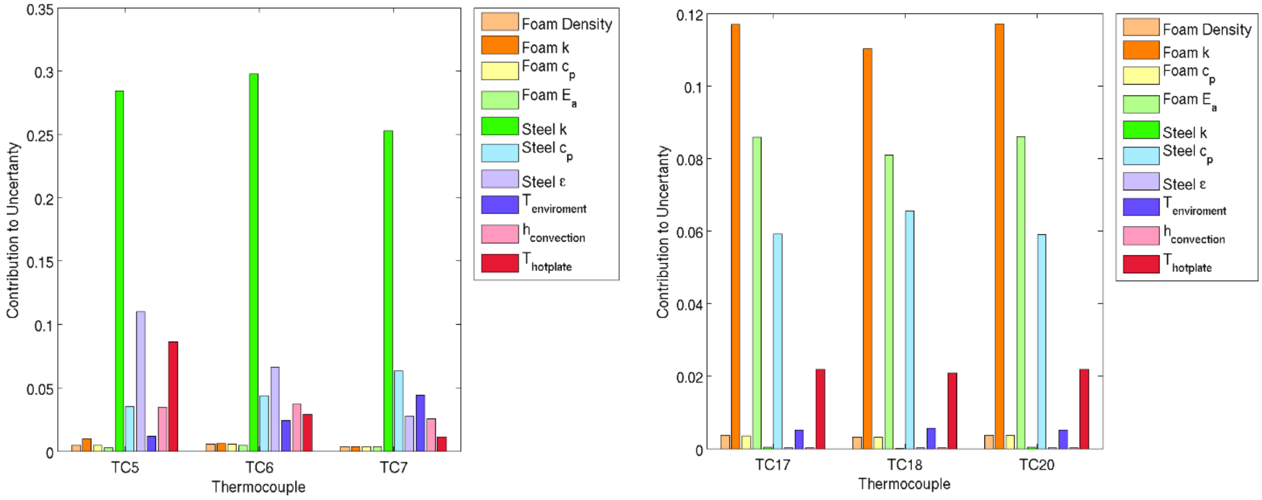

(a) (b)

Figure 38. Contribution to uncertainty for thermocouples (a) along the exterior side (b) on the embedded object for the upright configuration.

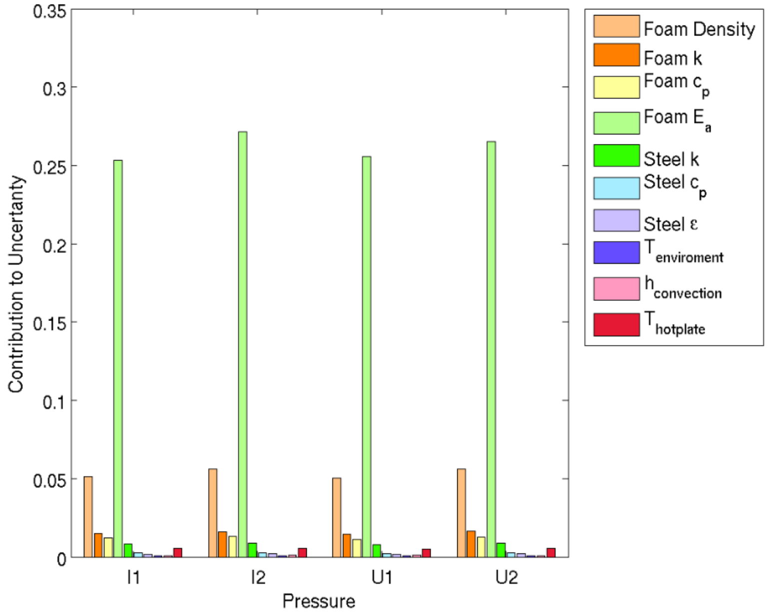

Figure 39. Contribution to uncertainty for pressure

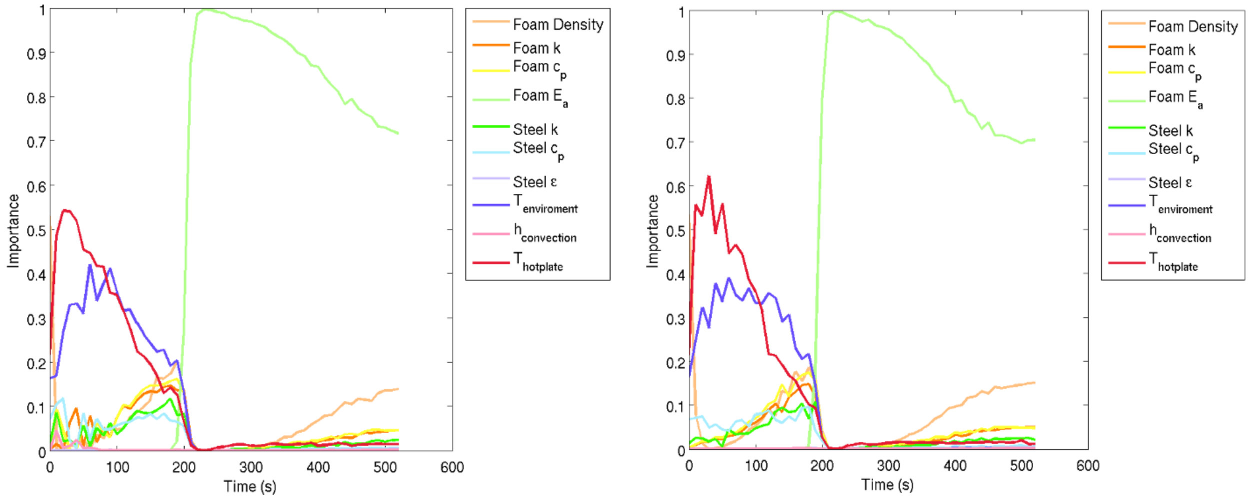

(a)

(b)

Figure 40. Parameter importance vs time for pressure for (a) inverted and (b) upright.

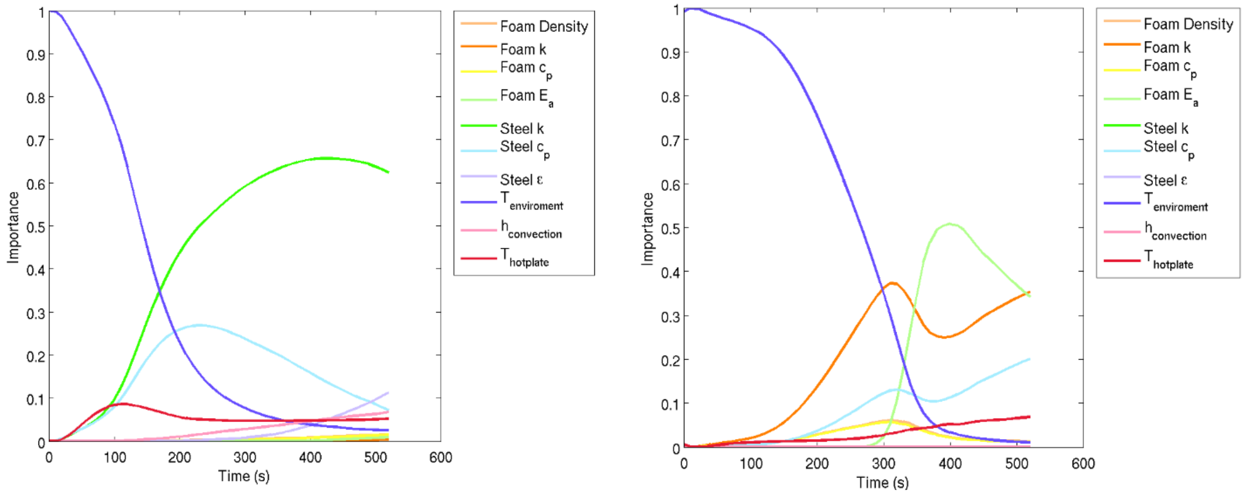

(a) (b)

Figure 41. Parameter importance vs time for (a) TC 6 and (b) TC 25 for the inverted configuration.

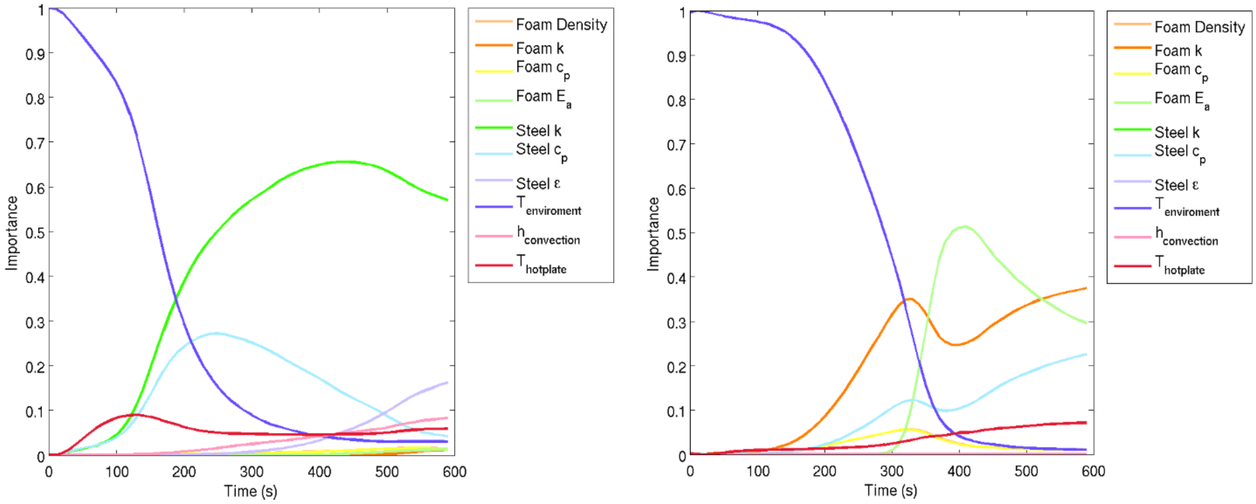

(a) (b)

Figure 42. Parameter importance vs time for (a) TC 6 and (b) TC 25 for the inverted configuration.

5.1.3 2011-30lb

For the 30lb dataset, Figure 43 shows that the inverted orientation under predicted the temperature response for both the sides and the embedded object. Figure 44 shows the upright orientation, which over predicts both the sides and then embedded object temperature.

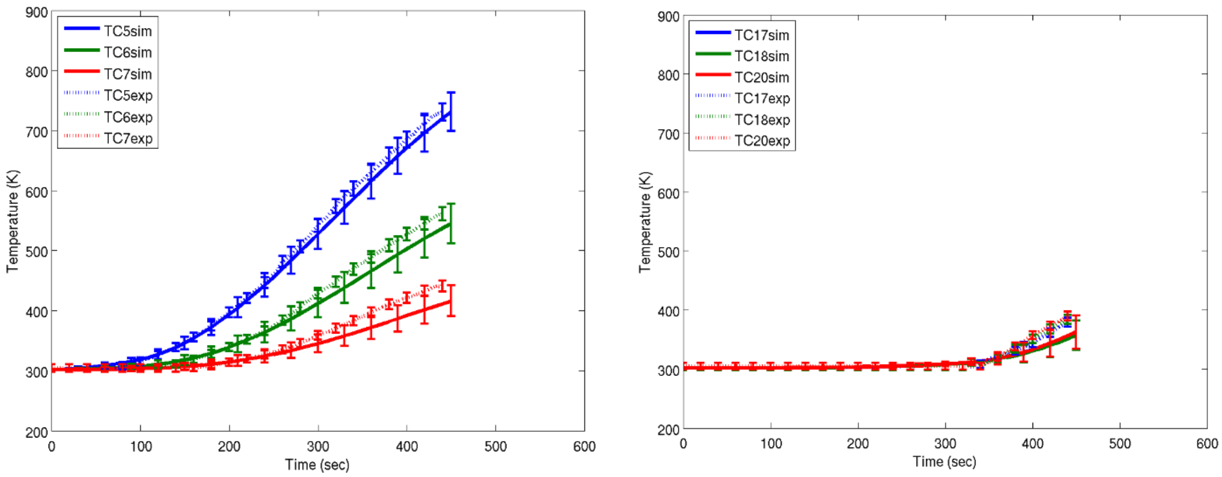

(a) (b)

Figure 43. Inverted Orientation. Computational results (solid) with ±$^{2\sigma_R}$ uncertainty and experimental results (dashed) with ±2% error for temperature vs time in the (a) exterior side thermocouples temperature and (b) the embedded object.

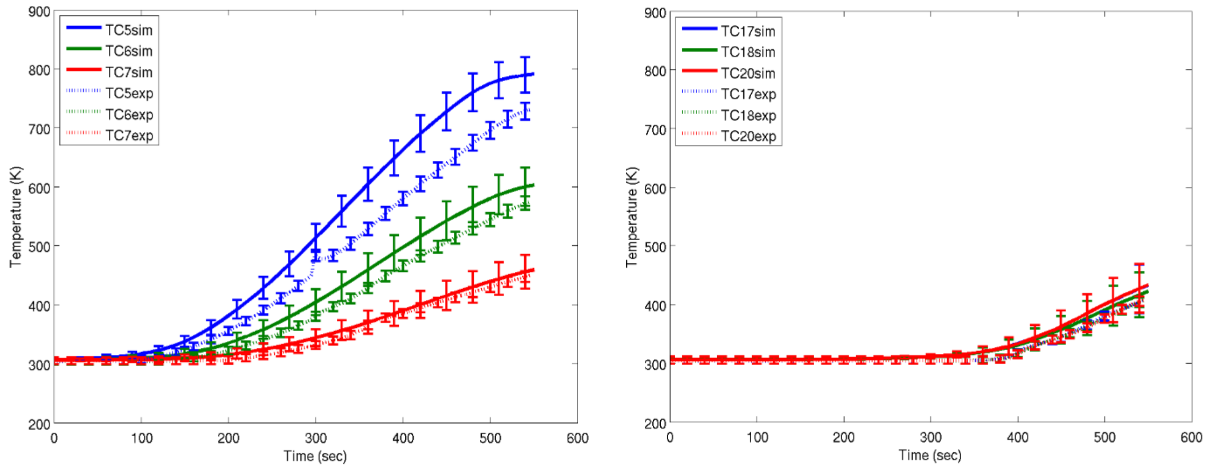

(a) (b)

Figure 44. Upright Orientation. Computational results (solid) with ±$^{2\sigma_R}$ uncertainty and experimental results (dashed) with ±2% error for temperature vs time in the (a) exterior side thermocouples temperature and (b) the embedded object.

Figure 45 and Figure 46 show the pressure response for the 30lb foam. While it is clear the pressure response is not capturing the nuanced physics of the problem (the slope changes are not captured), it does generally agree well with the upright configuration. However, the inverted orientation is consistently under predicted.

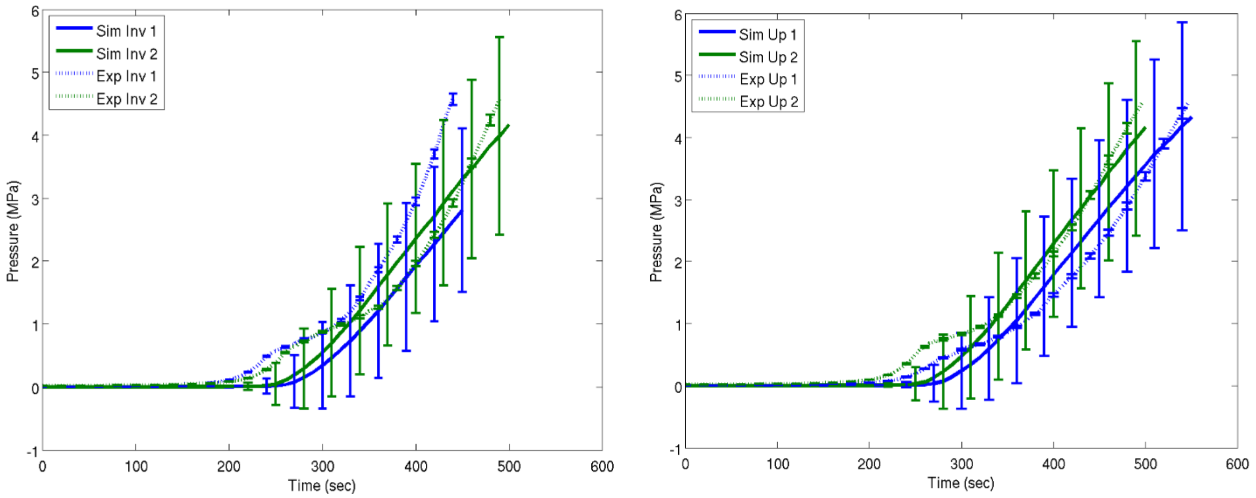

(a) (b)

Figure 45. Computational results (solid) with $\pm 2\sigma_R$ uncertainty and experimental results (dashed) with ±2% error for pressure vs time for the (a) inverted and (b) upright orientations.

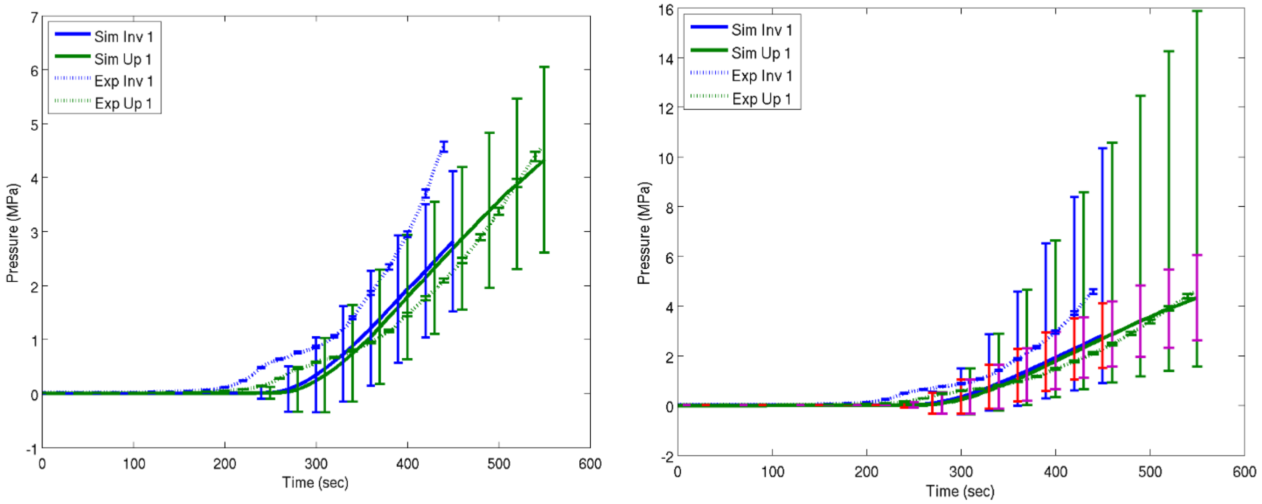

(a) (b)

Figure 46. (a) comparison between representative upright and inverted computational results (solid) with $\pm 2\sigma_R$ uncertainty and experimental results (dashed) with ±2% error for pressure vs time and (b) comparison between representative upright and inverted computational results (solid) with $\pm 2\sigma_R$ uncertainty with pressure multiplier included and experimental results (dashed) with ±2% error for pressure vs time with original uncertainties (from (a)) overlaid in red (upright) and purple (inverted)

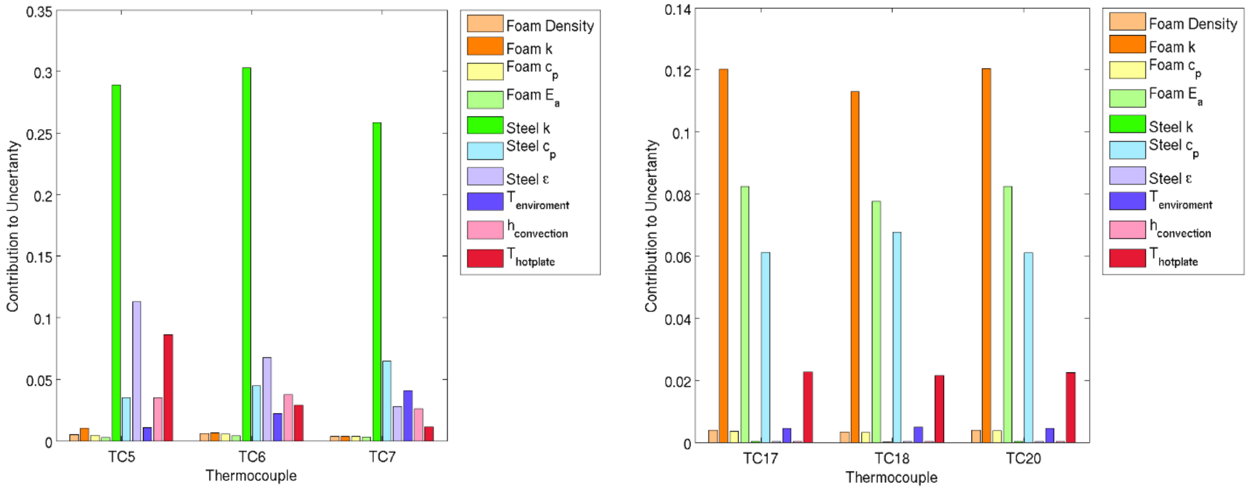

(a) (b)

Figure 47. Contribution to uncertainty for thermocouples (a) along the exterior side (b) on the embedded object for the inverted configuration.

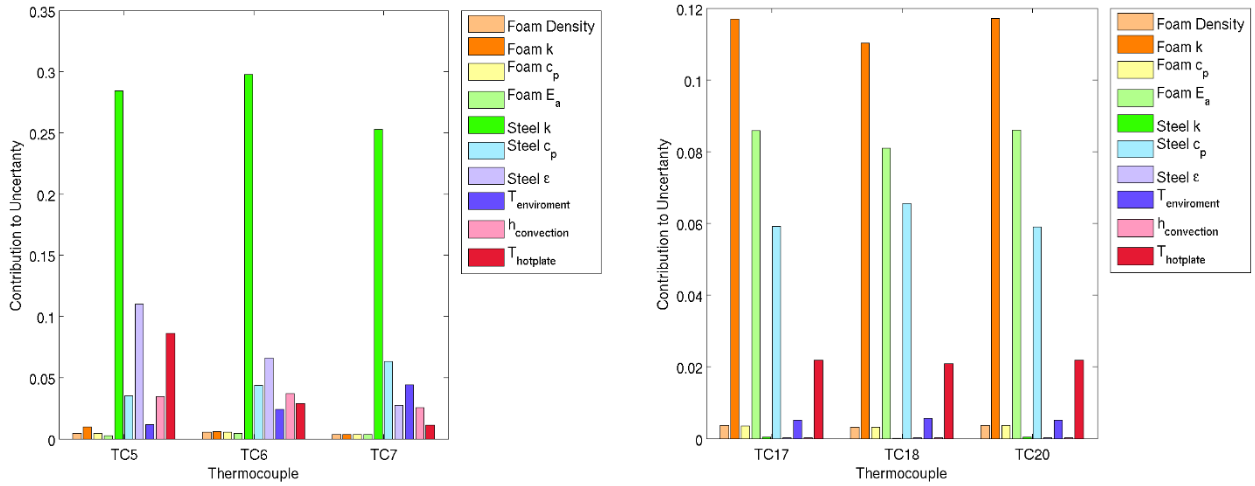

(a) (b)

Figure 48. Contribution to uncertainty for thermocouples (a) along the exterior side (b) on the embedded object for the upright configuration.

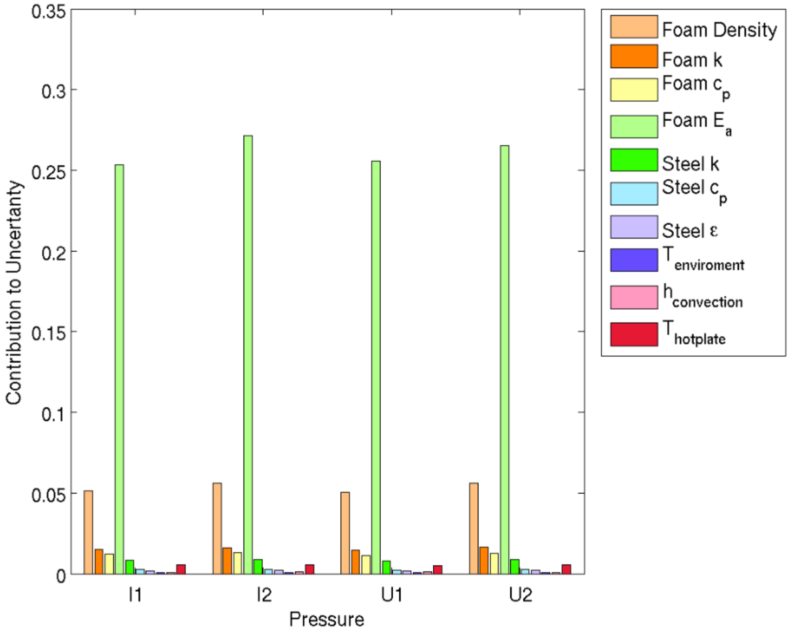

Figure 49. Contribution to uncertainty for pressure

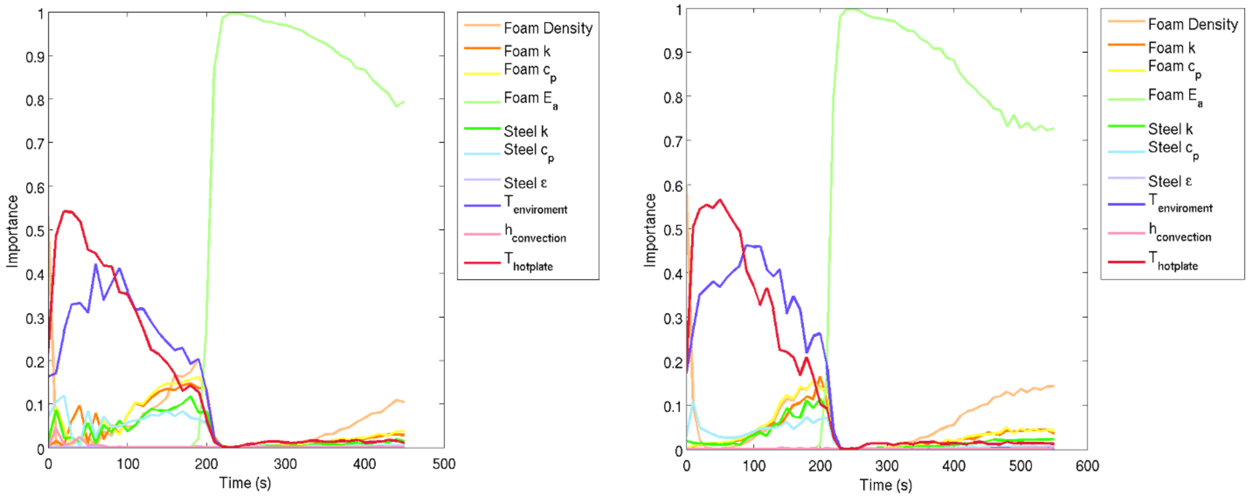

(a) (b)

Figure 50. Parameter importance vs time for pressure for (a) inverted and (b) upright.

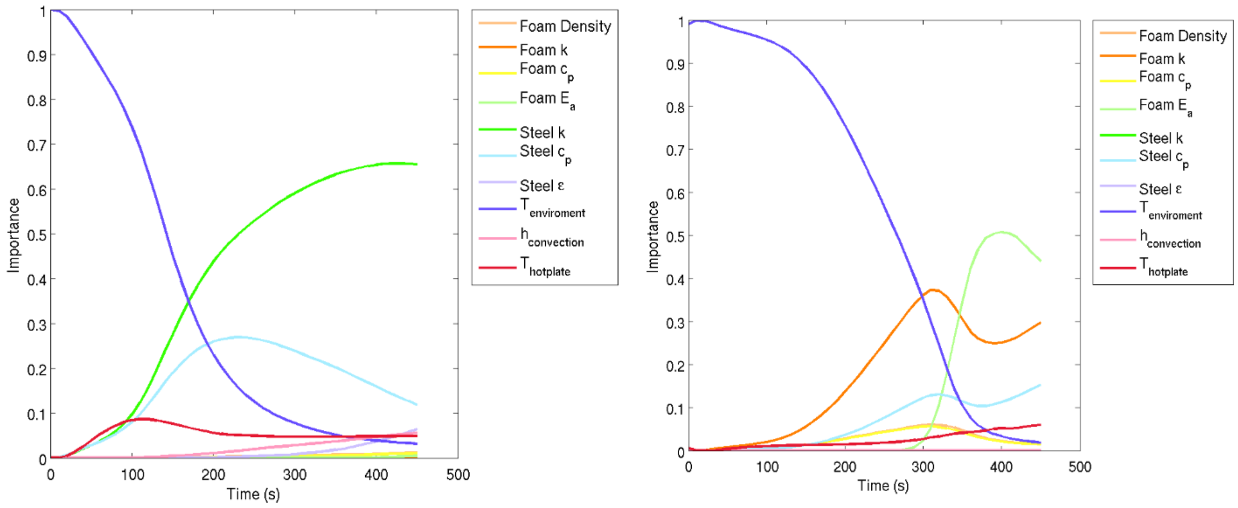

(a) (b)

Figure 51. Parameter importance vs time for (a) TC 6 and (b) TC 25 for the inverted configuration.

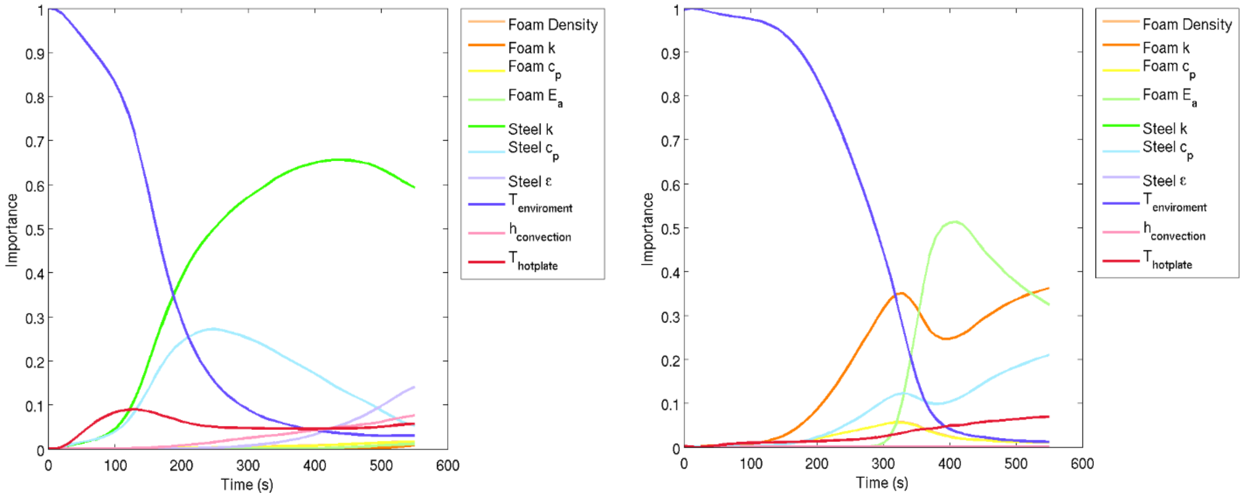

(a) (b)

Figure 52. Parameter importance vs time for (a) TC 6 and (b) TC 25 for the upright configuration.

5.1.4 2012

Figure 53 and Figure 54 show the same general trends that have been discussed in the previous datasets. However, since the experiments in this data set were ran until the can breached, it is possible to capture later in time behavior.

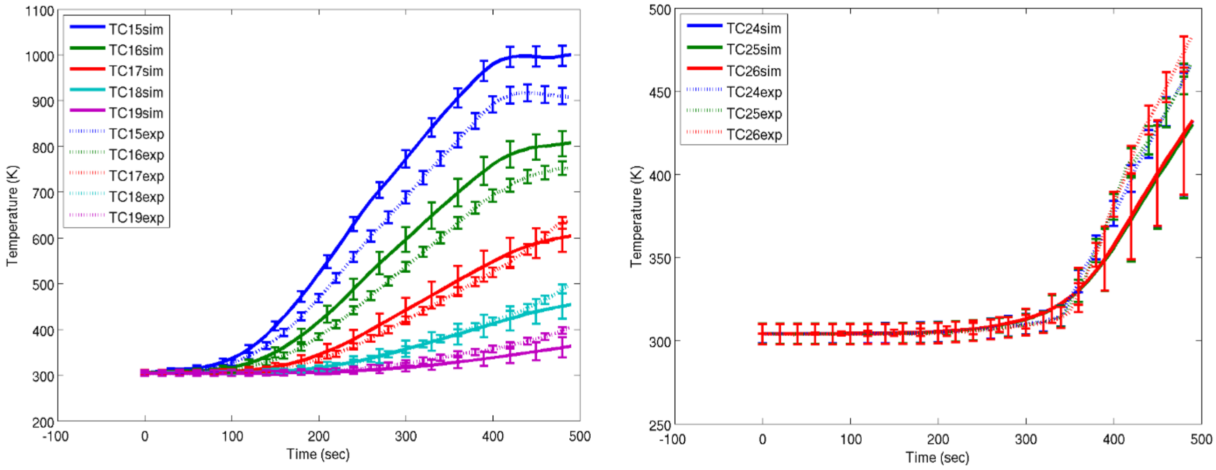

(a) (b)

Figure 53. Inverted Orientation. Computational results (solid) with ±$^{2\sigma_R}$ uncertainty and experimental results (dashed) with ±2% error for temperature vs time in the (a) exterior side thermocouples temperature and (b) the embedded object.

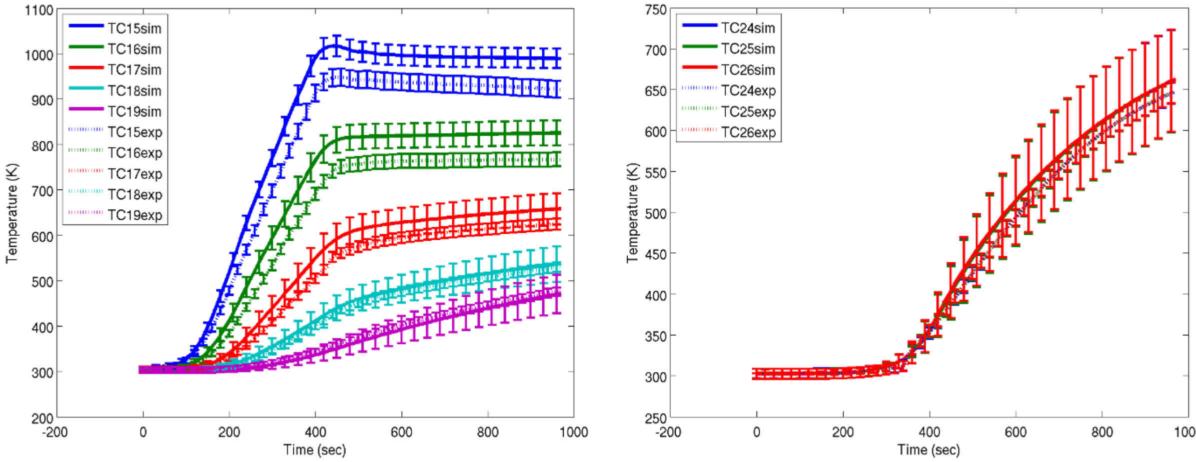

(a) (b)

Figure 54. Upright Orientation. Computational results (solid) with ±$^{2\sigma_R}$ uncertainty and experimental results (dashed) with ±2% error for temperature vs time in the (a) exterior side thermocouples temperature and (b) the embedded object.

Figure 55 and Figure 56 show the magnitude of the over prediction of the upright orientation and the under prediction of the inverted case only increase when the duration of the experiment is increased.

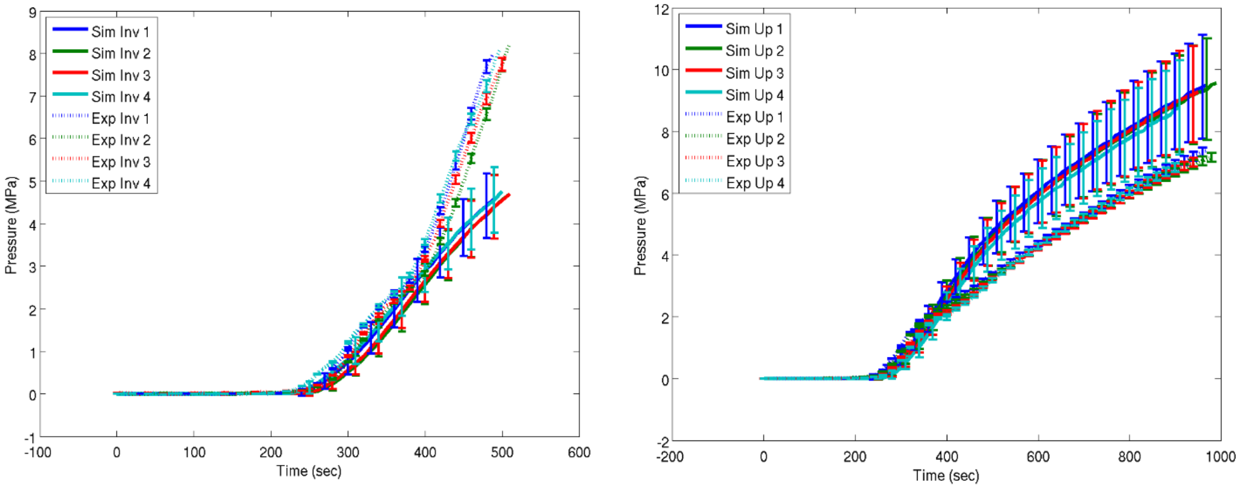

(a) (b)

Figure 55. Computational results (solid) with ±$2\sigma_R$ uncertainty and experimental results (dashed) with ±2% error for pressure vs time for the (a) inverted and (b) upright orientations.

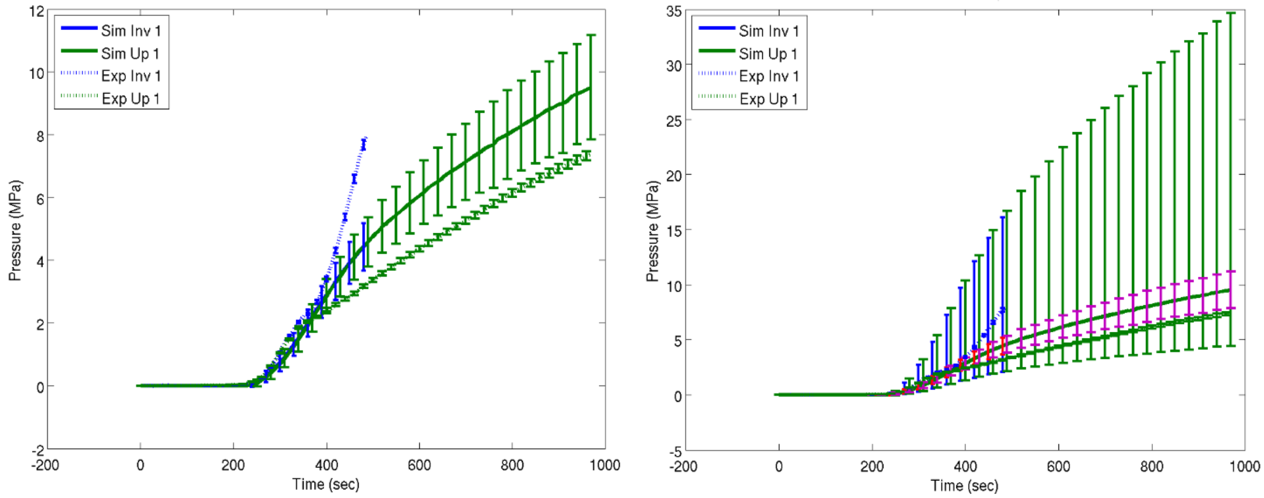

(a) (b)

Figure 56. (a) comparison between representative upright and inverted computational results (solid) with ±$2\sigma_R$ uncertainty and experimental results (dashed) with ±2% error for pressure vs time and (b) comparison between representative upright and inverted computational results (solid) with ±$2\sigma_R$ uncertainty with pressure multiplier included and experimental results (dashed) with ±2% error for pressure vs time with original uncertainties (from (a)) overlaid in red (upright) and purple (inverted)

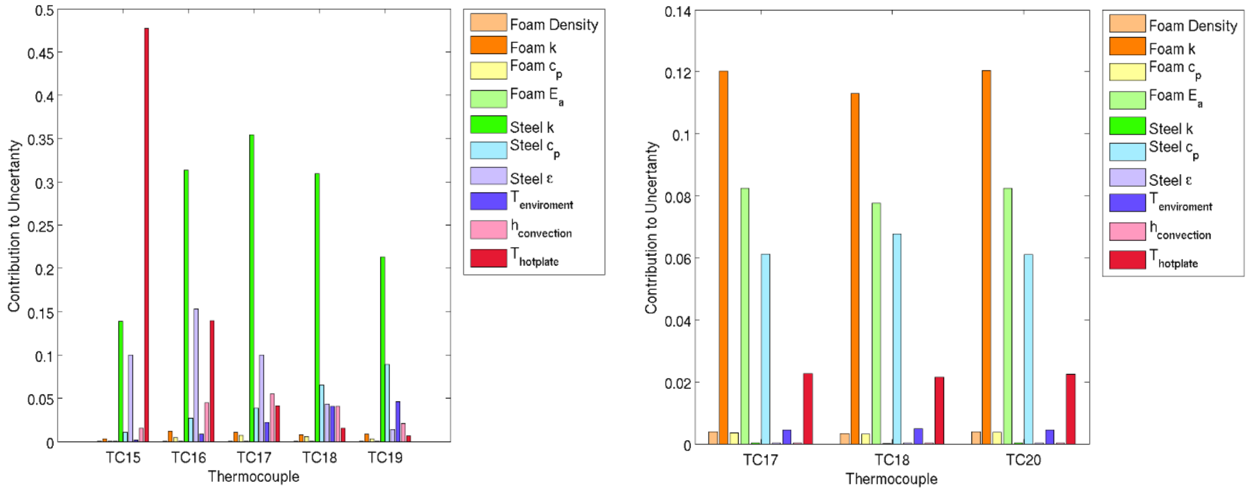

(a) (b)

Figure 57. Contribution to uncertainty for thermocouples (a) along the exterior side (b) on the embedded object for the inverted configuration.

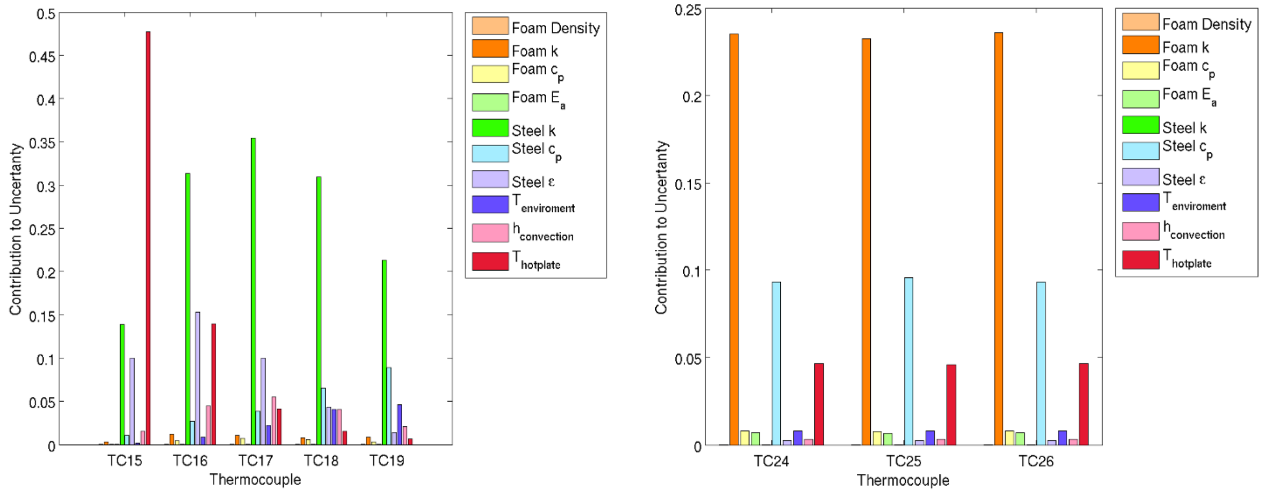

(a) (b)

Figure 58. Contribution to uncertainty for thermocouples (a) along the exterior side (b) on the embedded object for the upright configuration.

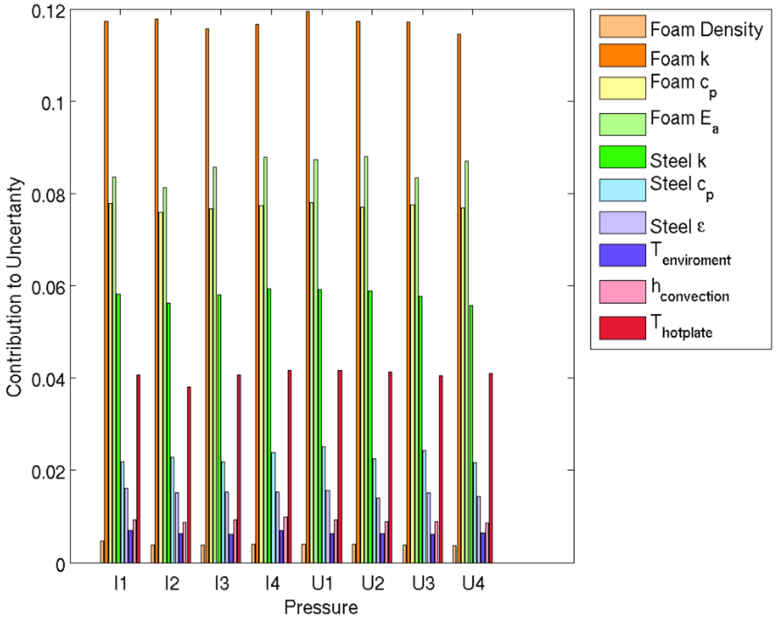

Figure 59. Contribution to uncertainty for pressure

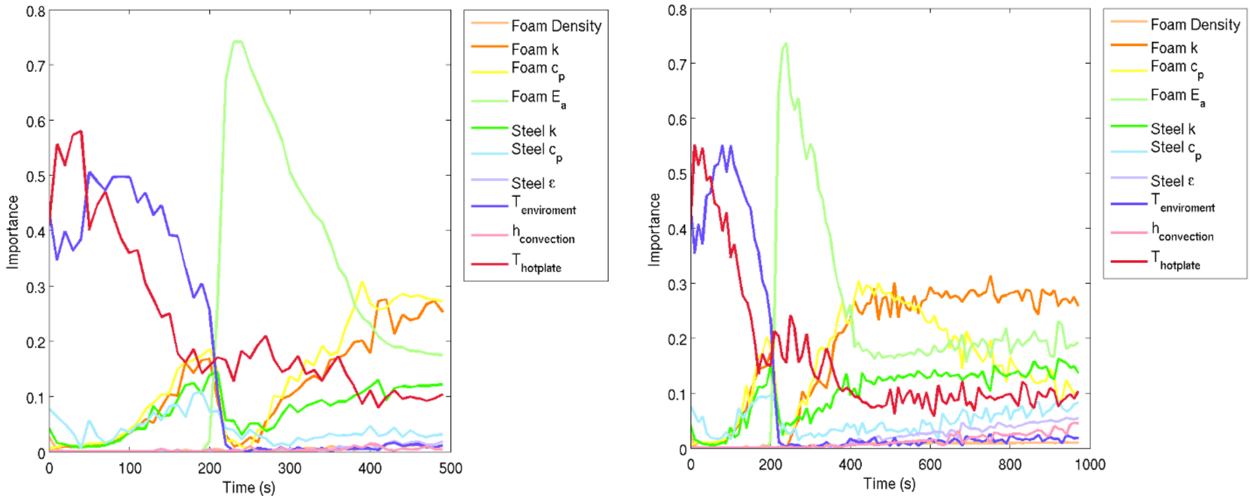

(a) (b)

Figure 60. Parameter importance vs time for pressure for (a) inverted and (b) upright.

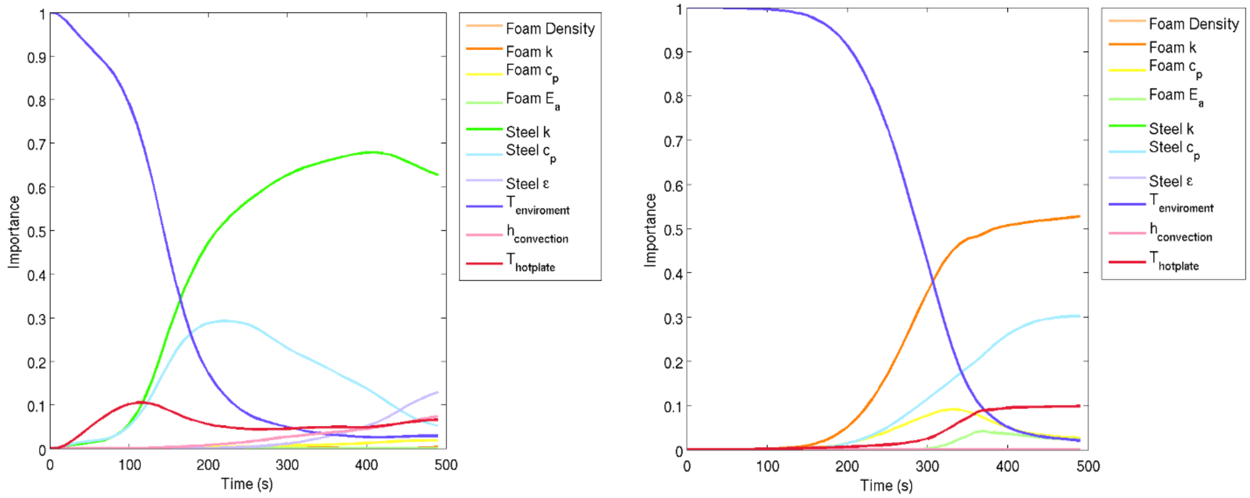

(a) (b)

Figure 61. Parameter importance vs time for (a) TC 17 and (b) TC 25 for the inverted configuration.

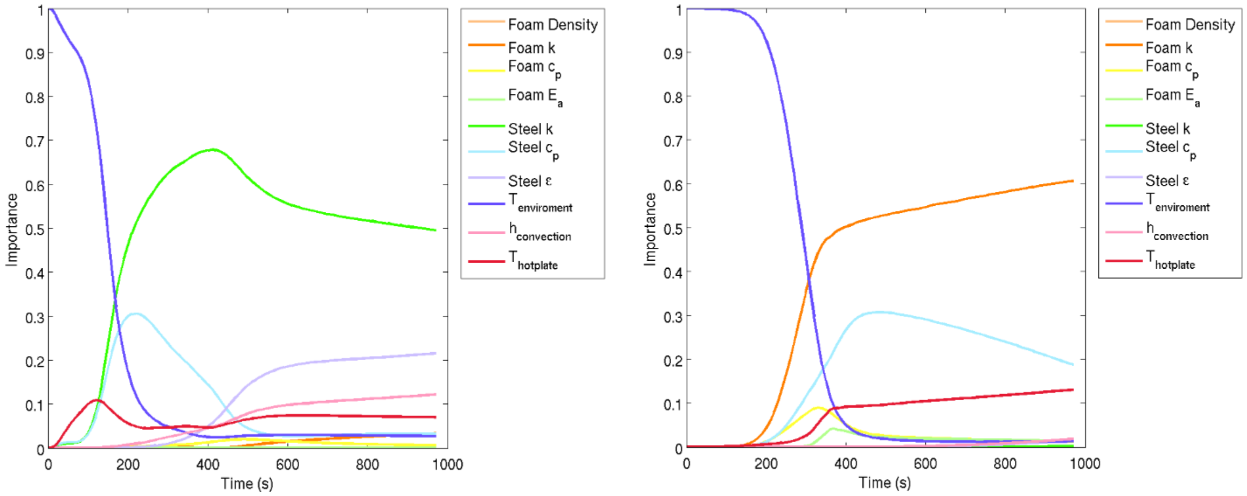

(a) (b)

Figure 62. Parameter importance vs time for (a) TC 17 and (b) TC 25 for the upright configuration.

5.1.5 2013-10C

The 2013-10C experiments were also run to breach and at a much lower heating rate. This means the tests were approximately four times longer than the 2012 tests. This yields some interesting effects in the in the experimental data, specifically in the temperature of the embedded object, as seen in Figure 63(b) and Figure 64(b). These slope changes would indicate that unmodeled physics, such as radiation from the hot plate to the object after the object becomes exposed.

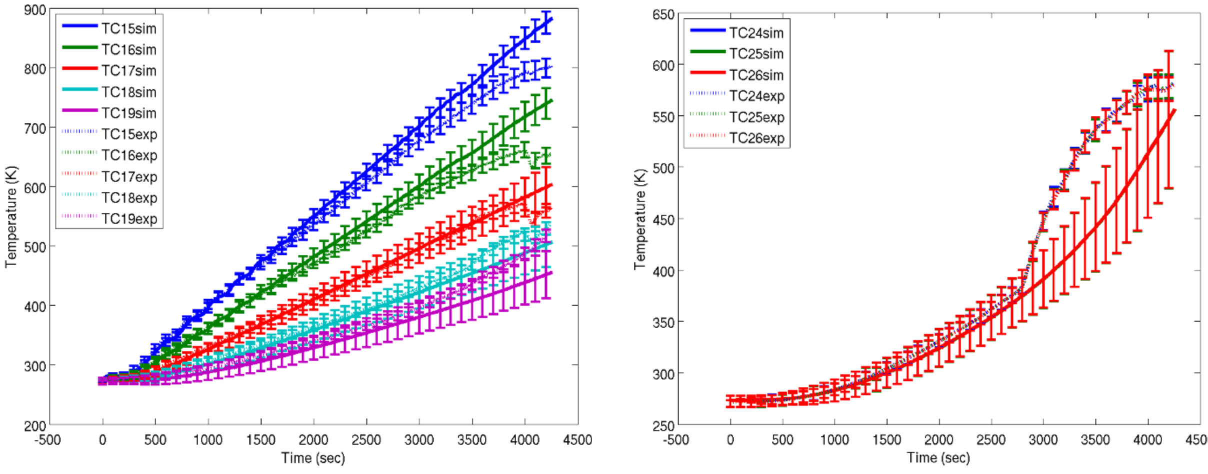

(a) (b)

Figure 63. Inverted Orientation. Computational results (solid) with $\pm^{2\sigma_R}$ uncertainty and experimental results (dashed) with ±2% error for temperature vs time in the (a) exterior side thermocouples temperature and (b) the embedded object.

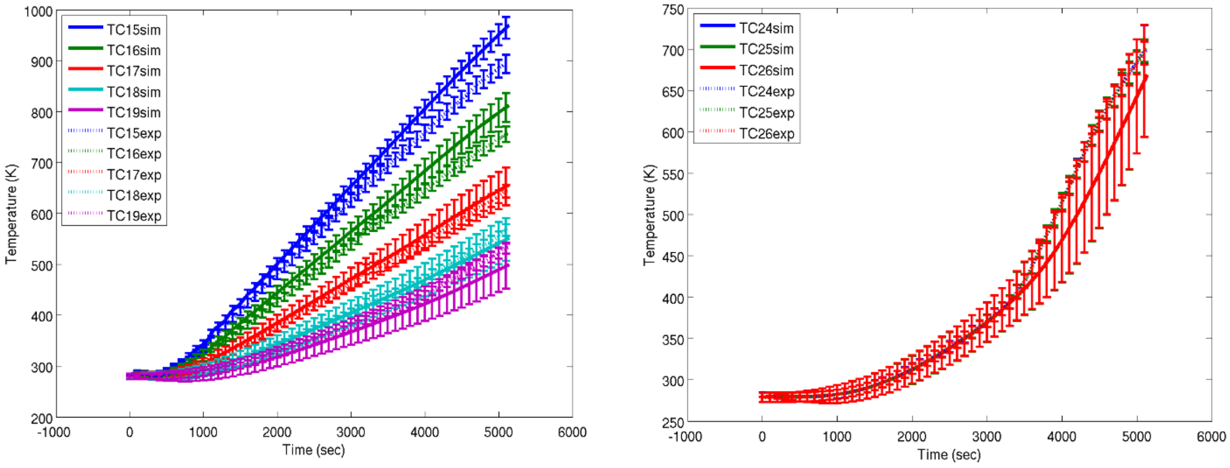

(a) (b)

Figure 64. Upright Orientation. Computational results (solid) with $\pm^{2\sigma_R}$ uncertainty and experimental results (dashed) with ±2% error for temperature vs time in the (a) exterior side thermocouples temperature and (b) the embedded object.

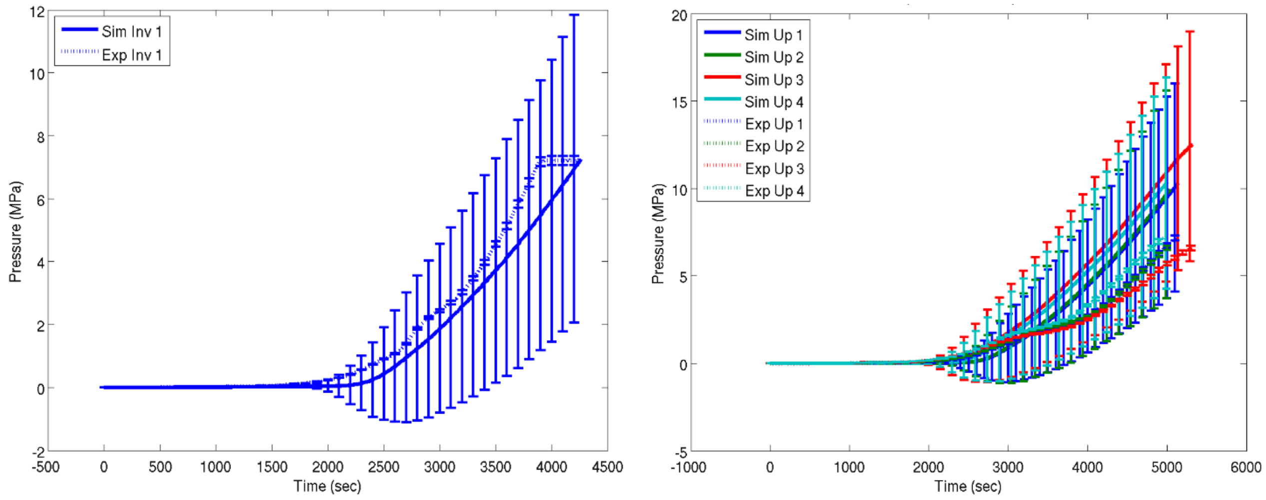

(a) (b)

Figure 65. Computational results (solid) with $\pm 2\sigma_R$ uncertainty and experimental results (dashed) with ±2% error for pressure vs time for the (a) inverted and (b) upright orientations.

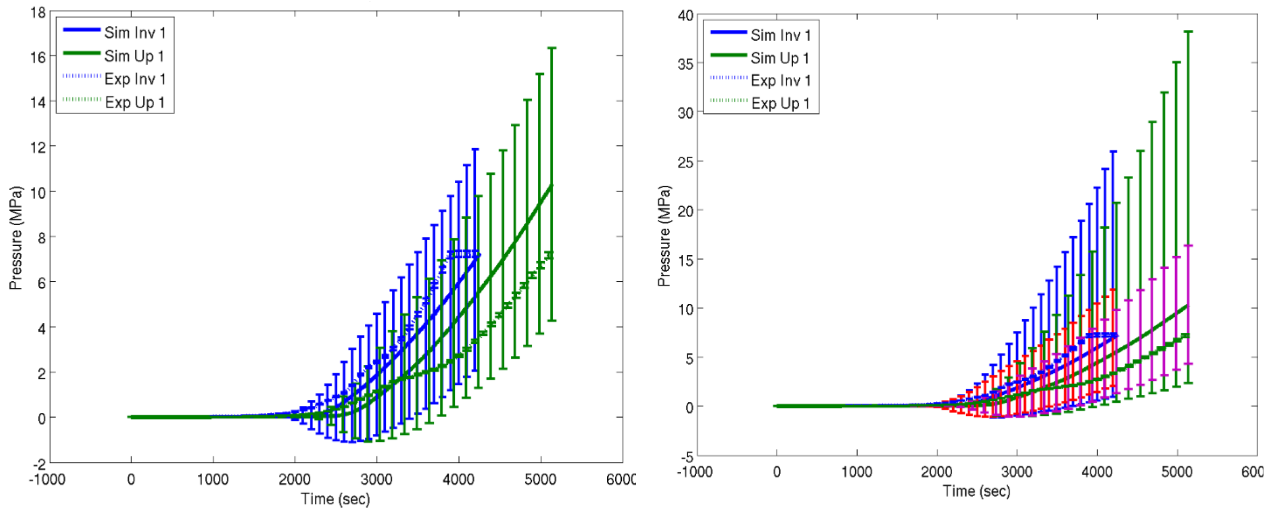

(a) (b)

Figure 66. (a) comparison between representative upright and inverted computational results (solid) with $\pm 2\sigma_R$ uncertainty and experimental results (dashed) with ±2% error for pressure vs time and (b) comparison between representative upright and inverted computational results (solid) with $\pm 2\sigma_R$ uncertainty with pressure multiplier included and experimental results (dashed) with ±2% error for pressure vs time with original uncertainties (from (a)) overlaid in red (upright) and purple (inverted)

Another interesting consequence of the lower heating rate is that, unlike in all previous datasets, the activation energy of the foam is now the most important contributor to the uncertainty parameter rather than the conductivity of the foam (Figure 67b, Figure 68b, Figure 71b, and Figure 72b). The slower heating rate means that a longer portion of the simulation takes place when foam properties have changed due to the reaction having occurred. Since the activation energy governs when the reaction will take place in the foam, and the reaction governs what the material properties of the foam are, this may explain the rise in the importance of the activation energy.

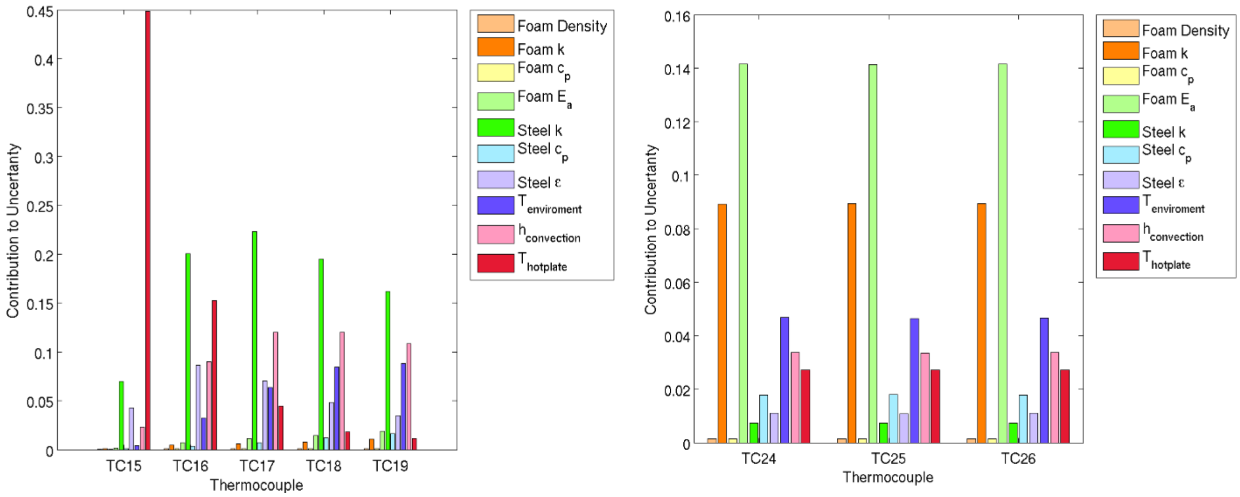

(a) (b)

Figure 67. Contribution to uncertainty for thermocouples (a) along the exterior side (b) on the embedded object for the inverted configuration.

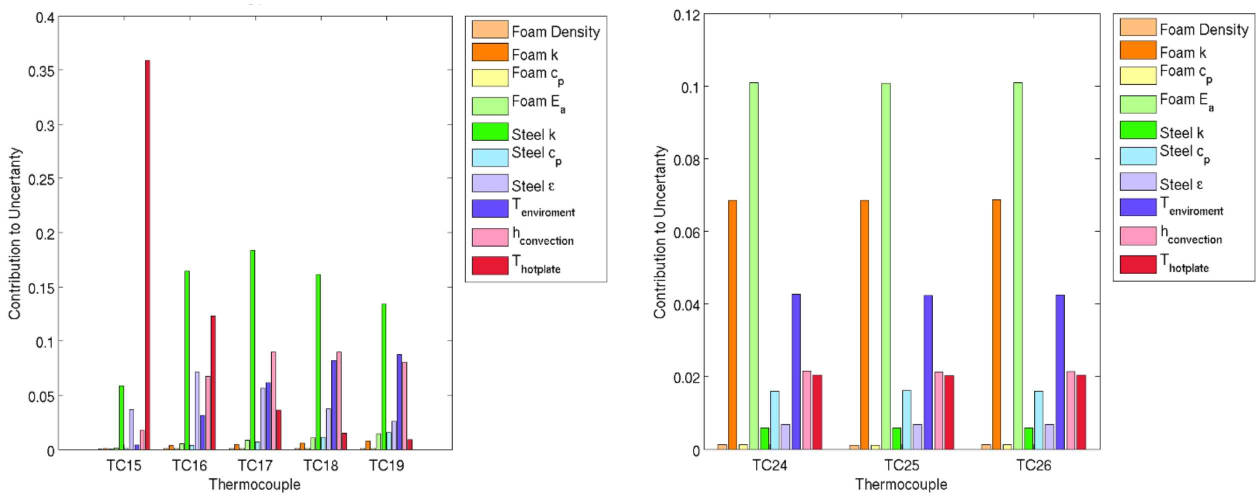

(a) (b)

Figure 68. Contribution to uncertainty for thermocouples (a) along the exterior side (b) on the embedded object for the upright configuration.

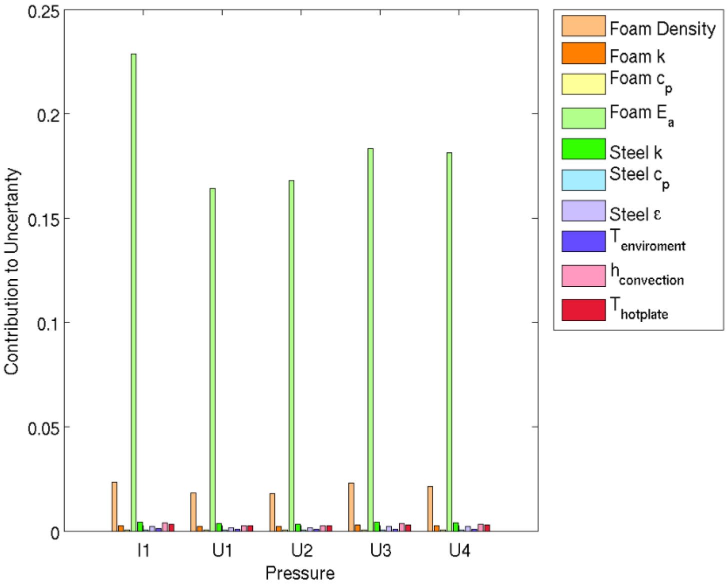

Figure 69. Contribution to uncertainty for pressure

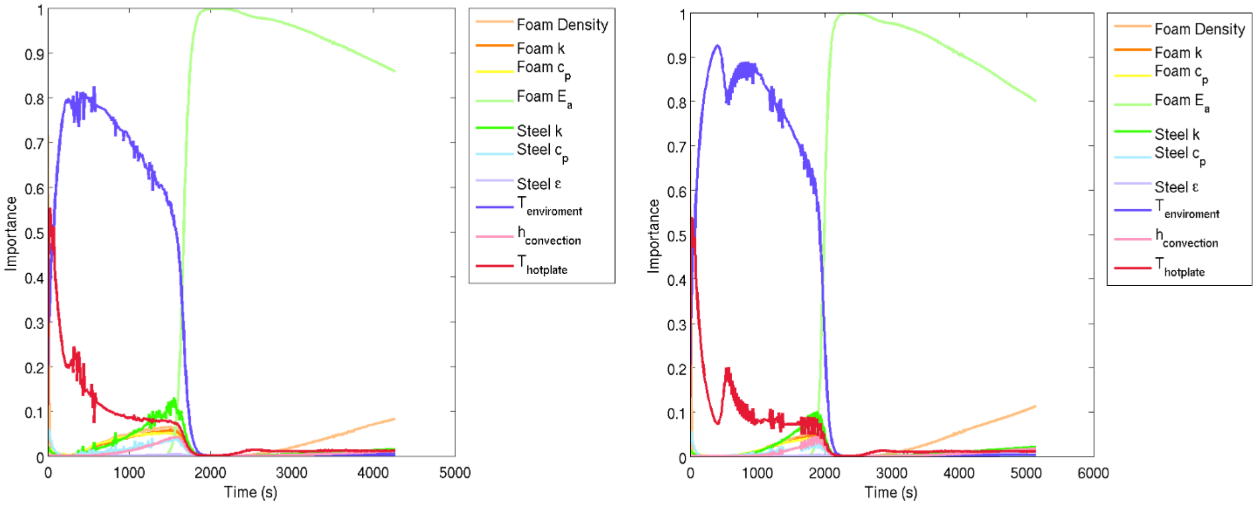

(a)

(b)

Figure 70. Parameter importance vs time for pressure for (a) inverted and (b) upright.

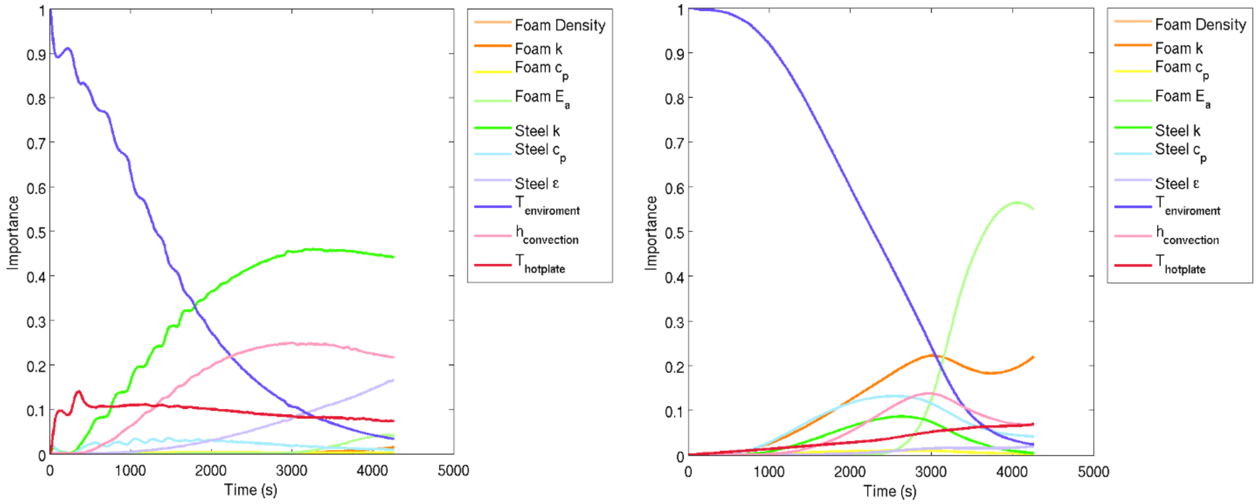

(a) (b)

Figure 71. Parameter importance vs time for (a) TC 17 and (b) TC 25 for the inverted configuration.

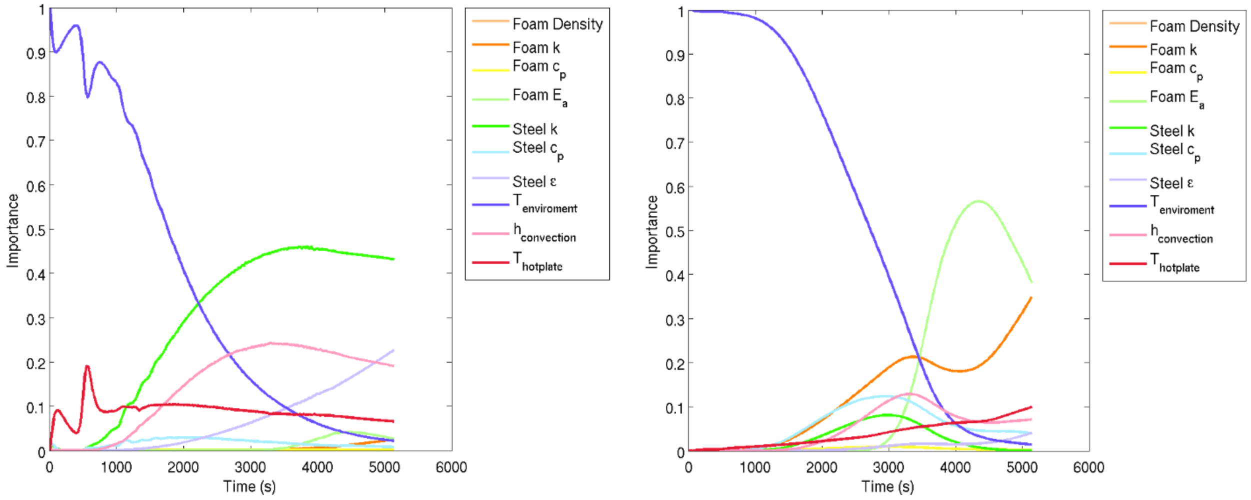

(a) (b)

Figure 72. Parameter importance vs time for (a) TC 17 and (b) TC 25 for the upright configuration.

5.1.6 2013-50C

This series of experiments was also ran at a lower heating rate and shows some of the additional interesting physics that were described in 5.1.5 in regards to the embedded object temperature (Figure 73b and Figure 74b).

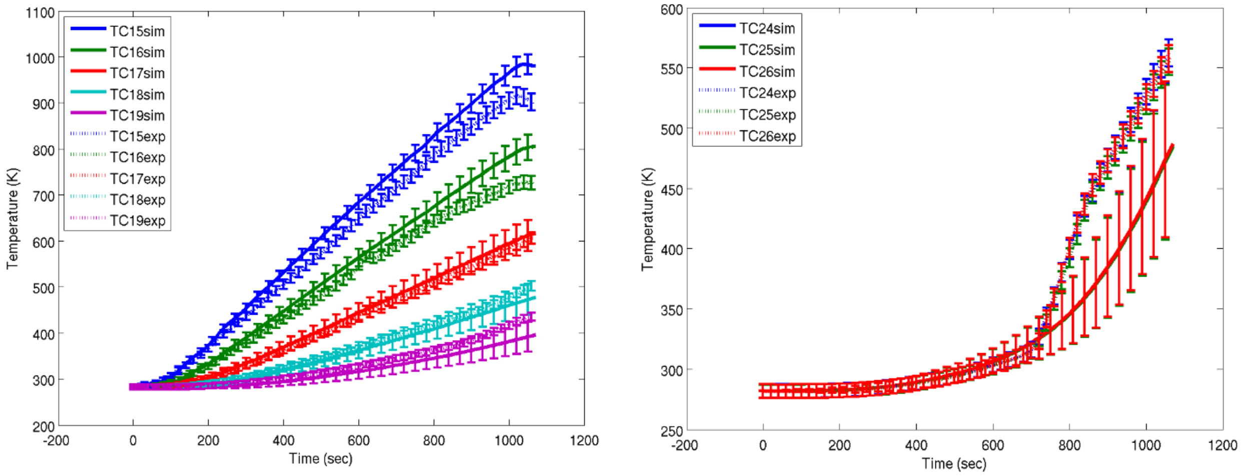

(a) (b)

Figure 73. Inverted Orientation. Computational results (solid) with ±$^{2\sigma_R}$ uncertainty and experimental results (dashed) with ±2% error for temperature vs time in the (a) exterior side thermocouples temperature and (b) the embedded object.

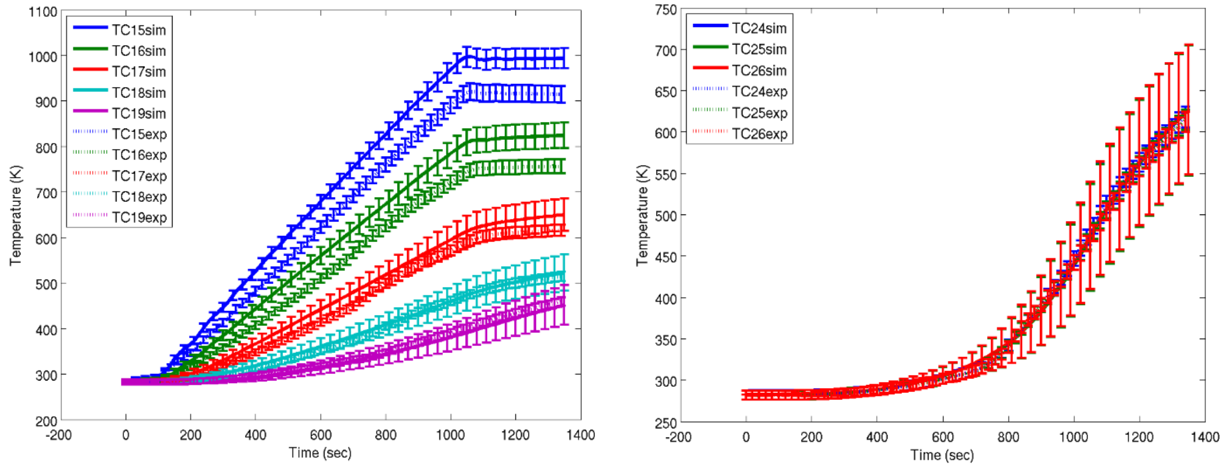

(a) (b)

Figure 74. Upright Orientation. Computational results (solid) with ±$^{2\sigma_R}$ uncertainty and experimental results (dashed) with ±2% error for temperature vs time in the (a) exterior side thermocouples temperature and (b) the embedded object.

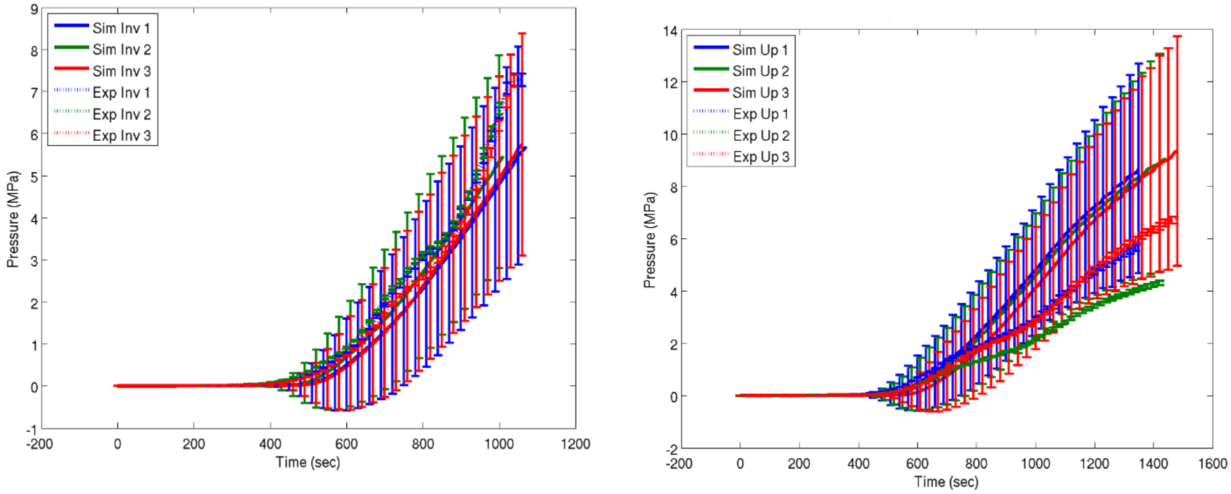

(a) (b)

Figure 75. Computational results (solid) with ±$^{2\sigma_R}$ uncertainty and experimental results (dashed) with ±2% error for pressure vs time for the (a) inverted and (b) upright orientations.

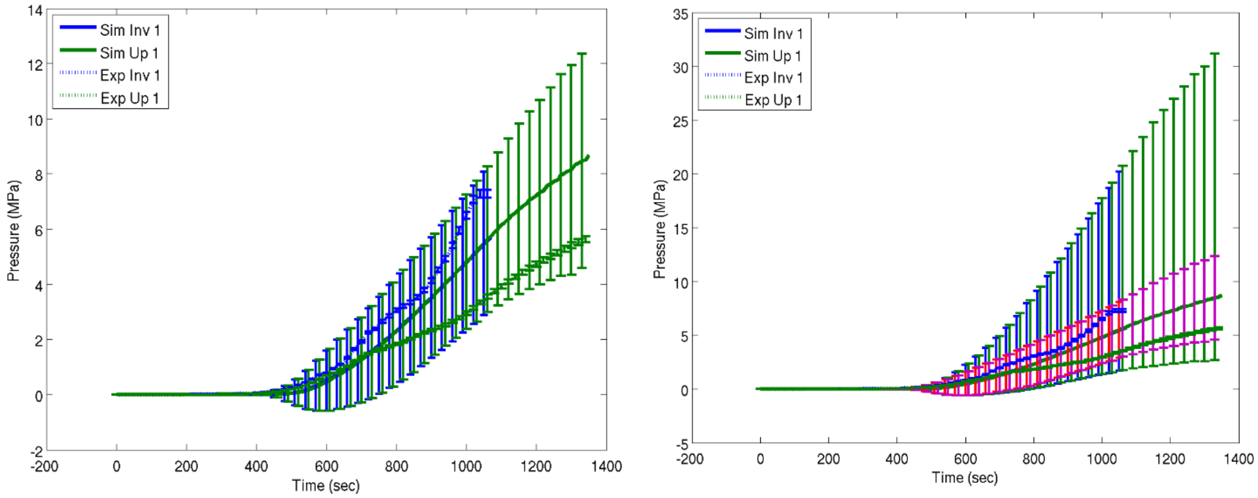

(a) (b)

Figure 76. (a) comparison between representative upright and inverted computational results (solid) with ±$^{2\sigma_R}$ uncertainty and experimental results (dashed) with ±2% error for pressure vs time and (b) comparison between representative upright and inverted computational results (solid) with ±$^{2\sigma_R}$ uncertainty with pressure multiplier included and experimental results (dashed) with ±2% error for pressure vs time with original uncertainties (from (a)) overlaid in red (upright) and purple (inverted)

As in 5.1.5, the lower heating rate drastically increases the importance of the activation energy of the foam, such that now it is almost equation to the foam conductivity (Figure 77b, Figure 78b, Figure 81b, and Figure 82b).

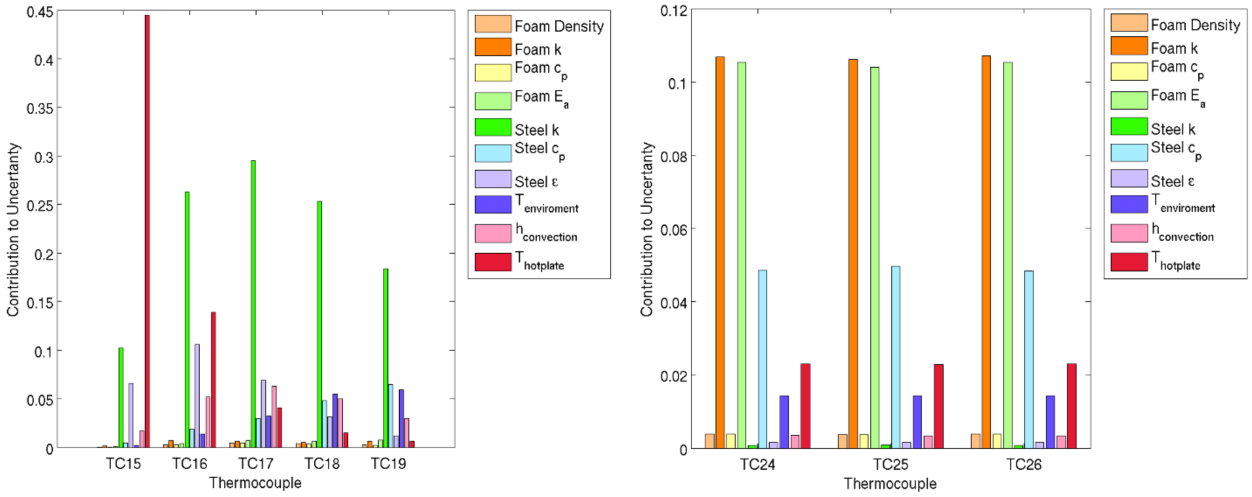

(a) (b)

Figure 77. Contribution to uncertainty for thermocouples (a) along the exterior side (b) on the embedded object for the inverted configuration.

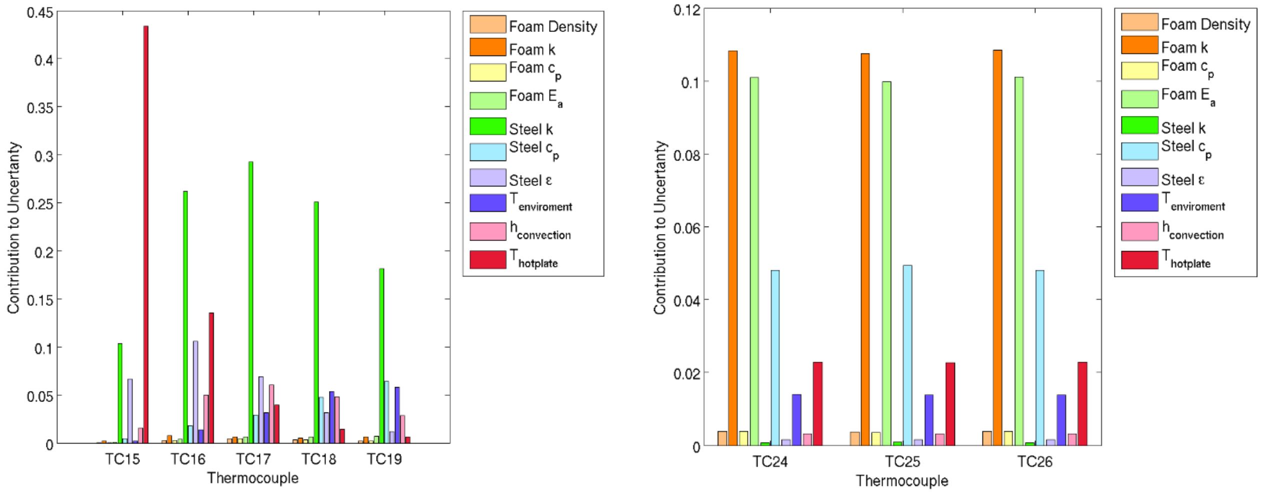

(a) (b)

Figure 78. Contribution to uncertainty for thermocouples (a) along the exterior side (b) on the embedded object for the upright configuration.

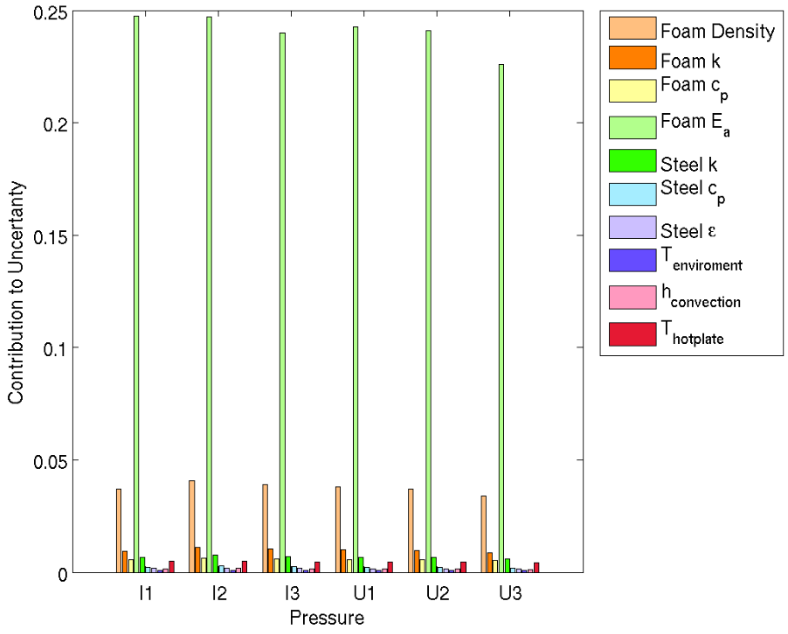

Figure 79. Contribution to uncertainty for pressure

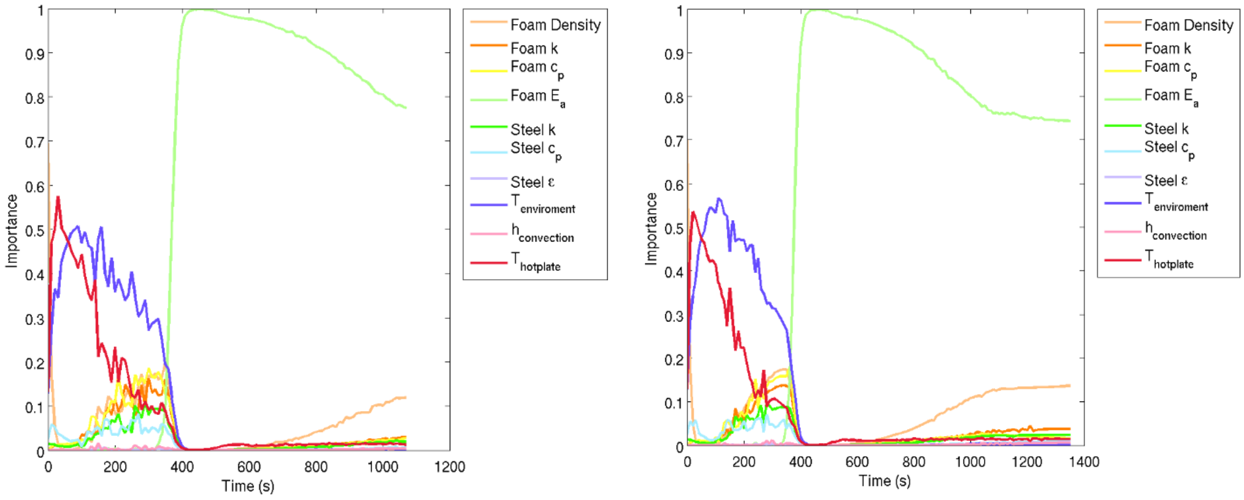

(a) (b)

Figure 80. Parameter importance vs time for pressure for (a) inverted and (b) upright.

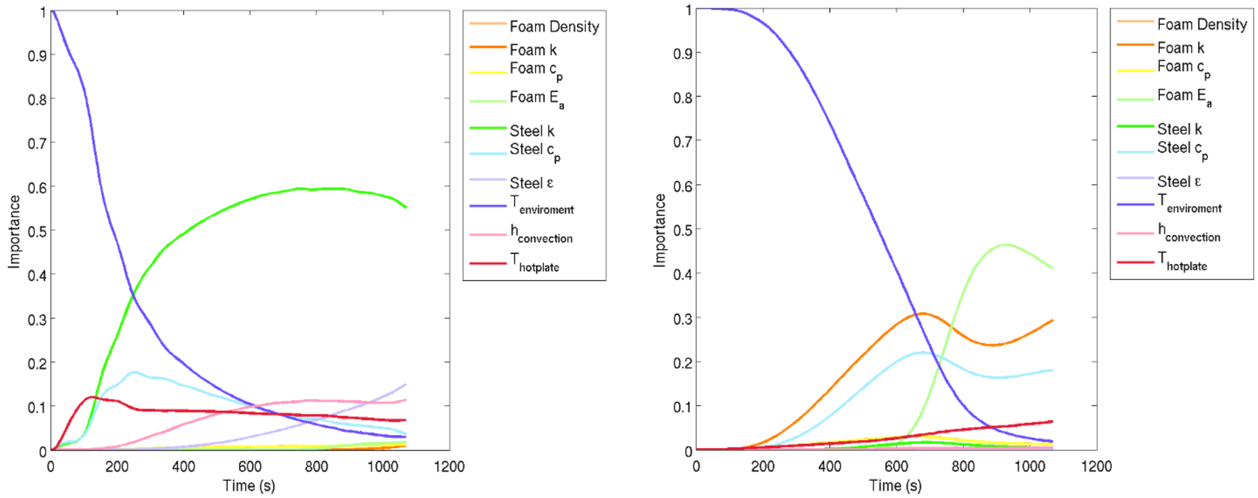

(a) (b)

Figure 81. Parameter importance vs time for (a) TC 17 and (b) TC 25 for the inverted configuration.

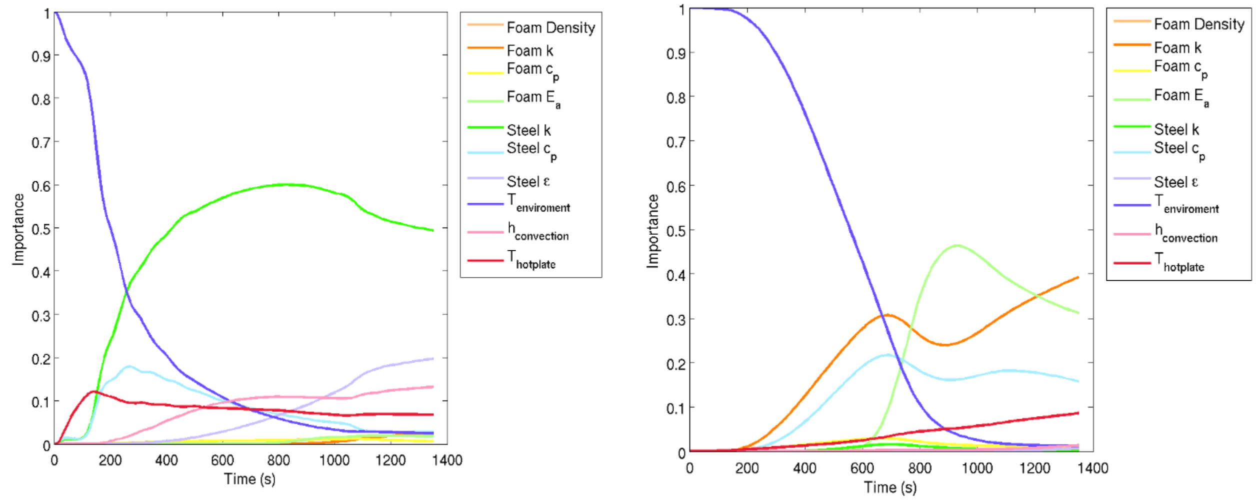

(a) (b)

Figure 82. Parameter importance vs time for (a) TC 17 and (b) TC 25 for the upright configuration.

5.2 LHS Approach

Figure 83 and Figure 84 compare the computational model results to the experimental results for select thermocouples and for pressure in the upright and inverted orientations. The mean of the responses with a $\pm 2\sigma_R$ propagated uncertainty for the computational results and ±2% error for the experimental results are included in Figure 83 and Figure 84 for both upright and inverted orientations. As was the case for the mean value results, Figure 83 and Figure 84a show generally good agreement between the computational and experimental results, especially for thermocouples farther from the heated surface. Figure 84b shows the pressure response of the model compared to the experiment, with a similar result as for the mean value approach. The mean and uncertainties of the mean value and LHS approach appear very similar and will be discussed further in the next section.

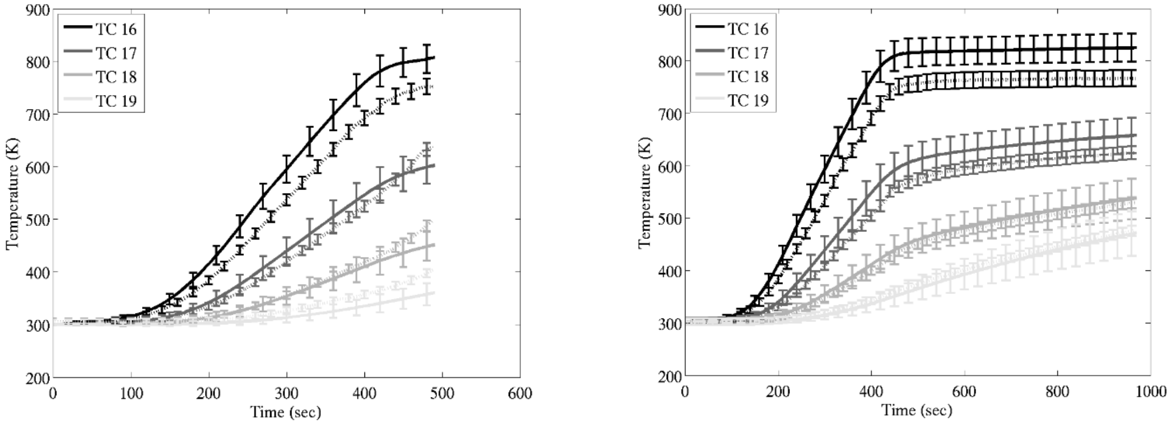

(a) (b)

Figure 83. Computational results (solid) with ±$2\sigma_R$ uncertainty and experimental results (dashed) with ±2% error for the exterior side thermocouples temperature vs time in the (a) inverted and (b) upright orientations using the LHS approach.

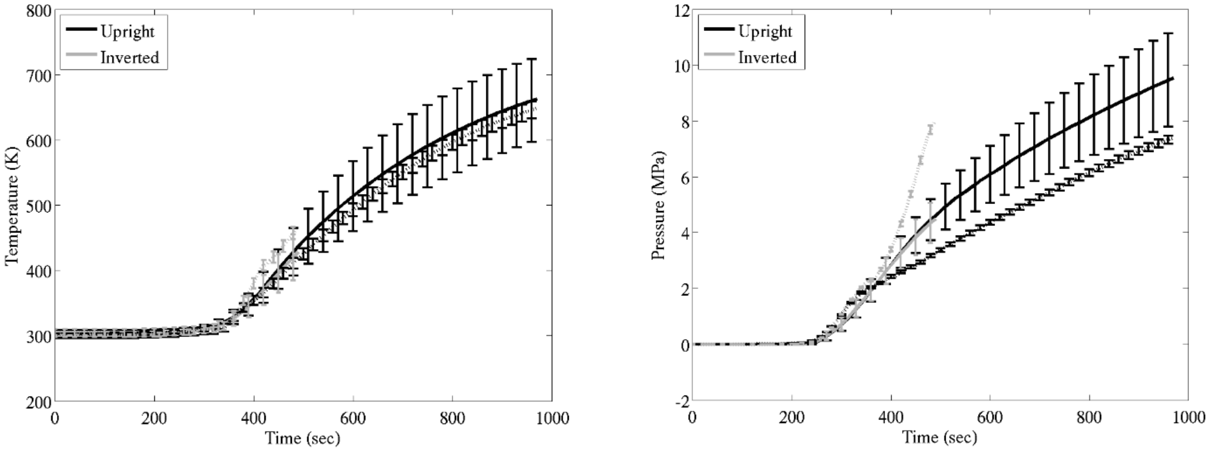

(a) (b)

Figure 84. Inverted and upright computational results (solid) with ±$2\sigma_R$ uncertainty and experimental results (dashed) with ±2% error for (a) temperature vs time for TC 25 and (b) pressure vs time using the LHS approach.

Figure 85 and Figure 86 show the correlation coefficients squared over time. The examination of the correlation coefficients is similar to that of the importance factors in the mean value method. Like in the mean value method, the correlation coefficient for the activation energy of the foam dominates the response of the pressure (Figure 85) for both upright and inverted orientations. Early in time, the hotplate temperature and environmental temperature are driving the response, but during this time, the pressure response is not changing because the foam has not yet started to decompose. Later in time, the foam conductivity and foam specific heat become increasingly important, followed by the activation energy of the foam and the stainless steel conductivity.

This was true in both the upright and inverted cases. When measuring the response of temperature on the outside of the can (Figure 86a) the conductivity of steel is dominant; while for the embedded object (Figure 86b) it is the effective conductivity of the foam for both the inverted and upright cases, although only inverted are shown. For both thermocouples, early in time, the temperature of the environment is dominate because the flow of heat from the heated surface has not yet reached the location of interest.

An additional metric of interest is the Spearman rank correlation coefficients which involve a rank transformation followed by the linear regression as applied for the Pearson correlation coefficients, details of the rank transformation are discussed in Helton and Davis [18]. For this study only the Pearson correlation coefficients are presented because there was very little difference between the two methods of computing correlation coefficients, suggesting a linear relationship between the parameters and responses.

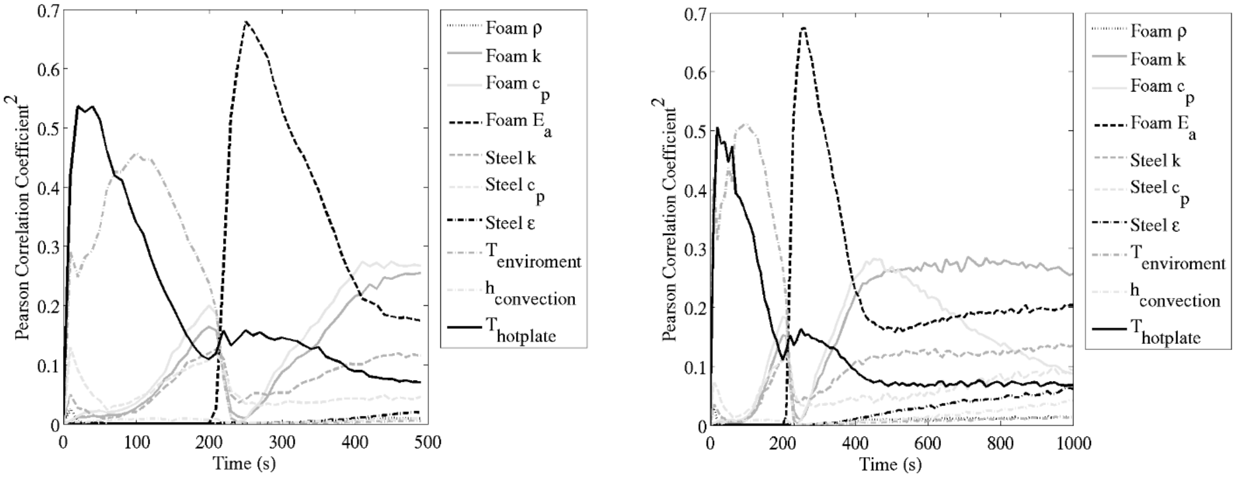

(a) (b)

Figure 85. Squared correlation coefficient vs time response for pressure for (a) inverted and (b) upright.

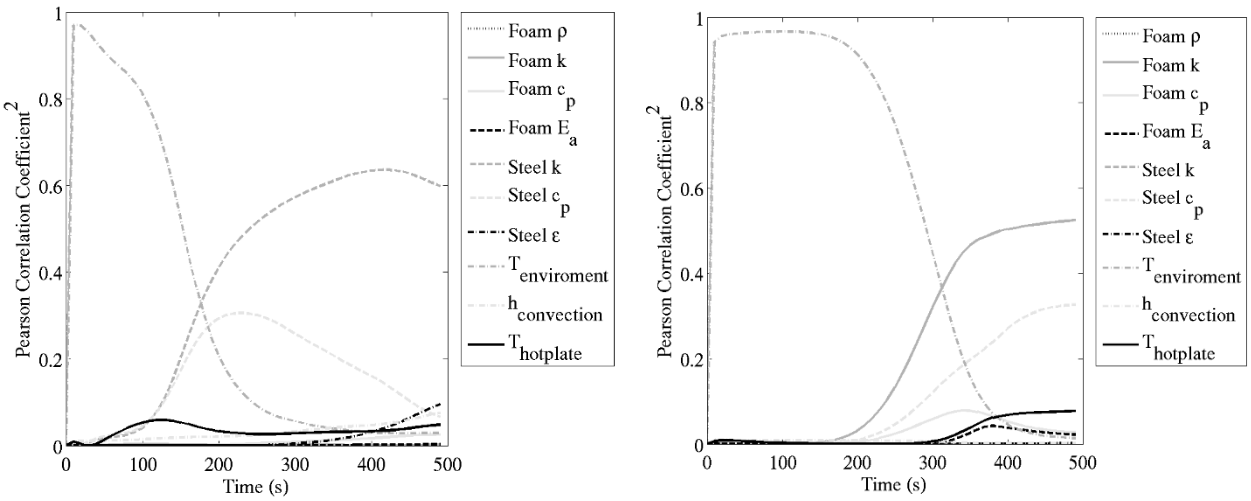

(a) (b)

Figure 86. Inverted can squared correlation coefficient vs time response for (a) TC 17 and (b) TC 25.

In order to investigate the validity of the linear assumption, scatter plots were examined. A scatter plot shows the response (i.e. pressure/temperature) for each LHS run as a function of the parameter variation. Figure 87 through Figure 90 show scatter plots for the parameters that have the highest values of the correlation coefficients for the following responses: pressure, TC17, and TC25. As was shown in Figure 85a, the activation energy is a large contributor to the uncertainty in the pressure response from 200 to 400 seconds and after 400 seconds, the foam effective conductivity and foam specific heat were the main contributors to uncertainty. As a result, Figure 87 presents scatter plots of the pressure response vs. the activation energy multiplier (i.e. how the activation energy was varied) at 250 seconds and 500 seconds. At 250 seconds (Figure 87a), there is a strong downward linear trend (and potentially a subtle nonlinear relationship towards the edges of the parameter space) between the pressure and activation energy. This is not surprising considering that activation energy directly affects the numbers of moles of gas generated (a decrease in activation energy begins the decomposition at lower temperatures (i.e. earlier in time) leading to a higher pressure) which is directly proportional to the pressure response. By 500 seconds (Figure 87b), there is only a slight downward trend between pressure and activation energy. At 500 seconds, the main contributors to the pressure uncertainty are the foam effective conductivity and foam specific heat. Figure 88 shows scatter plots of pressure vs. foam effective conductivity (a) and foam specific heat (b). Slight linear downward and upward trends for both of these parameters are noticeable.

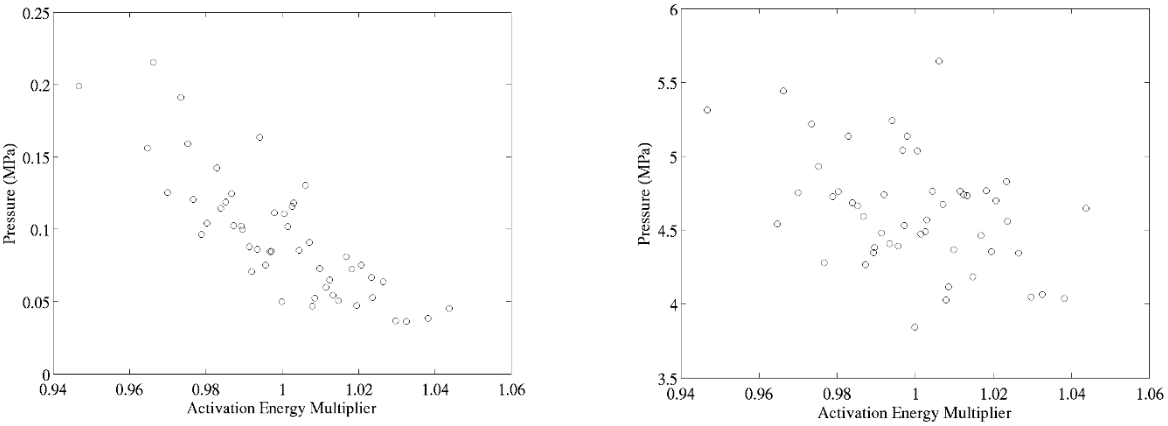

(a) (b)

Figure 87. Scatter plots of pressure vs. activation energy multiplier at (a) 250 and (b) 500 seconds for the inverted configuration.

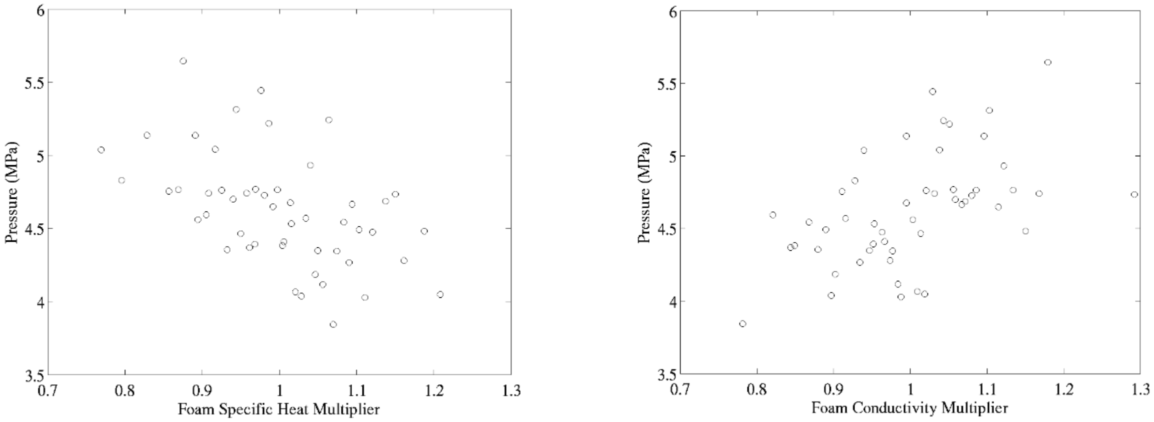

(a) (b)

Figure 88. Scatter plots pressure at 500 seconds for (a) foam specific heat and (b) foam conductivity for the inverted configuration.

Figure 89 illustrates the temperature response of TC17 as a function of stainless steel conductivity and stainless steel specific heat at 500 seconds. There is a strong linear dependence on the stainless steel conductivity and a weaker linear dependence on the stainless steel specific heat. It is interesting to note that even in late time; the contribution to uncertainty is still due to stainless steel properties. Figure 90 displays the temperature response of TC25 as a function of foam effective conductivity and stainless steel specific heat at 500 seconds. There is a strong linear dependence on the foam effective conductivity and a weaker linear dependence on the stainless steel specific heat.

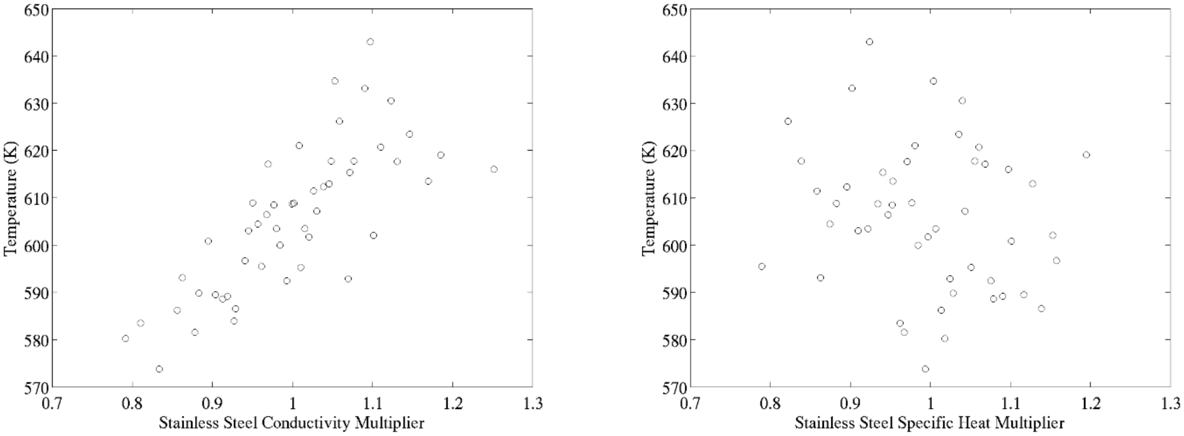

(a) (b)

Figure 89. Scatter Plots for TC17 at 500 seconds for (a) stainless steel conductivity and (b) stainless steel specific heat for the inverted configuration.

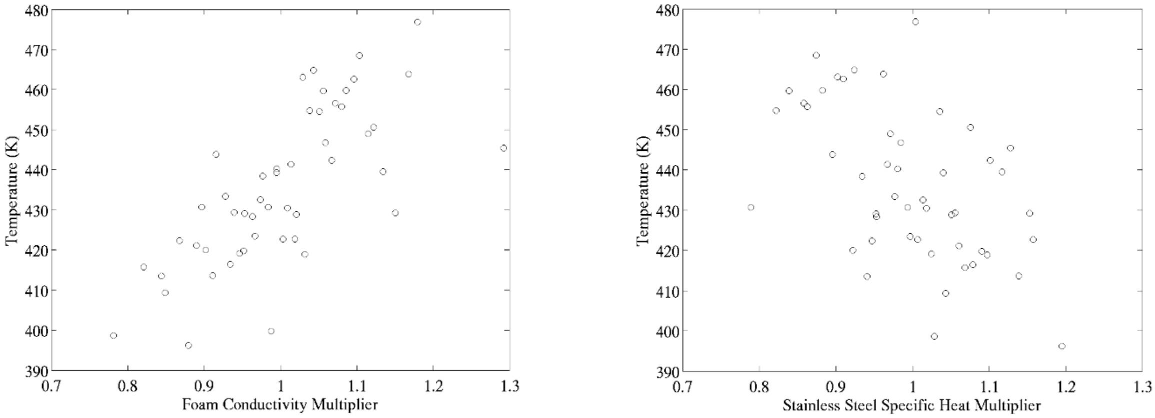

(a) (b)

Figure 90. Scatter Plots for TC25 (a) foam conductivity and (b) stainless steel specific heat for the inverted configuration.

5.3 Comparison of Mean Value and LHS

Figure 91 and Figure 92 show comparisons between mean value and Latin hypercube approaches. In Figure 91, the pressure responses and uncertainties are plotted for both inverted (Figure 91a) and upright (Figure 91b) configurations. There is very little difference between the MV and LHS responses and magnitudes of the uncertainties. Figure 92shows the MV and LHS responses with uncertainties for TC17 and TC25 inverted simulations and experiment. There is minimal difference between MV and LHS responses and magnitude of uncertainty. This indicates that the linear assumption inherit in MV is valid and thus either method is appropriate for this experimental configuration.

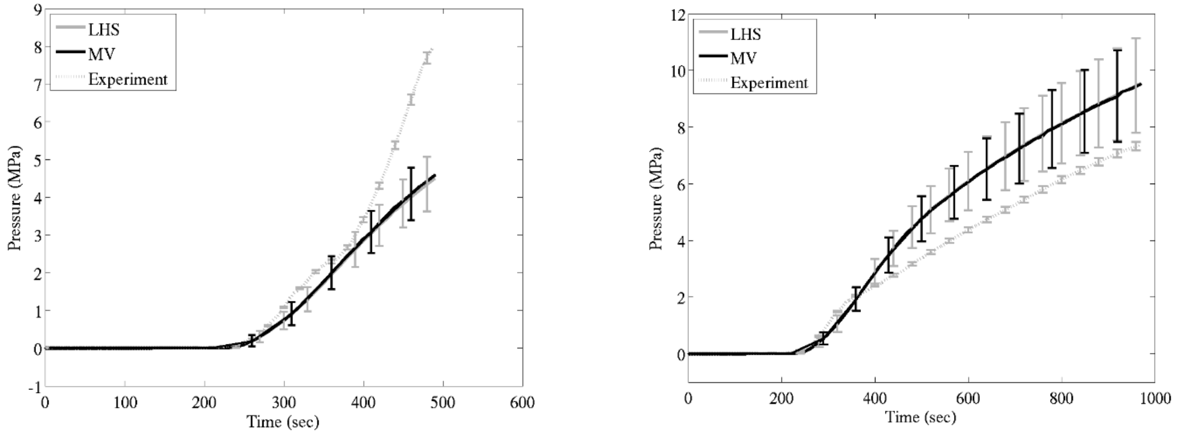

(a) (b)

Figure 91. Latin Hypercube and Mean Value Method assessments of pressure with ±$^{2\sigma_R}$ uncertainty for (a) Inverted and (b) Upright experiments.

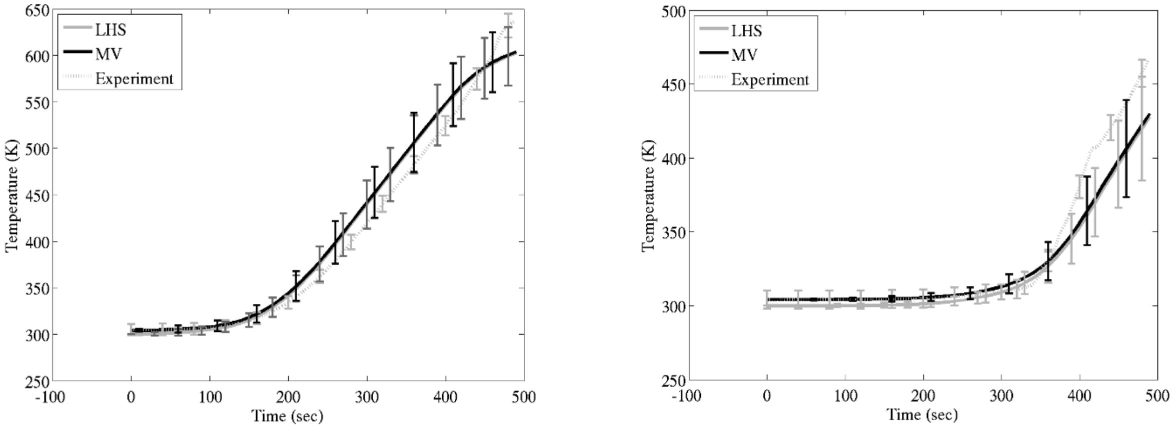

(a) (b)

Figure 92. Inverted Latin Hypercube and Mean Value Method assessments with ±$^{2\sigma_R}$ uncertainty for (a) TC17 and (b) TC25.

6 CONCLUSION

Pressure and temperature responses from a computational model and experiments were examined for the Foam in a Can apparatus. Uncertainties in input parameters for the model were propagated through the simulation using the mean value method and the Latin hypercube approach. Substantial information can be gained through both MV and LHS approaches. In the current application of these approaches, a linear relationship between parameter and response was valid, thus both approaches yielded similar means, standard deviations, and parameter importance/correlation. However, with increasing physics fidelity and increasingly nonlinear responses such as in fluid dynamics, LHS may provide additional insight. Furthermore, there are additional methods that can be used to analyze data with may yield better results when examining nonlinear trends [20, 21, 22]. There is a large amount of understanding of the problem behavior that can be gained through examination of scatter plots as a function of time, parameter, location, and response. However, this approach also yields an infinite number of combinations to examine. It is tempting to examine the response of integrated quantities or only look at a specific time of interest, which is valuable, but can be misleading if responses have varying contributors to uncertainty depending upon time.

While the computational and experimental results agreed well for most cases, in the inverted case, the rate of pressurization in the experiments increases drastically near the end of the test, a response not seen in model. Since the model does not explicitly consider the gravity-induced movement of gaseous or liquid products of decomposition, it does not differentiate between the inverted and upright orientations. In order to properly predict these trends, additional physics needs to be included in the model. For example, a model that includes fluid motion and convective heat transfer involving both gas-vapor and liquid phases is the only mechanism by which temperature distributions and, therefore, the number of moles of decomposition products would change with orientation (due to channeling by hot gases and liquefaction and flow of a condensed phase, either toward or away from a heat flux) would be appropriate to include. The future direction of our work begins to incorporate these effects through including porous media transport, front tracking, and a higher fidelity radiative transport.

7. REFERENCES

1. Beyler, C. and Hirschler, M., Thermal Decomposition of Polymers, *SFPE Handbook of Fire Protection Engineering*, 110-131. National Fire Protection Association (2001)

2. Erickson, K.L., Dodd, A.B., Hogan, R.E., and Dowding, K.J., Heat Transfer, Foam Decomposition, and Container Pressurization: Comparison of Experimental and Modeling Results, Interflam, Nottingham, UK: Interscience Communications Ltd (2010)

3. Erickson, K.L., Dodd, A.B., and Quintana, E.C., Physical Behavior and Container Pressurization During Thermal Decomposition of Polyurethane Foams, Proceedings of BCC 2011, Stamford, CT (2011)

4. Erickson, K.L., Dodd, A.B., Hogan, R.E., Modeling Pressurization Caused by Thermal Decomposition of Highly Charring Foam in Sealed Containers, Proceedings of BCC 2010, Stamford, CT (2010)

5. Sierra Core Team, Sierra Thermal/Fluids Code, Sandia National Laboratories: Albuquerque, NM (2014)

6. Larsen, M.E and Dodd, A.B., Uncertanty Quantification for Foam in Can Experiement, Sandia Internal Memorandum, Sandia National Laboritories Alburquerque NM (2013)

7. Erickson, K. L, Celina, M. C., Hogan, R. E., Nicolette, V. F., and J. H. Aubert, in Fire and Materials 2009, Interscience Commun. Ltd.: London, UK p353-p365.

8. Erickson, K. L., *J. Therm. Anal. Calor.* 2007, 89, pp 427-440.

9. Erickson, K. L. and Oelfke, J., in ACS Symposium Series 1013: Fire and Polymers V, pp. 387-407, C. A. Wilkie, A.B. Morgan, and G. L. Nelson, eds., ACS 2009.

10. Taylor, R. E., Groot, H., and Ferrier, J., Thermophysical Properties of Two Foams, TPRL 1964, Thermophysical Properties Res. Lab., West Lafayette, IN, 1998.

11. Neet, T. E., "Development of Non-TDI Polyurethane Encapsulation Foams", PDO 705898 Final Report, Sept. 1994.

12. Jin, G., Venkatesan, G., Chyu, M. C., and Zheng, J. X., *Measurement of Thermal Conductivity and Heat Capacity of Foam Insulation During Transient Heating*, AV7569 Final Report, Dept. of Mechanical Engineering, Texas Tech Univ., (1998)

13. Siegel, R. and Howell, J. R., Thermal Radiation Heat Transfer, 2nd ed., Hemisphere Publishing, Cambridge, 1982, 497-501.

14. Reichman, J., *Applied Optics*, 12 (8), August 1973, 1811-1815

15. Scott, S.N., Templeton, J.A., Ruthruff, J.R., Hough, P.D. and Peterson, J.P., Computational Solution Verification Applied to a Thermal Model of a Ruggedized Instrumentation Package, Computational Methods and Experimental Measurements XVI, A Coruña, Spain 2-4 July (2013)

16. Hughes, T.J.R., *The Finite Element Method*. Mineola, New York: Dover Publications (2000)

17. Saltelli, A., Chan, K., and Scott, E. M., *Sensitivity Analysis*, Chapter 6, John Wiley and Sons, Inc., New York (2000)

18. Helton, J. C., and Davis, F. J., Latin Hypercube Sampling and the Propagation of Uncertainty in Analyses of Complex Systems, SAND2001-0417, Sandia National Laboratories, Albuquerque, NM 87185.

19. Adams, B. M., Ebeida, M. S., Eldred, M. S., Jakeman, J. D., Swiler, L. P., Bohnhoff, W. J., Dalbey, K. R., Eddy, J. P., Hu, K. T., Vigil, D. M., Bauman, L. E., and Hough, P. D., "DAKOTA, A Multilevel Parallel Object-Oriented Framework for Design Optimization, Parameter Estimation, Uncertainty Quantification, and Sensitivity Analysis, Version 5.4 Users Manual," SAND2010-2183, Sandia National Laboratories, Albuquerque, NM, December 2009.

20. Helton, J.C., Johnson, J.D., Sallaberry, C.J., Storlie, C.B., Survey of sampling-based methods for uncertainty and sensitivity analysis, Reliability Engineering and System Safety, vol. 91, 1175-1209, 2006.

21. Ghanem, R. G. and Spanos, P.D., Stochastic Finite Elemets: A Spectral Approach, Verlag, New York, 1991.

22. Sacks, J., Schiller, S.B., Welch, W., Design for computer experiments. Technometrics, vol 31 41–47, 1989.

DISTRIBUTION

4 Lawrence Livermore National Laboratory
Attn: N. Dunipace (1)
P.O. Box 808, MS L-795
Livermore, CA 94551-0808

1 MS0899 Technical Library 9536 (electronic copy)

Sandia National Laboratories